MEASUREMENTS OF PERNITRIC ACID AND INORGANIC BROMINE SPECIES USING CHEMICAL IONIZATION MASS SPECTROMETRY

A Dissertation
Presented to
The Academic Faculty

by

Chen, Dexian

In Partial Fulfillment
of the Requirements for the Degree
Doctor of Philosophy in the
School of Earth & Atmospheric Sciences

Georgia Institute of Technology
December 2016

MEASUREMENTS OF PERNITRIC ACID AND INORGANIC BROMINE SPECIES USING CHEMICAL IONIZATION MASS SPECTROMETRY

Approved by:

Dr. L. Gregory Huey, Advisor
School of Earth & Atmospheric Sciences
Georgia Institute of Technology

Dr. Paul H. Wine
School of Chemistry & Biochemistry
Georgia Institute of Technology

Dr. Yuhang Wang
School of Earth & Atmospheric Sciences
Georgia Institute of Technology

Dr. Yi Deng
School of Earth & Atmospheric Sciences
Georgia Institute of Technology

Dr. Nga Lee Ng
School of Chemical & Biochemical Engineering
Georgia Institute of Technology

Date approved: 20 September 2016

To my parents

ACKNOWLEDGEMENTS

I would like to express my gratitude to my advisor, Prof Greg Huey, for his support, and guidance. His knowledge of chemistry and instrumentation has been valuable resources for me. He taught me how to think and analyze critically. He was always available for discussion even though he was busy. Thank him for his encouragement over the last six years, especially in the last year when I was very frustrated.

I would like to thank current or previous CIMS group members: Dave Tanner, Bob Stickel, Jin Liao, Jeff Shook, Arsineh Hecobian, Steve Sjostedt, Eric Parker, Xiaoxi Liu and Zainab Al-Riyami. Dave taught me instrument operations and electrics. Dave and Bob were in the field with me and taught me a lot, i.e., instrument maintenance and how to find a good restaurant. Jin helped me a lot in my first and second years.

I would like to thank Prof Sally Ng and her group members: Dr Theo Nah, Lu Xu and Javier Sanchez for their assistances. I would also like to thank Dr Mike Nicovich for his help in my lab experiments.

Dr Laura Pan and Dr Ross Salawitch taught me good lessons in the CONTRAST campaign and later during my preparation of the paper manuscript. Many thanks to Dr Gao Chen, Dr Andy Neuman, Dr Andy Weinheimer, Dr Jack Dibb, Dr Dan Riemer, Dr Becky Hornbrook, Hong Viet Ta, and other CONTRAST, DC3, and GEOSummit team members. Many thanks to Dr John Nowak and Dr John Orlando for their helps.

Many thanks to my committee members: Dr Yuhang Wang, Dr Sally Ng, Dr Paul Wine and Dr Yi Deng.

Finally, I would like to thank my parents for their support and love over the last six years.

TABLE OF CONTENTS

LIST OF TABLES

LIST OF FIGURES

LIST OF SYMBOLS AND ABBREVIATIONS

CDC	Collisional dissociation chamber
CIMS	Chemical ionization mass spectrometry
CONTRAST	The CONvective TRansport of Active Species in the Tropics campaign
LMS	Lowermost stratosphere
LOD	Limit of detection
MBL	Marine boundary layer
PGI	Product gas injection
RF	Research flight
SGI	Source gas injection
SZA	Solar zenith angle
TFT	Tropical free troposphere
TTL	Tropical tropopause layer
VOC	Volatile organic compounds
VSL	Very short-lived

SUMMARY

Measurements of atmospheric trace gases is a central aspect of the study of atmospheric chemistry. It allows scientists to critically challenge our current understanding of the atmosphere. For years, chemical ionization mass spectrometry (CIMS) has been utilized to measure atmospheric trace gases.

This thesis presents two projects that involves measurements with CIMS. In the first project measurement of pernitric acid (HO_2NO_2) was performed in metropolitan Atlanta in two seasons (winter 2014, and summer 2015). As HO_2NO_2 is in equilibrium with hydroperoxyl radical (HO_2) and nitrogen dioxide (NO_2) at warm temperatures, this measurement provided a way to infer HO_2. The project illustrates the feasibility of inferring HO_2 via HO_2NO_2 measurement at warm regions when HO_2 measurements are unavailable.

The second project is airborne CIMS observations of inorganic bromine species, BrO and HOBr +Br_2 over the tropical West Pacific during the CONvectic Transport of Active Species in the Tropics (CONTRAST) campaign in 2014. Bromine is a key ozone-depleting substance (ODS). The transport of inorganic bromine (Br_y) to the stratosphere, known as product gas injection (PGI) of bromine species, contributes to a significant part of stratospheric bromine loading. PGI occurs in the tropics. The tropical West Pacific plays a particularly important role in PGI. The goal of this project is to provide constraints for further understanding of the whole PGI mechanism. Most of the time CIMS did not detect significant amount of BrO or HOBr +Br_2 in the tropical free troposphere (TFT) and the tropical tropaupose layer (TTL), given the CIMS 1-min average limit of detection (LOD) was 0.6 to 1.6 pptv for BrO, and 1.3 to 3.5 pptv for HOBr + Br_2. During one flight, BrO

observations from the TTL to the extratropical lowermost stratosphere (LMS) were used to infer a profile of Br_y. Based on this profile, the PGI of bromine species was estimated be roughly 2 pptv. Analysis of Br_y partitioning further indicates that BrO levels are likely very low in the TFT environment and that future studies should target the measurement of HBr or Br atoms.

CHAPTER 1. INTRODUCTION

Atmospheric trace gases comprise less than 1% of the earth atmosphere, but are its most active components and largely control its chemical properties. They are involved in many important processes, such as degradation of pollutants, production and destruction of stratospheric and tropospheric ozone, formation and growth of particular matter, and global warming [e.g., *Seinfeld and Pandis*, 2016; *Finlayson-Pitts and Pitts*, 2000]. Due to their low concentrations, the detection of atmospheric trace gases requires highly sensitive instruments. The chemical ionization mass spectrometry (CIMS) technique has provided sensitive detections of trace gases [*Huey*, 2007]. To date, CIMS techniques have been utilized to detect a host of trace gases, e.g., $CH_3C(O)O_2NO_2$ (PAN), HONO, NH_3, HCl, SO_2, Cl_2, Br_2, ClO, BrO, HOCl, HOBr, N_2O_5, HNO_3, HONO, $ClNO_2$, HCOOH, HNCO, $CH_3C(O)OOH$ [e.g., *Huey et al.*, 1998; *Kercher, et al.*, 2009; *Kim et al.*, 2007; *Le Breton et al.*, 2012, 2014; *Liao et al.*, 2011a, 2011b, 2012, 2014; *Marcy et al.*, 2005; *McNeill et al.*, 2006; *Neuman et al.*, 2010; *Phillips et al.*, 2013; *Pratt et al*, 2013, *Slusher et al.*, 2002, 2004; *Thornton et al*., 2003; *Woodward-Massey* et al., 2014; *Zheng et al.*, 2011].

This thesis focuses on several atmospheric trace gases: peroxynitric acid (HO_2NO_2), and inorganic bromine species (Br_y = BrO + Br + 2×Br_2 + HOBr + $BrNO_3$ + HBr + BrCl). Peroxynitric acid (HO_2NO_2) is formed via the association of HO_2 and NO_2, which couples both HO_x (= HO_2 + OH) and NO_x (= NO + NO_2) families [*Levine et al.*, 1977; *Niki et al.*, 1977]. HO_x and NO_x are central to atmospheric chemistry [*Levy*, 1971, 1972; *Chameides and Walker*, 1973; *Crutzen*, 1974]. At low temperature, HO_2NO_2 is an important reservoir species of HO_x and NO_x and thus modifies local photochemistry. At high temperature, due

to its rapid thermal dissociation [e.g., *Gierczak et al.*, 2005], HO_2NO_2 comes to equilibrium with HO_2 and NO_2, which provides a way to inference of HO_2 via HO_2NO_2 [*Spencer et al.*, 2009]. Br_y is important ozone depletion substance (ODS) [*Solomon*, 1999]. The study of Br_y is an important aspect of the assessment of ozone depletion. Both HO_2NO_2 and Br_y and related to key concerns of atmospheric chemistry.

Chapter 2 discusses the basic principles of CIMS technique, as well as the photochemical box models used for data analysis in this work.

Chapter 3 [*Chen et al.*, 2016a, in preparation] presents measurements of HO_2NO_2 in metropolitan Atlanta, US in winter 2014 and summer 2015, using CIMS with the reagent ion $I^-\cdot(H_2O)_n$, and inferred HO_2 concentrations based on this equilibrium. The measurement technique for HO_2NO_2 is detailed. This method is further explored by analysing the suppression of HO_2 at high NO, the correlation of HO_2 with O_3 and NO_3 at night, and comparing inferred HO_2 with model calculations.

Chapter 4 [*Chen et al.*, 2016b, submitted] presents CIMS measurements of BrO and HOBr+Br_2 over the tropical West Pacific Ocean within the altitude range of 1 to 15 km, during the CONvective TRansport of Active Species in the Tropics (CONTRAST) campaign in 2014, analyzes the partitioning of Br_y in the TFT and TTL, and estimates the product gas injection (PGI) from Br_y to the stratosphere.

CHAPTER 2. METHODOLOGY

2.1 Chemical ionization mass spectrometry (CIMS)

The basic principle of CIMS is to selectively ionize targeted analytes in the complex matrix of ambient air. For instance, HNO_3 can be ionized with the reagent ion SF_5^- [*Marcy et al.*, 2005].

(R2.1) $HNO_3+SF_5^- \rightarrow HF\cdot NO_3^-$ (*m/z* 82) + SF_4

In R 2.1, the ionization product $HF\cdot NO_3^-$ gives a unique signature HNO_3, and its signal can be tracked to retrieve ambient HNO_3 concentrations.

The CIMS are designed to efficiently detect species in air using ion molecule reactions (Figure 2.1). The CIMS is comprised of the following differentially pumped regions: a flow tube, a collisional dissociation chamber (CDC), an octopole ion guide, a quadrupole mass filter and an ion detector. Air is sampled via an orifice into the flow tube, where the ion molecule reactions took place. The reagent ion is generated by passing a N_2 flow that contains trace amount of its precursor into the flow tube via a ^{210}Po ion source. The ionized products are sampled into the CDC, where the collision between ions and neutral molecules is enhanced by an electric field. Weakly-bound cluster ions (mainly water cluster ions) are dissociated into core ions (e.g., $Br_2\cdot I^-\cdot(H_2O)_n$ was dissociated into $Br_2\cdot I^-$)[*Tanner et al.*, 1997]. Then ionization products are guided by the octopole to the quadrupole for detection.

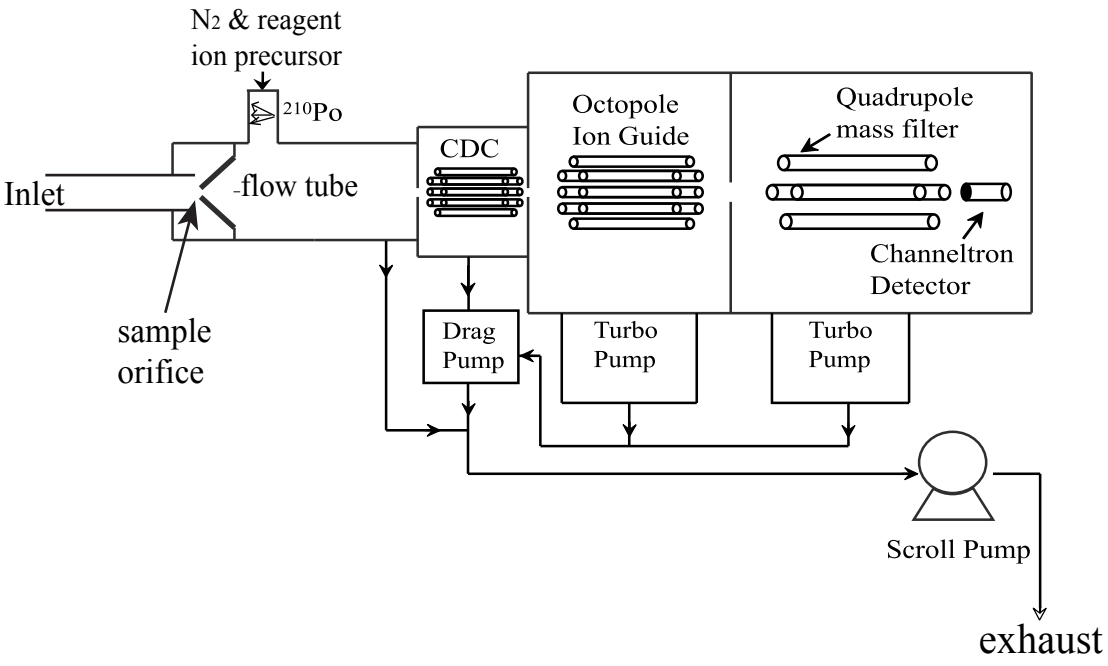

Figure 2.1. Schematic of the basic CIMS configuration.

CIMS is often calibrated by the standard addition method [e.g., *Neuman et al.*, 2006]. For example, HNO_3 measurements by CIMS are calibrated by periodically adding a known amount of HNO_3 to the instrument inlet to track its sensitivity. If a portable calibration source of the analyte is not available, an indirect calibration method is often applied. This involves using a stable calibrant in the field to monitor the CIMS sensitivity. After the field measurements, the relative sensitivity of the analyte to the calibrant is assessed in laboratory. For instance, for Br_2 measurement using the reagent SF_6^-, the calibrant SO_2 is used in the field to track instrumental sensitivity, and the sensitivity ratio Br_2/SO_2 is determined in laboratory [*Liao et al*, 2011]:

(R2. 2) $Br_2 + SF_6^- \rightarrow Br_2^-$ (*m/z* 158, 160, 162) + SF_6 (Measurement)

(R2. 3) $SO_2 + SF_6^- \rightarrow SO_2F_2^-$ (*m/z* 102) + SF_4 (calibration)

2.2 Zero-dimensional box models

Two zero-dimensional (0-D) photochemical box models, a steady-state model, and a time-dependent model, were applied in this thesis. They were developed based on previous studies [*Sjostedt et al.*, 2007; *Kim et al.*, *2007*; *Liao et al.*, 2011a]. The chemistry scheme of both models is detailed in Appendix A.

The steady-state model is to evaluate relatively short-lived species including HO_x and some inorganic bromine species (Br atom, Br_2, BrO, HOBr, $BrNO_3$, BrCl). Parameters such as *T*, *p*, and photo-dissociation rates (*j* values) and long-lived chemicals (lifetime longer than hours) are constrained. In the time-dependent model, *T*, *p* and *j* values are constrained. Long-lived species are calculated in a time-dependent manner, given initial concentrations. Short-lived species are calculated to steady state. Detailed setups were different in different studies and are listed in different chapters.

CHAPTER 3. INFERRING HYDROPEROXYL RADICAL (HO_2) IN METROPOLITAN ATLANTA VIA MEASUREMENT OF PERNITRIC ACID (HO_2NO_2) USING CHEMICAL IONIZATION MASS SPECTROMETRY

3.1 Introduction

The Hydroperoxyl radical (HO_2) is a key species in the atmosphere and is the dominant form of HO_x (OH + HO_2). Sources of HO_2 include the oxidation of CO and volatile organic compounds (VOC) by hydroxyl radicals (OH), the photolysis of carbonyl compounds, the ozonolysis of alkenes, and the oxidation of VOC by the nitrate radical (NO_3) [e.g., *Atkinson and Carter*, 1984; *Johnson and Marston*, 2007; *Paulson and Orlando*, 1996; *Wayne et al.*, 1991; *Geyer et al.*, 2003; *Kanaya et al.*, 2007]. The last two are important sources of HO_2 at night. HO_2 is highly involved in important atmospheric processes such as the degradations of pollutants, ozone production and secondary organic aerosols (SOA) formation [e.g., *Finlayson-Pitts and Pitts*, 2000; *Carton et al.*, 2009; *Jenkin* 2004]. Observations of HO_2 are important for understanding and constraining atmospheric chemistry.

Pernitric acid (HO_2NO_2) is closely related to HO_2. HO_2NO_2 has a relatively simple chemistry in the atmosphere (R1− R4) [e.g., *Levine et al.*, 1977; *Niki et al.*, 1977; *Jiménez et al.*, 2004; *Gierczak et al.*, 2005].

(R3.1, 3. −1) $HO_2+NO_2+M \leftrightarrow HO_2NO_2+M$

(R3.2a) $HO_2NO_2+h\upsilon \rightarrow HO_2+NO_2$

(R3.2b) → $OH+NO_3$

(R3.3) $HO_2NO_2+OH \rightarrow NO_2+O_2+H_2O$

(R3.4) HO_2NO_2 → deposition/scavenging

The thermal decomposition rate k_{-1} is a strong function of temperature, e.g., ~5×10^{-6} s^{-1} at –30°C, and ~ 1×10^{-1} s^{-1} at 30°C [*Burkholder et al.*, 2015]. The important role of HO_2NO_2 in HO_x and NO_x (= NO + NO_2) chemistry in cold regions has been widely discussed [*Talbot et al.*, 1999; *Jaeglé et al.*, 2001; *Slusher et al.*, 2002; *Chen et al.*, 2001, 2004; *Sjostedt et al.*, 2006; *Kim et al.*, 2007; *Stiller et al.*, 2007; *Jones et al.*, 2014]. In warm regions, as the thermal decomposition is fast and dominates the loss, HO_2NO_2 chemistry is reduced to a steady state with HO_2 and NO_2 (R 3.1, 3.−1). Given proper averaging time that allows steady state to be approached, HO_2 can be inferred via HO_2NO_2 [*Spencer et al.*, 2009].

$$[HO_2] = \frac{k_{-1}[HO_2NO_2]}{k_1[NO_2]} = \frac{[HO_2NO_2]}{K[NO_2]} \qquad (2.1)$$

where $K = k_1/k_{-1}$ is the equilibrium constant. K is a function of temperature alone [*Burkholder et al.*, 2015].

In this chapter, the CIMS technique was employed to measure HO_2NO_2 in metropolitan Atlanta, and infer HO_2 from observations of HO_2NO_2 and NO_2. Hydrated iodide ($I^-\cdot(H_2O)_n$) is used as the reagent ion(s) for the CIMS detection of HO_2NO_2 [*Zhang et al.*, 1997; *Abida et al.*, 2011; *Veres et al.*, 2015; *Chen et al.*, 2016, in preparation]. $I^-\cdot(H_2O)_n$ is also a suitable reagent for detections of other species, e.g., Cl_2, Br_2, ClO, BrO, HOCl, HOBr, N_2O_5, HNO_3, HONO, $ClNO_2$, HCOOH, HNCO, and $CH_3C(O)OOH$ [e.g.,

Neuman et al., 2010; *Liao et al.*, 2011a, 2012, 2014; *Pratt et al.*, 2013, *Kercher* et al., 2009; *McNeill et al.*, 2006; *Le Breton et al.*, 2012, 2014; *Thornton et al.*, 2003; *Woodward-Massey et al.*, 2014; *Phillips et al.*, 2013]. This makes it possible to measure HO_2NO_2, which can be used to infer HO_2, along with a host of other species. The goal of this work is to evaluate if the $I^-\cdot(H_2O)_n$ CIMS method can be used to infer HO_2 levels in a warm polluted environment.

3.2 Methods

3.2.1 Observations

Observations were made in winter (20 Nov 2014 to 2 Jan 2015) and summer (10 June to 7 July 2015), respectively, on top of the Georgia Tech Ford ES&T building in metropolitan Atlanta (33°46' N, 84°24' W), 10 m above the ground, and 0.6 km to the west of the Interstate-75 highway. Concurrent measurements of HO_2NO_2, NO, NO_2, CO, O_3, N_2O_5 (winter only) and meteorological parameters were performed (Table 3.1). Data were reported in local time, UTC−5 h in winter, and UTC−4 h in summer.

Table 3.1. Summary of the measurements in Atlanta in two seasons.

	species	Instrument	LOD	Integration Time	uncertainty	reference
Winter (2014)	HO_2NO_2	CIMS	0.2 pptv	1 min	±22%	*Chen et al.*, 2016, and *Veres et al.*, 2015
	N_2O_5	CIMS	0.2 pptv	1 min	±25%	*Kercher et al.*, 2009
	NO	CL[a]	4.5 pptv	1 min	±10%	*Ryerson et al.*, 2000
	NO_2	CAPS	< 60 pptv	5 s	< 5%	*Kebabian et al.*, 2008
	O_3	Thermo 49C	< 1 ppbv	10 s	±1 ppbv	-
	CO	Thermo 48C	<1 ppbv	10 s		-
	met. [b]	Vantage Pro2	-	1 min		-
Summer (2015)	HO_2NO_2	CIMS	0.6 pptv	1 min	±16%	*Chen et al.*, 2016, and *Veres et al.*, 2015
	NO	Teledyne 200EU	50 pptv	1 min	±5%	-
	NO_2	CAPS	<60 pptv	5 s	< 5%	*Kebabian et al.*, 2008
	O_3	Teledyne T400	400 pptv	10 s	±5%	-
	CO	IR	< 1 ppbv	10 s		-
	met. [b]	Vantage Pro2	-	1 min		-

a. Chemiluminescence

b. Meteorological parameters include *T*, *p*, humidity, wind speed, wind gust, wind direction, total solar radiation, solar UV radiation, cloud base, and precipitation rate.

3.2.2 CIMS measurement of HO_2NO_2

3.2.2.1 CIMS Apparatus

Due to instrument availability, different CIMS instruments were employed during each season. Both CIMS instruments had similar configurations to that described by *Liao et al.* [2011a]. The main differences were the inlet configuration and flow. The inlets were Teflon^{TM} FEP tubings (O.D. = 1.22 cm, and I. D. = 0.95 cm), 9 m and 5 m long respectively in winter and summer observations. The excess flows were 45 slpm (standard liter per minute, standard = 0°C and 1013 hPa) and 40 slpm, respectively. Correspondingly, the residence times in the inlets were roughly 0.8 s and 0.5 s, respectively. To assess the loss of HO_2NO_2 in the inlet, HO_2NO_2 sample was flown through (1) the inlet used for sampling, (2) a new, clean inlet of the same diameter and length as the sampling inlet, and (3) a very short (~30 cm), clean inlet of the same diameter. HO_2NO_2 signals were found to be the same for all cases, and thus it is concluded that the wall loss of HO_2NO_2 was minimal.

3.2.2.2 Ion chemistry and possible interferences

HO_2NO_2 is detected by using $I^-\cdot(H_2O)_n$ CIMS in two channels $HO_2NO_2\cdot I^-$ (*m/z* 206) and NO_3^- (*m/z* 62) [*Zhang et al.*, 1997; *Abida et al.*, 2011; *Veres et al.*, 2015]. The $I^-\cdot(H_2O)_n$-HO_2NO_2 chemistry has not been studied. However, previous work showed that I^- clusters such as $Br_2\cdot I^-$ and $BrO\cdot I^-$ are formed via a ligand-exchange reaction of hydrated I^- and the detected species, rather than a direct association [e.g., *Neuman et al*., 2010; *Liao et al.*, 2011a], since the departing H_2O can take away excess energy and stabilize the clusters. Laboratory experiments were performed to understand the $I^-\cdot(H_2O)_n$-HO_2NO_2 chemistry. HO_2NO_2 was synthesized by adding 0.4 g solid NO_2BF_4 (96%, Alfa Aesar) to

2 mL ice-chilled H_2O_2 (90%) in a dry atmosphere [*Kenley et al.*, 1981]. The 90% H_2O_2 was prepared by bubbling 50% H_2O_2 (Sigma-Aldrich) with a dry N_2 flow, and the concentration of H_2O_2 solution was confirmed by measuring its density. After synthesis the solution was immediately transferred to a glassware that was immersed in ice bath. The HO_2NO_2 vapor was flushed out of the glassware and was diluted in a stepwise manner to operating concentrations (Figure 3.1). HNO_3 is a by-product of the synthesis, but does not form NO_3^- in reactions with $I^-\cdot(H_2O)_n$ under our conditions. Fixed concentration of HO_2NO_2 was introduced to CIMS over a wide range of humidity. The $I^-\cdot H_2O$ (*m/z* 145) signal increased as the humidity increased and tended to be saturated at high humidity. Here $I^-\cdot H_2O$ should be regarded as a surrogate for all $I^-\cdot(H_2O)_n$ ions as $I^-\cdot(H_2O)_n$ was partially dissociated in the CDC. At almost zero humidity no $I^-\cdot H_2O$ nor $HO_2NO_2\cdot I^-$ but NO_3^- signal was detected. As the humidity increased, $HO_2NO_2\cdot I^-$ signal increased accordingly and was proportional to $I^-\cdot H_2O$ signal, while the NO_3^- signal did not change (Figure 3.2). This indicates that $HO_2NO_2\cdot I^-$ is also formed via a ligand-exchange reaction of hydrated I^- (R3.5) rather than a direct association. However, NO_3^- can be formed by reactions with I^- and hydrated I^-. Both reactions (R3.6a, R3.6b) are efficient as the NO_3^- yield is high over a wide range of humidity.

(R3.5) $I^-\cdot(H_2O)_n + HO_2NO_2 \rightarrow HO_2NO_2\cdot I^-$(*m/z* 206) $+ nH_2O$

(R3.6a) $I^- + HO_2NO_2 \rightarrow NO_3^-$(*m/z* 62) $+ HOI$

(R3.6b) $I^-\cdot(H_2O)_n + HO_2NO_2 \rightarrow NO_3^-$(*m/z* 62) $+ HOI + nH_2O$

HO_2NO_2 concentrations were retrieved based on the $HO_2NO_2\cdot I^-$ channel. The NO_3^- channel is the major channel with a branching ratio > 90% but is known to be non-specific for HO_2NO_2. It can be form via reactions of $I^-\cdot(H_2O)_n$ and several species (HO_2NO_2, N_2O_5,

NO_3, $BrONO_2$, $ClONO_2$) [*Hanson and Ravishankara*, 1991; *Huey et al.*, 1995; *Thornton et al.*, 2003; *Slusher et al.*, 2004].

The detection on the $HO_2NO_2 \cdot I^-$ channel can be interfered with by $I \cdot {}^{79}Br^-$ of the same *m/z* in a bromine-rich environment [*Liao et al.*, 2011a].

(R3.7) $HOBr + I^- \cdot (H_2O)_n \rightarrow I \cdot Br^-$ (*m/z* 206, 208) +…

This interference can be corrected by tracking the isotope $I \cdot {}^{81}Br^-$ at *m/z* 208. Nitryl chloride ($ClNO_2$) is detected as $ClNO_2 \cdot I^-$ at *m/z* 208 ($^{35}ClNO_2 \cdot I^-$) and 210 ($^{37}ClNO_2 \cdot I^-$) [*Kercher et al.*, 2009]. If $ClNO_2$ is present, the $^{35}ClNO_2 \cdot I^-$ signal at *m/z* 208 needs to be subtracted to obtain the $I \cdot {}^{81}Br^-$ signal. Thus $^{37}ClNO_2 \cdot I^-$ signal at *m/z* 210 needs to be tracked. In winter, signals at *m/z* 208 and 210 were found to only originate from $ClNO_2$, based on their correlation and the known isotope ratios. This ruled out the $I \cdot {}^{79}Br^-$ interference. In summer, no $ClNO_2 \cdot I^-$ nor $I \cdot Br^-$ was found at *m/z* 208 or 210.

High NO_2 (up to ~ 65 ppbv) in Atlanta can be a potential interference for HO_2NO_2 detection. For this reason, NO_2 standards of up to 86 ppbv were added to the inlet during observations, but no significant changes of signal were observed on both $HO_2NO_2 \cdot I^-$ and NO_3^- channels. Thus, typical levels of NO_2 in Atlanta do not interfere with the detection of HO_2NO_2.

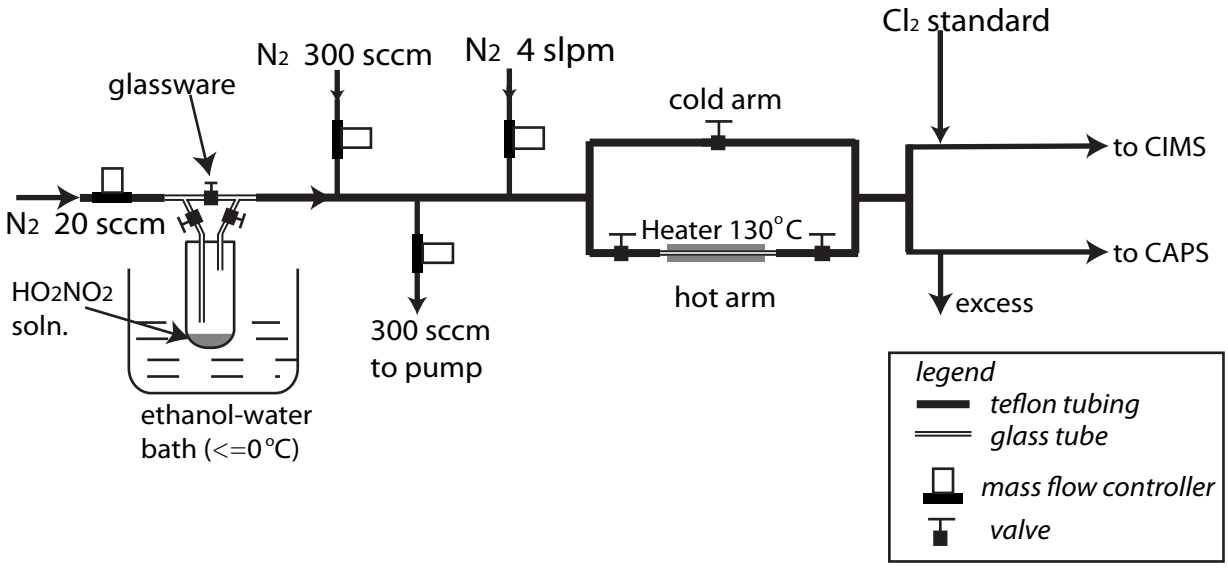

Figure 3.1. The flow setup for laboratory experiments of HO_2NO_2. HO_2NO_2 solution is stored in a glassware that is immerged in an ethanol-water bath ($\leqslant$ 0°C). A flow of 20 standard cubic centimeters per minute (sccm, standard = 0°C and 101.3 kPa) N_2 carries HO_2NO_2 vapor out of the glassware. HO_2NO_2 is diluted in a stepwise manner. The outflow from the glassware is combined with 300 sccm of N_2, and then 300 sccm is exhausted, and the rest is further combined with 4 slpm of N_2. The cold-hot arms are designed for the calibration experiment (Sect. 2.4). To quantify HO_2NO_2, the flow first goes through the cold arm and then the hot arm. The ΔNO_2 recorded by CAPS gives the quantity of HO_2NO_2. The signal recorded by CIMS and the amount of HO_2NO_2 quantified by CIMS give the CIMS sensitivity to HO_2NO_2. The sensitivity to HO_2NO_2 was compared to the sensitivities to Cl_2 to obtain the sensitivity ratio HO_2NO_2/Cl_2.

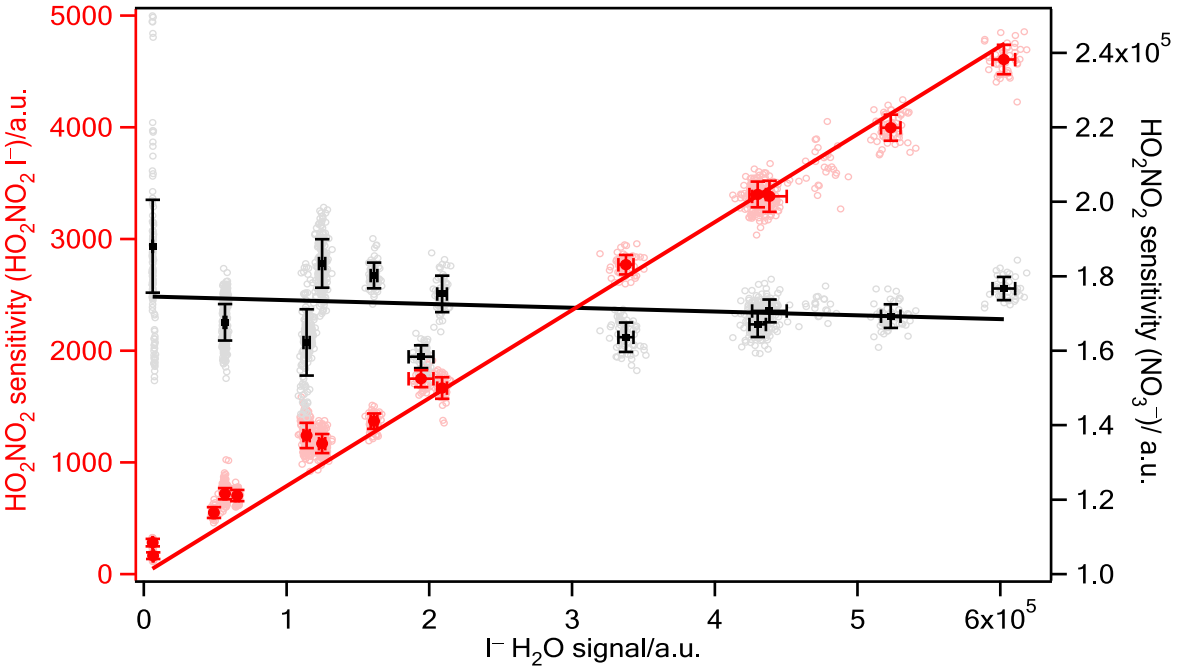

Figure 3.2. The sensitivity towards HO_2NO_2 on both $HO_2NO_2 \cdot I^-$ and NO_3^- channel as a function of $I^- \cdot H_2O$. The sensitivity on the $HO_2NO_2 \cdot I^-$ channel is proportional to $I^- \cdot H_2O$.

3.2.2.3 Calibration

A two-step indirect calibration was applied as a portable HO_2NO_2 calibration source has not been developed. A known amount of Cl_2 from a permeation tube (KIN-TEK) was periodically added into the inlet to track the sensitivity variation (R3.8) [*Liao et al.* 2011a; *Neuman et al.*, 2010].

(R3.8) $Cl_2 + I^- \cdot (H_2O)_n \rightarrow Cl_2 \cdot I^- (m/z\ 197, 199, 201) + nH_2O$

The Cl_2 emission rate was determined every two or three days by a spectrophotometric method [*Wu et al.*, 1963; *Kazantseva et al.*, 2002]. The relative sensitivity of HO_2NO_2 to Cl_2 was determined in the laboratory by comparing signals of known amounts of HO_2NO_2 and Cl_2. HO_2NO_2 was quantified by measuring the resulting NO_2 of HO_2NO_2 thermal decomposition (R3.−1) with a Cavity Attenuated Phase-shift

Spectroscopy (CAPS, Aerodyne). HO_2NO_2 was thermally decomposed by flowing through a glass tube heated to ~130°C. HO_2NO_2 was found to be completely decomposed under our conditions. The experimental setup is displayed in Figure 3.1.

Sensitivities to Cl_2 (as $Cl_2 \cdot I^-$) and HO_2NO_2 (as $HO_2NO_2 \cdot I^-$) are both proportional to $I^- \cdot H_2O$ signal (Figure 3.3) as both ion cluster are formed via ligand exchange reactions (R3.5, R3.8), and thus their sensitivity ratio is constant with the humidity. This facilitates the calibration as it is unnecessary to replicate the humidity in the field when determining their sensitivity ratio.

The sensitivities to HO_2NO_2 ($HO_2NO_2 \cdot I^-$ channel) were calibrated to be ~25 $Hz \cdot pptv^{-1}$ and ~15 $Hz \cdot pptv^{-1}$ respectively in both seasons. The limit of detection (LOD) for CIMS has been estimated based upon the standard deviation of the variations of background signals [e.g., *Neuman et al.* 2002; *Liao et al.*, 2011a]. Here, the LOD is defined as twice the standard deviation (3σ) of the background variation. The LODs of HO_2NO_2 for both seasons were 0.3 pptv and 0.9 pptv, respectively, based on 1-min integration time. The uncertainties for HO_2NO_2 measurement were 22% in winter and 16% in summer.

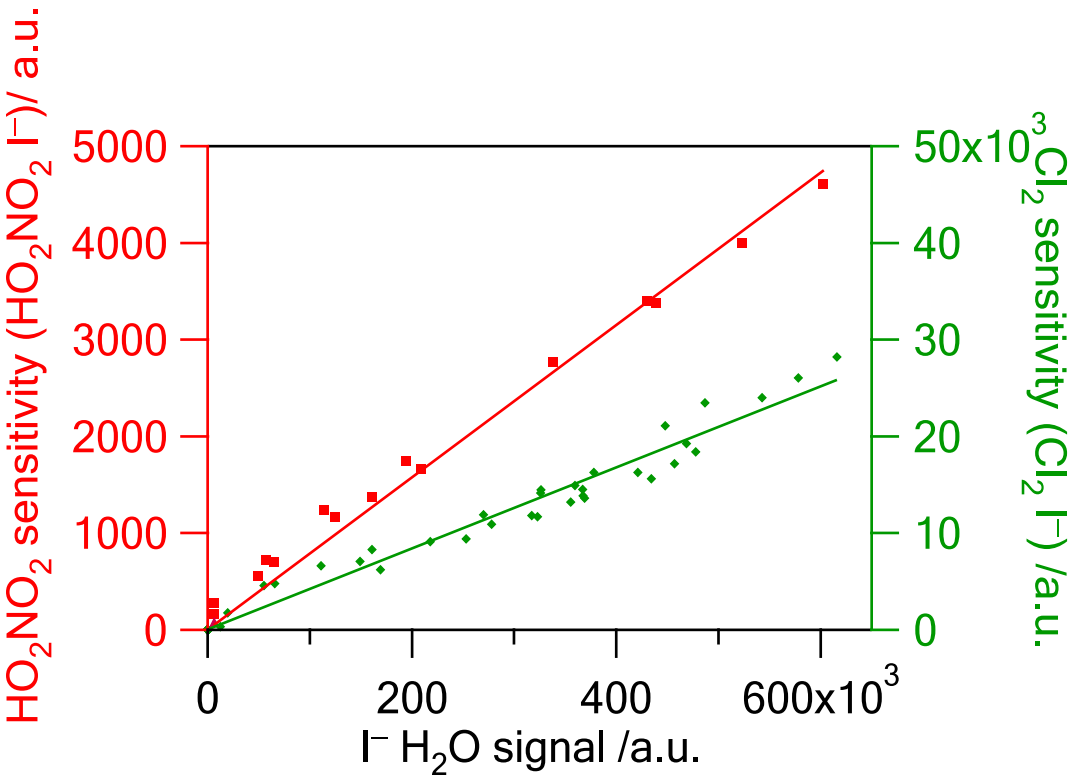

Figure 3.3. The sensitivities towards HO_2NO_2 (as $HO_2NO_2 \cdot I^-$) and Cl_2 (as $Cl_2 \cdot I^-$) as functions of to $I^- \cdot H_2O$, both are proportional to $I^- \cdot H_2O$.

3.2.3 Inference of HO_2

HO_2NO_2 observations were combined with measurements of NO_2 and temperature to infer HO_2 levels from Equation 1. HO_2NO_2 data were excluded during precipitation events, as they perturbed the equilibrium, or if they were below the LOD. All NO_2 data were well above the LOD.

Different averaging times were applied to infer HO_2 at different temperatures. Temperature ranged from −4.7°C to 24.5°C during the winter observation, and 18.8°C to 37.6°C during the summer observation. The lifetime of HO_2NO_2 and thus the time scale to

approach equilibrium varied. Also, NO_x emitted by traffic (especially traffic on the highway nearby) fluctuated, which can perturb the HO_2NO_2 equilibrium.

The 0-D time-dependent model was used to determine the averaging time. The model setup is detailed in Table 3.2. Model calculations were performed constrained by measured NO_x and O_3 from 1 December 2014, 20:00 to 3 December 2014, 20:00, when variations of NO_x were especially pronounced. Model simulations were performed for this period for a set of assumed temperatures. HO_2 was simulated directly from the model, and also inferred HO_2 from the model simulated HO_2NO_2. Both the simulated and inferred HO_2 concentrations were averaged on different time scales and compared. Figure 3.4 shows the results. At −5°C, 10 min averages of inferred and simulated HO_2 agree within 10% (slope = 0.899, r = 0.976); at 5°C, 5 min averages of inferred and simulated HO_2 agree within 5% (slope = 0.955, r = 0.988); at 15°C, 1-min averages of inferred and simulated HO_2 agree within 3% (slope = 0.975, r = 0.985). Thus, the average time of 10 min was selected for $-5°C \leq T < 5°C$, 5 min for $5°C \leq T < 15°C$, and 1min for $T \geq 15°C$.

The uncertainty for HO_2 inferred from HO_2NO_2 observations has multiple sources. The equilibrium constant K in Equation (2.1) has a 30% uncertainty in the temperature range of the observations [*Burkholder et al.*, 2015; *Christensen et al.*, 2004; *Gierzcak et al.*, 2005; *Bacak et al.*, 2011], and is the major uncertainty source. The uncertainties of the HO_2NO_2 and NO_2 measurements are listed in Table 3.1. Combining these effects gives a total uncertainty of 39% in the winter observation and 35% in the summer observation for inferred HO_2.

Table 3.2. Summary of the time-dependent model.

	Species/Parameters
constrained	T[a], p[b], O_3[c], NO[c], NO_2[c], H_2O(v)[d], CO[d], CH_4[d], C_2H_6[d], C_3H_8[d], CH_2O[d], $CH_3C(O)CH_3$[d], j values[e],
Time-dependent	HO_2NO_2[f], N_2O_5[f], HONO[f], PAN[f]
Steady-state	OH, HO_2, CH_3O_2, $CH_3C(O)O_2$, NO_3

a. Fixed to different values for each run.
b. Fixed to be 100 kPa.
c. Constrained by measurements
d. fixed concentrations: [H_2O(v)] = 8000 ppmv, [CO] = 100 ppbv, [CH_4] = 1.8 ppmv, [C_2H_6] = 1 ppbv, [C_3H_8] = 500 pptv, [CH_2O] = 1 ppbv, [$CH_3C(O)CH_3$] = 2 ppbv.
e. Estimated using the NCAR TUV model (https://www2.acom.ucar.edu/modeling/tropospheric-ultraviolet-and-visible-tuv-radiation-model).
f. Initial concentrations for time-dependent species: $[HO_2NO_2]_0$ = 2 pptv, $[N_2O_5]_0$ = 50 pptv, $[HONO]_0$ = 1 ppbv, $[PAN]_0$ = 1 ppbv.

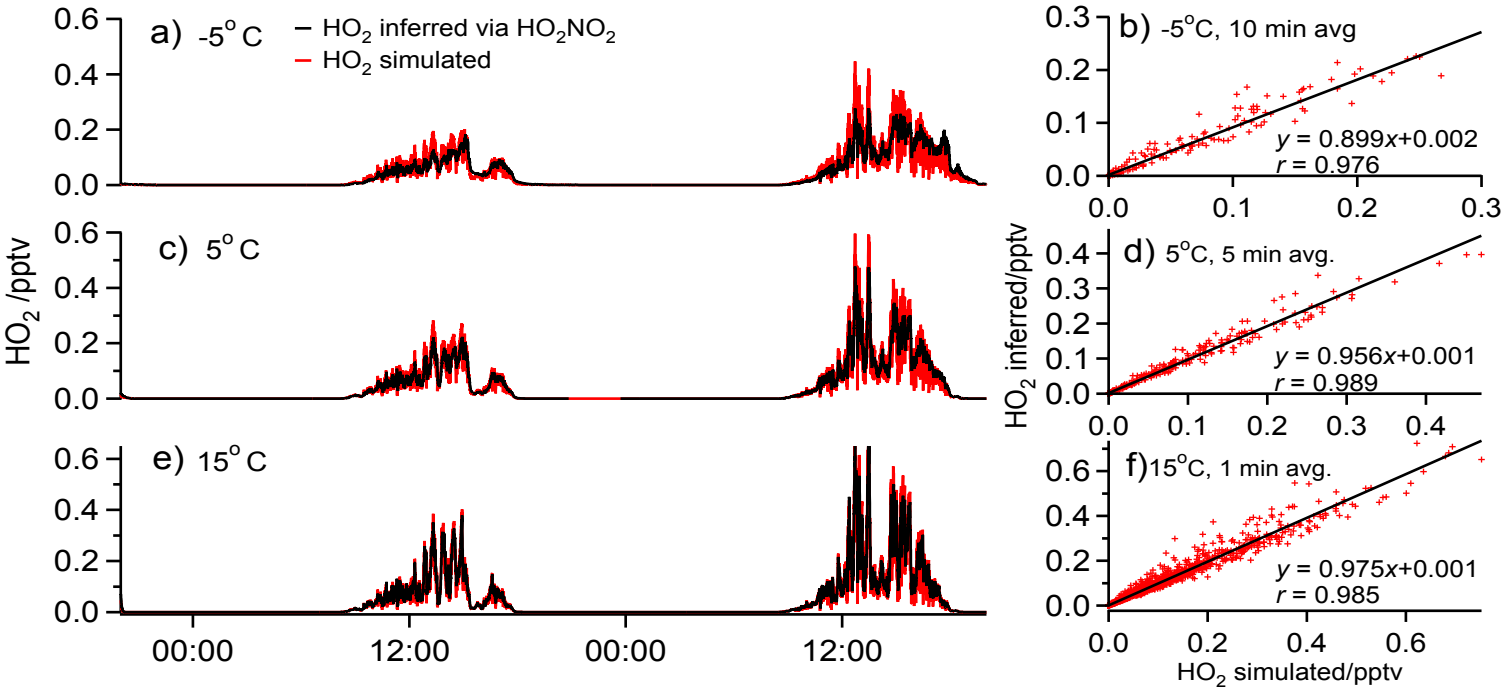

Figure 3.4. To determine the averaging time for the inference of HO_2, HO_2NO_2 and HO_2 were simulated using a time-dependent model for a period of 24 h, with $\Delta t = 10$ s, at −5°C, 5°C, and 15°C (panel a, c, d). In panel a, c, and d, time series of inferred HO_2 via simulated HO_2NO_2 is plotted in red, and simulated HO_2 is plotted in red. The inferred and simulated HO_2 levels were averaged on different time scales and compared (panel b, d, f).

3.2.4 Model calculation of HO_2

The 0-D steady-state model was used to estimate HO_2 to compare to inferred HO_2. The model setup is listed in Table 3.3. The chemistry scheme is listed in the supplement. The model included detected species and meteorological parameters. VOC, HONO, and H_2O_2 were not measured. Concentrations of basic VOC (C_2H_6, C_3H_8, C_2H_4, C_3H_6, CH_2O, CH_3OH, CH_3CHO, peroxyacetyl nitrate (PAN), $CH_3C(O)CH_3$, $CH_3C(O)CH_2OH$, $CH_3C(O)CHO$, isoprene, methacrolein (MACR), methyl vinyl ketone (MVK), benzene, toluene), HONO, and H_2O_2 were estimated using the 3-D Regional chEmical and trAnsport Model (REAM). Details of REAM can be found in previous studies [*Choi et al.*, 2005; *Jing et al.*, 2006; *Wang et al.*, 2006; *Liu et al.*, 2010; *Zhao et al.*, 2010]. *j* values were calculated using the NCAR TUV model (https://www2.acom.ucar.edu/modeling/tropospheric-ultraviolet-and-visible-tuv-radiation-model), and scaled using measured solar UV radiations. The model was run twice. Run_1 was not constrained by measured HO_2NO_2 but calculated HO_2NO_2 to steady state. Run_2 included HO_2NO_2 as a constraint. Since HO_2 was inferred based on HO_2NO_2, we here have a comparison and examine how the constraint of HO_2NO_2 influences the model simulation result.

Table 3.3. Species and parameters for the steady-state model prediction of HO_2.

	Species/Parameters
constrained (measured)	T, p, O_3, H_2O(v), CO, NO, NO_2, HO_2NO_2[a], N_2O_5[b],
constrained (modeled/assumed)	j values[c], CH_4[d], C_2H_6[e], C_3H_8[e], C_2H_4[e], C_3H_6[e], CH_2O[e], CH_3OH[e] CH_3CHO[e], PAN[e], $CH_3C(O)CH_3$[e], $CH_3C(O)CH_2OH$[e], $CH_3C(O)CHO$[e], isoprene[e], $CH_3C(O)CH=CH_2$ (MVK)[e], $CH_2=C(CH_3)CHO$ (MACR)[e], benzene[e], toluene[e], , HONO[e], H_2O_2[e]
predicted by the model	OH, HO_2, CH_3O_2, $C_2H_5O_2$, $C_2H_4(OH)O_2$, $CH_3C(O)O_2$, $CH_3C(O)CH_2O_2$, Isop$(OH)O_2$[f], $MOHO_2$[g], MCO_3[h], ArO_2[i], $R(NO_3)O_2$[j], NO_3, CH_3OOH,

a. Predicted by the steady-state model in Run_1; constrained by measurements in Run_2 (see text).
b. Constrained by measurement in the winter observation; estimated using the REAM model in the summer observation.
c. Estimated using the NCAR TUV model, scaled using the measured UV radiation.
d. CH_4 was fixed to be 1.8 ppmv.
e. Estimated using the REAM model.
f. Hydroxylperoxy radicals derived from the OH-initiated oxidation of isoprene.
g. Hydroxylperoxy radicals derived from the OH-initiated oxidations of MACR/MVK.
h. $CH_2=C(CH_3)C(O)O_2$.
i. Peroxy radicals derived from the oxidation of benzene and toluene.
j. Peroxyl radicals derived from the NO_3-alkene addition reactions.

3.3 Results and discussions

Figure 3.5 shows time series of HO_2NO_2, NO_2, temperature, and inferred HO_2. In winter, HO_2NO_2 ranged up to 21.1 pptv (average 3.7 pptv), NO_2 ranged up to 60.1 ppbv (average 17.0 ppbv), and inferred HO_2 ranged up to 3.5 pptv (daytime average 0.17 pptv). In summer, HO_2NO_2 ranged up to 90.3 pptv (average 11.7 pptv), NO_2 ranged up to 64.6 ppbv (average 11.3 ppbv), and inferred HO_2 ranged up to 89.3 pptv (daytime average 10.4 pptv). Figure 3.6 shows mean diurnal profiles of HO_2. Peak values of HO_2 profiles were 0.19 pptv in winter, and 20.0 pptv in summer. Although unique to Atlanta, these HO_2 levels are similar to those observed in the same seasons at polluted sites [*Kanaya et al.*, 2007; *Martinez et al.*, 2003; *Ren et al.*, 2006; *Shirley et al.*, 2006]. The following sections focus on two test cases and model comparisons to determine if the inferred HO_2 is reasonable.

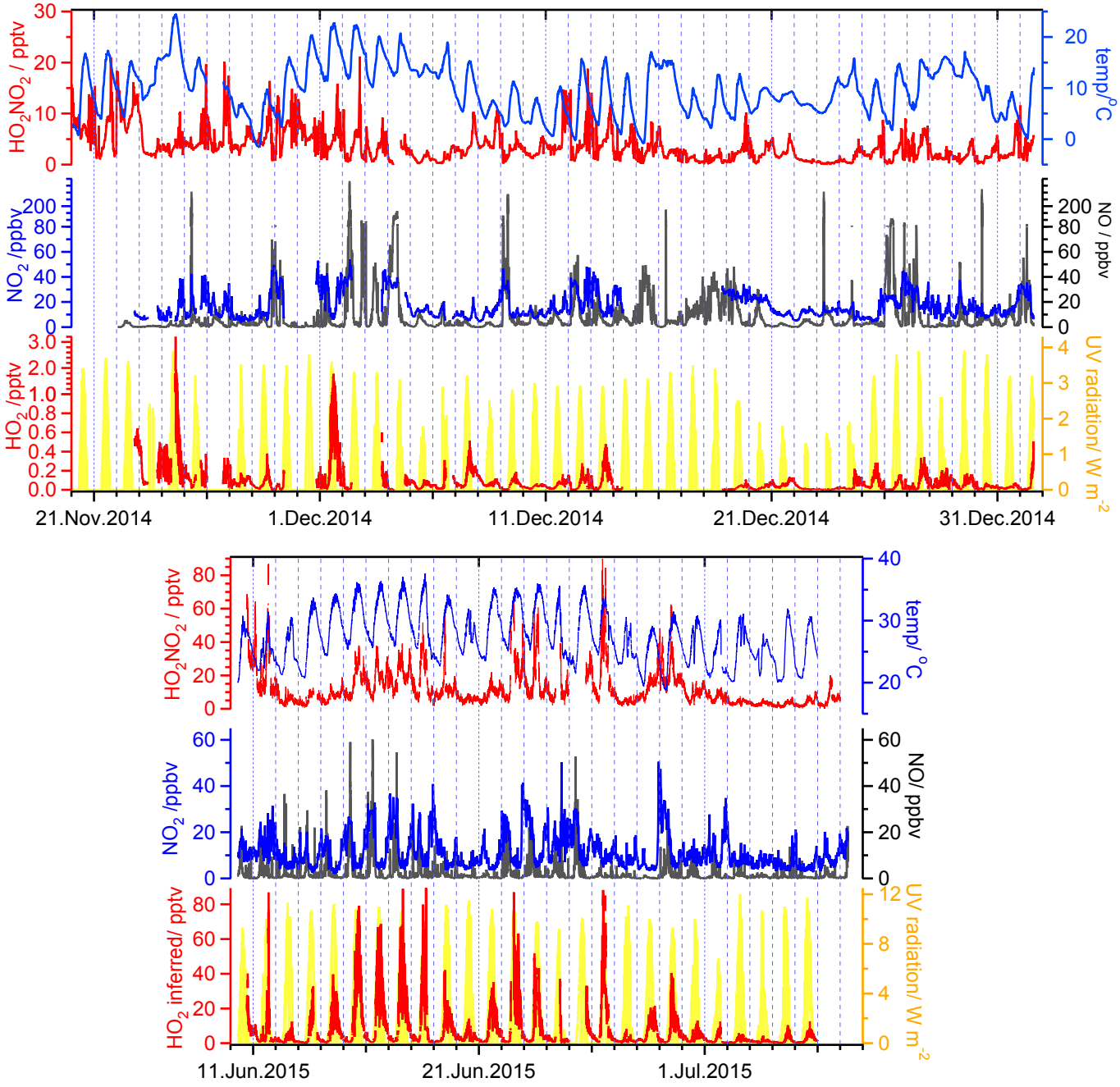

Figure 3.5. Time series of HO_2NO_2, NO_2, NO, temperature, UV radiation, and inferred HO_2 in both winter and summer observations.

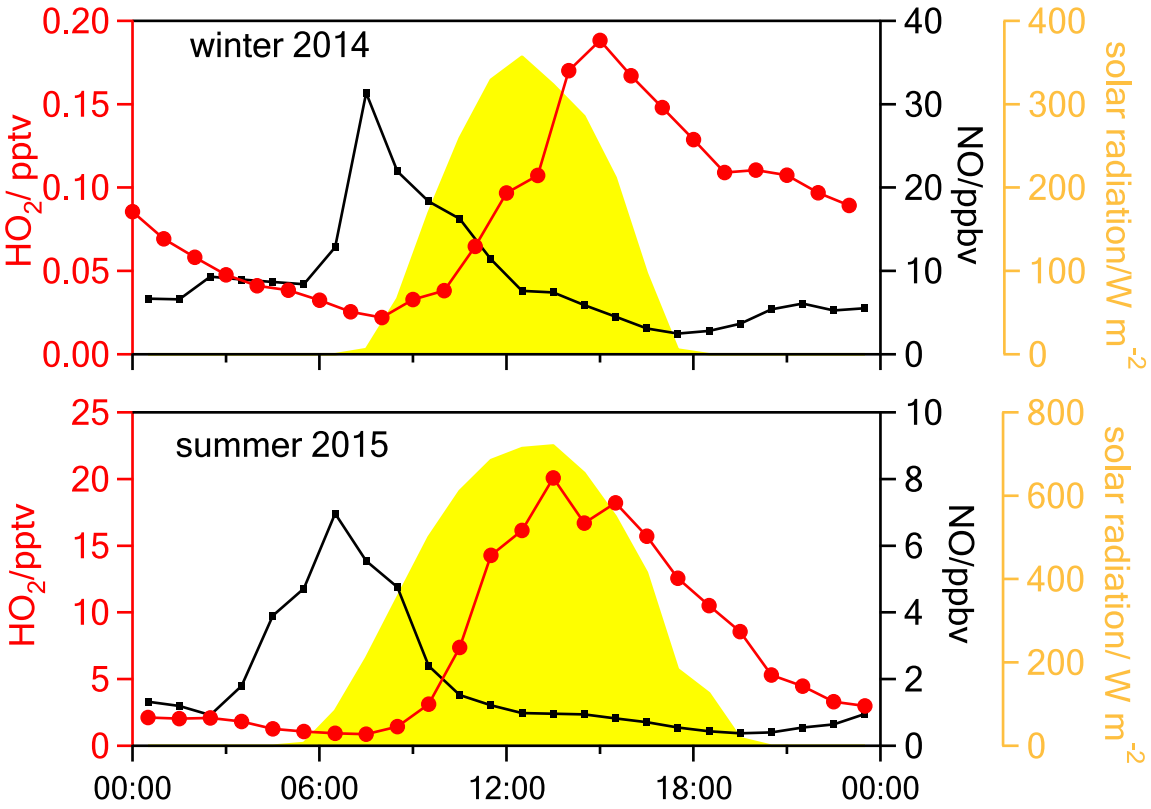

Figure 3.6. Diurnal profiles of HO_2, NO, and solar radiation. HO_2 is suppressed by NO during the morning rush hour.

3.3.1 Suppression of HO_2 at high NO

HO_2 can be efficiently suppressed at high NO due to the fast reaction of HO_2 with NO. The most obvious suppression of HO_2 occurred during morning rush hour, as seen in Figure 3.6. In both seasons, the peak of NO in the morning corresponds to a minimum in HO_2, resulting in asymmetric diurnal profiles, although the radical production is expected be symmetric as it likely driven by solar radiation. A similar behavior was observed in urban areas by *Holland et al.* [2003] and *Martinez et al.* [2003].

Low HO_2 associated with high NO was oftentimes observed in both seasons, during other periods besides rush hour. Figure 3.7 displays two examples of the suppression of HO_2 at high NO peaks. On 26 – 27 Dec 2014. HO_2 decreased at high NO multiple times (20:00 −23:00, 03:00 – 06:00, 07:40− 08:30, 09:00 – 14:00). On 20 June 2015, HO_2 was around 1 pptv during 17:00 – 18:00 while NO while NO reached 12 ppbv, then HO_2 recovered to ~6 pptv after NO dropped to ~ 1 ppbv. In all, the inferred HO_2 responded to NO in the manner expected.

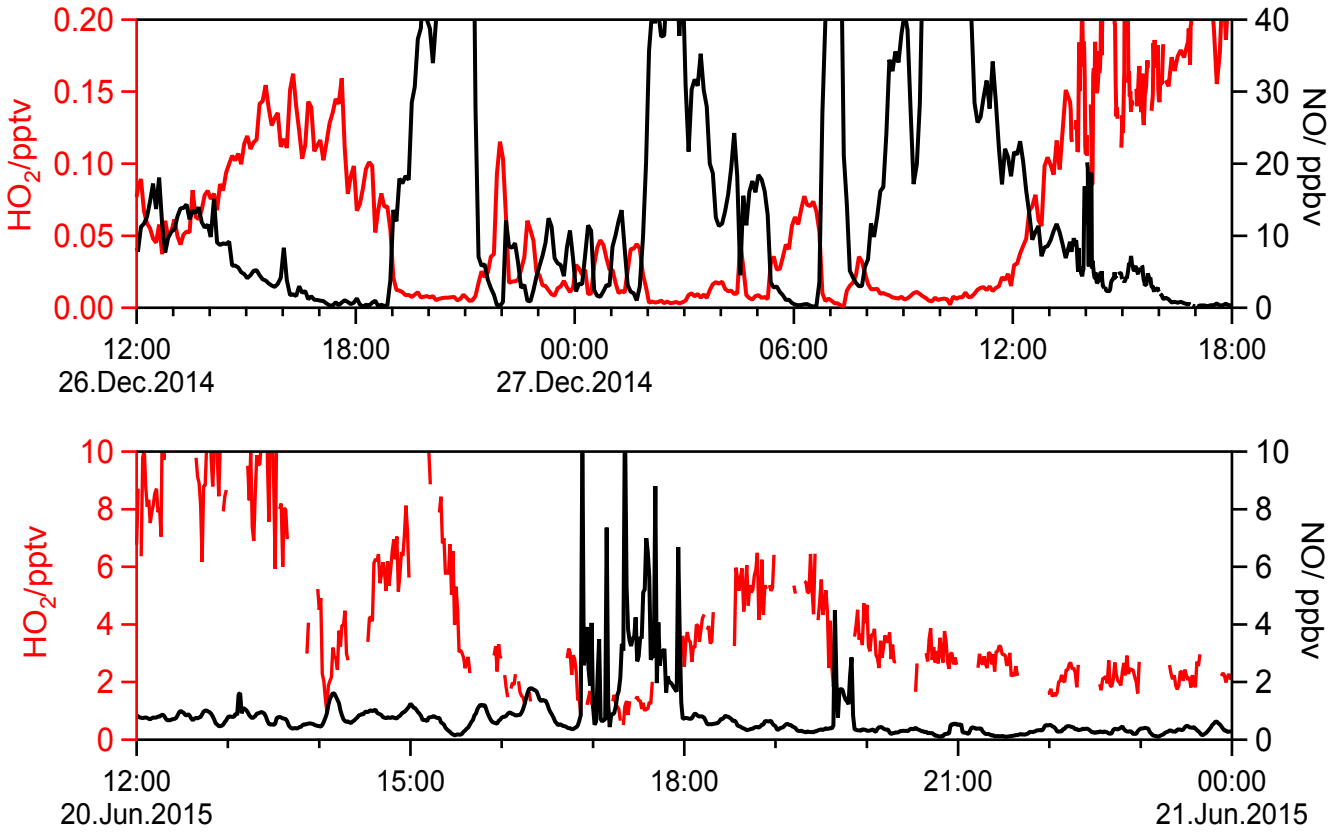

Figure 3.7. Examples of the suppression of HO_2 at high NO.

3.3.2 Correlations between HO_2 and O_3/NO_3 at night

Nighttime HO_x has been reported by a variety of research [e.g., *Commane et al.*, 2010; *Geyer et al.*, 2003]. During the night HO_2 is probably largely produced by VOC ozonolysis and oxidation by NO_3 [*Atkinson and Carter*, 1984; *Wayne et al.*, 1991; *Paulson and Orlando*, 1996; *Johnson and Marston*, 2007; *Brown et al.*, 2009; *Sommariva et al.*, 2009, 2011]. The correlation between nighttime HO_2 and O_3 in both seasons was examined. In addition, the correlation between nighttime HO_2 and NO_3 in the winter was investigated by using N_2O_5 observations to estimate $[NO_3]$:

$$[NO_3] \approx \frac{k_{N_2O_5}[N_2O_5] + k_{NO_2+O_3}[NO_2][O_3]}{k_{NO_3+NO_2}[NO_2] + k_{NO_3+NO}[NO]} \qquad (2.\ 2)$$

where k_{N2O5} is the unimolecular thermal decomposition rate of N_2O_5.

HO_2 was moderately correlated to O_3 at nights for the both seasons. $r(HO_2\text{-}O_3)$ = 0.68 in the winter observation, and 0.67 in summer. The correlation with NO_3 was found to be less, $r(HO_2\text{-}NO_3)$ = 0.27 in winter. However, if a filter of NO < 1 ppbv is applied, as high NO can suppress HO_2, O_3 and NO_3, $r(HO_2\text{-}O_3)$ = 0.59 in winter and 0.47 in summer, and $r(HO_2\text{-}NO_3)$ = 0.67 in winter.

Strong correlations between HO_2 and O_3/NO_3 were also observed on some nights. For instance, as seen in Figure 3.8, during 18:30− 01:30 on the night of 1 –2 December, 2014, most of the time NO < 1 ppbv, HO_2, O_3 and NO_3 all showed similar patterns. $r(HO_2\text{-}O_3)$ = 0.89, and $r(HO_2\text{-}NO_3)$ = 0.86. Also, as seen in Figure 3.9, during 20:00 – 05:00 on the night of 30 June – 1 July, 2015, NO was generally less than 1 ppbv, $r(HO_2\text{-}O_3)$ = 0.90.

These strong correlations suggest that O_3 and NO_3 are driving the production of HO_2 on these nights.

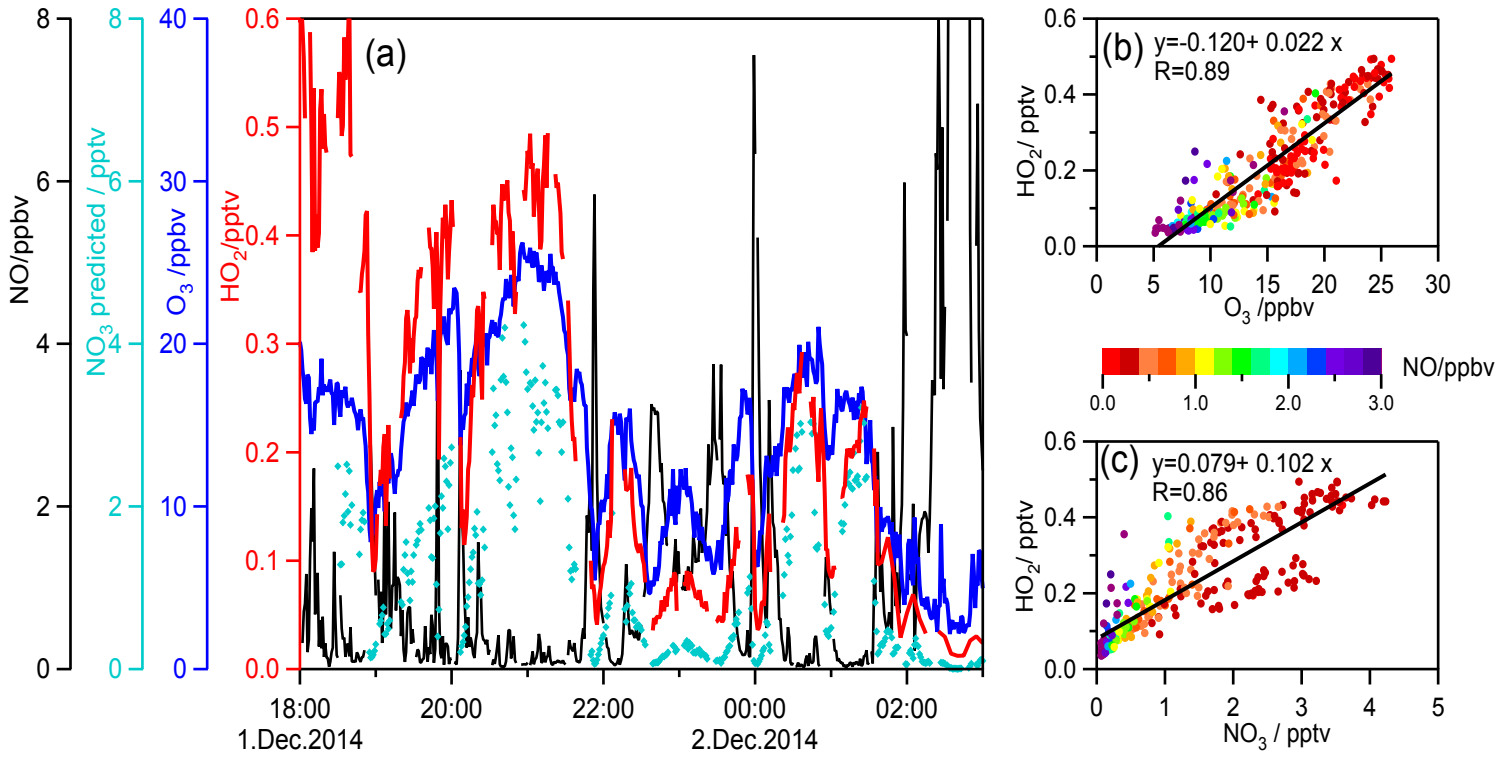

Figure 3.8. Strong correlations between HO_2 and O_3/NO_3 during 18:30 − 01:30 on the night of 1 – 2 December, 2014.

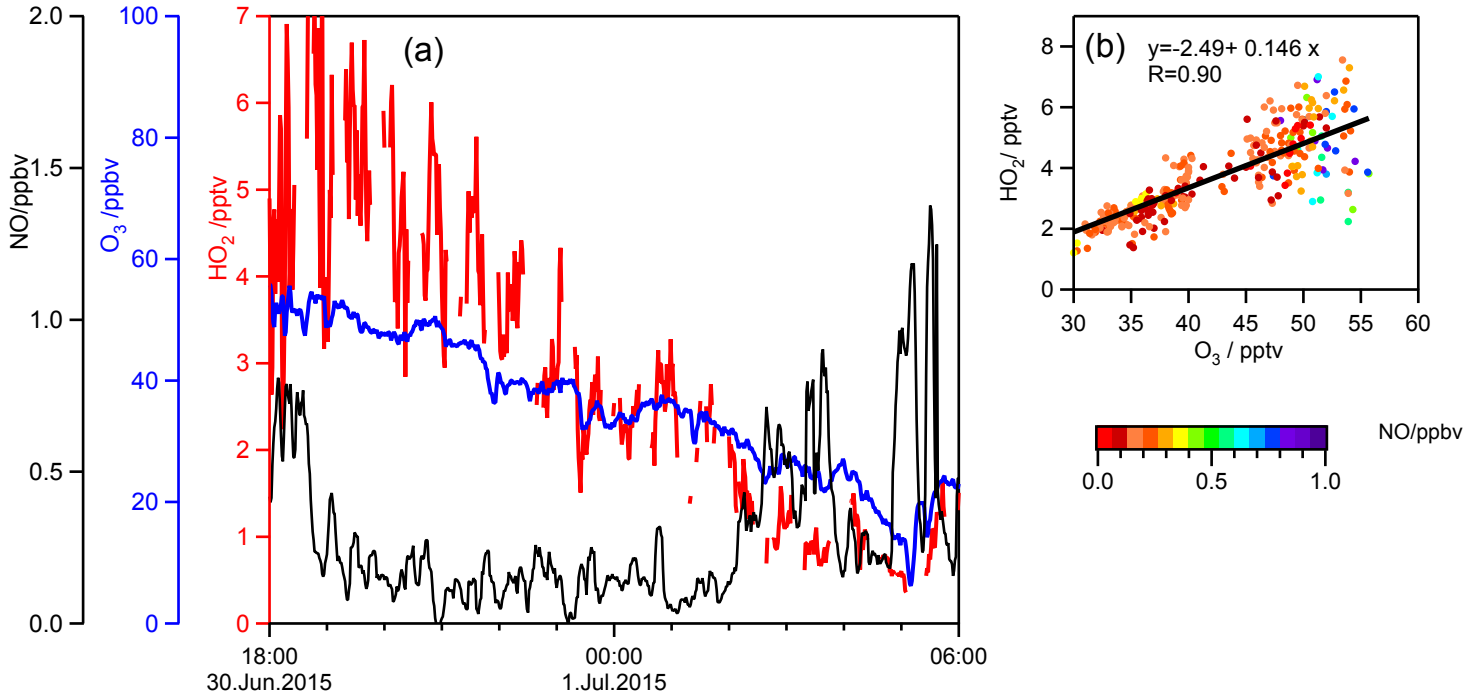

Figure 3.9. Strong correlation between HO_2 and O_3 during 20:00 – 05:00 on the night of 30 June – 1 July, 2015.

3.3.3 Comparison of inferred and modeled HO_2.

Figure 3.10 compares the inferred HO_2 with model predicted HO_2 (Run_1 and Run_2). Discrepancies between model simulations and inferred HO_2 are expected, since (1) the model was not constrained by measured VOC, H_2O_2, HONO, and *j* values, (2) the HO_x chemistry in polluted regions is complicated, perhaps even more so in Atlanta with significant isoprene emissions, and (3) previous studies have suggested missing (unknown) source/sink of HO_x in polluted regions especially at night [e.g., *Ren et al.*, 2003; *Kanaya et al.*, 2007, 2012]. Nevertheless, Run_1 still captures the basic features of inferred HO_2. For Run_1, the average modeled-to-inferred ratio (M/I) is 1.27 (r = 0.54) for winter and 0.70 (r = 0.80) for summer. For the summer observations, Run_1 tends to underestimate nighttime HO_2, which suggests that more sources of HO_2 may exist than included in the model.

With the constraint of HO_2NO_2, Run_2 predicted HO_2 with average M/I = 1.13 (r = 0.77) for winter, and average M/I = 0.90 (r = 0.97) for summer. Run_2 slightly improved M/I for the winter season, and largely improved M/I for the summer season. The large improvement of M/I in summer is due to fast decomposition of HO_2NO_2, which was an important source of HO_2 in Run_2. Nevertheless, considering the relatively loose constraints, both runs are in reasonable agreement with the inferred HO_2.

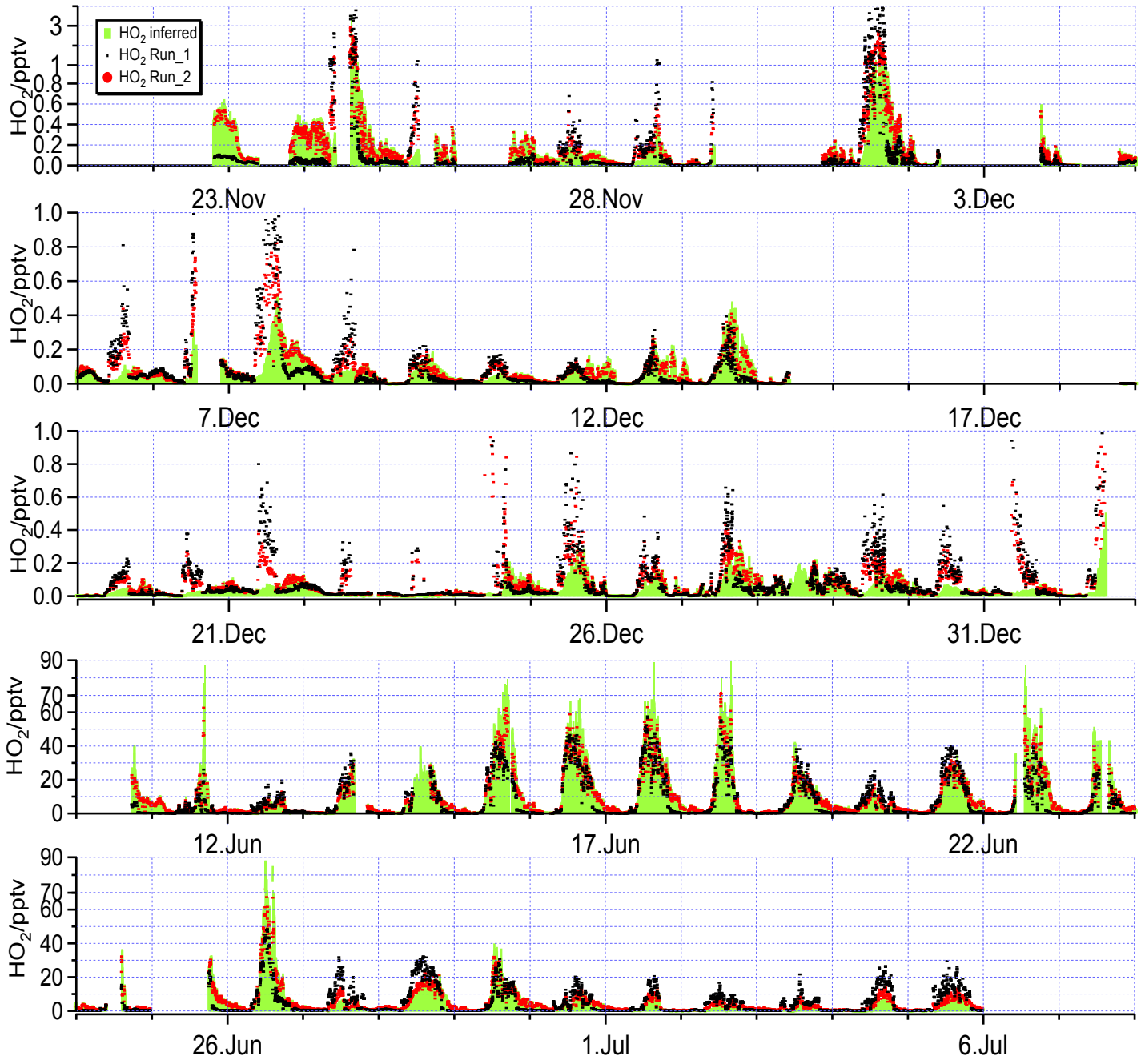

Figure 3.10. Comparison between the inferred and modeled HO_2. The model was run twice: Run_1 was not constrained by measured HO_2NO_2 while Run_2 was.

3.4 Conclusions

Chemical ionization mass spectrometry (CIMS) was employed to measure HO_2NO_2 in Metropolitan Atlanta in winter 2014 and summer 2015, and derive HO_2 concentrations. The total uncertainty for inferred HO_2 was 39% for the winter observation, and 35% for the summer observation. Inferred HO_2 ranged up to 3.5 pptv (daytime average 0.17 pptv) in the winter observation, and up to 89.3 pptv (daytime average 10.4 pptv) in the summer observation. The mean diurnal profile of inferred HO_2 has a peak value of 0.19 pptv in winter, and 20.0 pptv in summer. Inferred HO_2 was suppressed at high NO as expected, especially during morning rush hours. Significant nighttime HO_2 was observed, and was found to correlate to O_3 and/or NO_3, indicating the important role of O_3 and NO_3 in nighttime HO_2 production. Inferred HO_2 was compared to model calculations constrained by measured and model-estimated species/parameters. Inferred and model calculated HO_2 reasonably agreed with each other. These results show that it is a feasible method to infer HO_2 via HO_2NO_2 measurement in warm environments when HO_x measurements are unavailable. Future work should focus on (1) inter-comparison with HO_2 measurement techniques such as lacer-induced fluorescence (LIF) [e.g., *Fuchs et al.*, 2008], and (2) model calculation of HO_2 with a much better constrained dataset.

3.5 Acknowledgements

The meteorological data were provided by the Atlanta Midtown Weather Station, co-located on top of the Ford ES&T building. I thank James R. Hite Jr. for processing the meteorological data, and Dr J. Michael Nicovich for synthesizing NO_2 and recalibrating a NO_2/N_2 standard.

CHAPTER 4. AIRBORNE MEASUREMENTS OF BROMINE MONOXIDE AND THE SUM OF HYPOBROMOUS ACID AND DIBROMINE OVER THE TROPICAL WEST PACIFIC DURING THE CONVECTIVE TRANSPORT OF ACTIVE SPECIES IN THE TROPICS (CONTRAST) EXPERIMENT

4.1 Introduction

Bromine species are important ozone-depleting substances [e.g., *Daniel et al.*, 1999; *World Meteorological Organization* (*WMO*), 2011, 2014; *Wennberg et al.*, 1994; *Salawitch et al.*, 2005]. Bromine destroys ozone (O_3) much more effectively than chlorine [e.g., *Daniel et al.*, 1999; *Danilin et al.*, 1996]. Current estimates of the stratosphere bromine burden ranges from 16 to 23 pptv, which is roughly 150 times lower than stratospheric chlorine [*WMO*, 2014]. However, bromine accounts for 20 to 40% of the ozone (O_3) loss in the lowermost stratosphere (LMS) at mid-latitudes [*Lee et al.*, 2002], and ~ 50% of the O_3 loss in the Antarctic ozone hole [e.g., *Lee et al.*, 2002; *Danilin et al.*, 1996; *Frieler et al.*, 2006; *Salawitch et al.*, 1993]. Consequently, even low concentrations of Br_y have a relatively large impact on O_3 [*Salawitch et al.*, 2005].

The input of inorganic bromine (collectively known as Br_y, $Br_y = Br + BrO + HOBr + BrNO_3 + 2\times Br_2 + BrCl + HBr$) to the stratosphere contributes 1.1 to 4.3 pptv of its bromine burden [*Carpenter et al.*, 2014; *Montzka et al.*, 2011]. The input of Br_y to the stratosphere is usually termed product gas injection (PGI) of bromine species and the input of bromocarbons (CBr_y) to the stratosphere is termed source gas injection (SGI) of bromine

species. The most important PGI pathway is thought to be in the tropics; the Western Pacific plays a particularly important role due to the deep convection in this region [e.g., *Pan et al.*, 2016]. Deep convection transports Br_y from the marine boundary layer (MBL) and tropical free troposphere (TFT) (1 to 12 km) to the tropical tropopause layer (TTL) (~12 to 17 km) and subsequently to the LMS [*Aschmann et al.*, 2009; *Ashfold et al.*, 2012; *Fernandez et al.*, 2014; *Levine et al.*, 2007; *Tegtmeier et al.*, 2012; *Sinnhuber and Folkins*, 2006]. The release of Br_y from saline aerosols in the lower part of the troposphere, and the degradation of very short lived bromocarbons (CBr_y^{VSL}) throughout the troposphere and the TTL serve as sources of Br_y [e.g., *Ko et al.*, 1997; *Orlando*, 2003; *Yang et al*., 2005; *Salawitch*, 2006; *Hossaini et al.*, 2010;]. CBr_y^{VSL} are bromocarbons with tropospheric lifetimes less than half a year (e.g. $CHBr_3$ and CH_2Br_2), which are primarily produced by marine algae [e.g., *Tegtmeir et al.*, 2012; *Warwick et al.*, 2006]. In addition, the transport of Br_y is modified by the partitioning of Br_y (Table 4.1) [e.g., *Parrella et al.*, 2012; *Fernandez et al.*, 2014], since (1) soluble species such as HOBr, $BrNO_3$ and HBr are subject to loss by scavenging (Table 4.1, R4.17 – 4.19) in the troposphere before being delivered to the stratosphere, and (2) heterogeneous chemistry can recycle Br_y back to the gas phase (Table 4.1, R4.20 – 4.23) and thus partially compensate for the impact of scavenging [*Iraci et al*., 2005; *Fernandez et al*., 2014]. For these reasons, the mechanism for PGI from Br_y is complex as it couples biological, chemical, and dynamical processes. Measurements of Br_y in the tropical troposphere are necessary to understand the whole PGI mechanism: the release of Br_y, the transport, the chemistry, and finally the amount of Br_y delivered to the stratosphere.

Table 4.1. The partitioning of Br_y.

	Reaction
R4.1	$Br+O_3 \rightarrow BrO+O_2$
R4.2a	$BrO+BrO \rightarrow Br_2+O_2$
R4.2b	$BrO+BrO \rightarrow Br+Br+O_2$
R4.3	$BrO+h\upsilon \rightarrow Br+O(^3P)$
R4.4	$BrO+HO_2 \rightarrow HOBr+O_2$
R4.5	$BrO+OH \rightarrow Br+HO_2$
R4.6	$BrO+NO_2+M \rightarrow BrNO_3+M$
R4.7	$BrO+NO \rightarrow Br+NO_2$
R4.8a	$BrO+ClO \rightarrow Br+Cl+O_2$
R4.8b	$BrO+ClO \rightarrow Br+OClO$
R4.8c	$BrO+ClO \rightarrow BrCl+O_2$
R4.9	$Br+CH_2O \rightarrow HBr+HCO$
R4.10	$Br+CH_3CHO \rightarrow HBr+CH_3CO$
R4.11	$Br+HO_2 \rightarrow HBr+O_2$
R4.12	$Br_2+h\upsilon \rightarrow Br+Br$
R4.13	$HOBr+h\upsilon \rightarrow Br+OH$
R4.14a	$BrNO_3+h\upsilon \rightarrow Br+NO_3$
R4.14b	$BrNO_3+h\upsilon \rightarrow BrO+NO_2$
R4.15	$BrCl+h\upsilon \rightarrow Br+Cl$
R4.16	$HBr+OH \rightarrow Br+H_2O$
R4.17	$HBr(g) \rightarrow HBr(particle)$
R4.18	$HOBr(g) \rightarrow HOBr(particle)$
R4.19	$BrNO_3(g) \rightarrow BrNO_3(particle)$
R4.20	$BrNO_3 + H_2O \xrightarrow{heterogeneous} HOBr + HNO_3$
R4.21	$HOBr + HBr \xrightarrow{heterogeneous} Br_2 + H_2O$
R4.22	$HOBr + HCl \xrightarrow{heterogeneous} BrCl + H_2O$
R4.23	$HOCl + HBr \xrightarrow{heterogeneous} BrCl + H_2O$

There has been considerable effort to measure tropospheric Br_y, mainly in the extratropical troposphere [*Choi et al.*, 2012; *Dibb et al*., 2010; *Fitzenberger et al*., 2000; *Hebestreit et al.*, 1999; *Hönninger et al.*, 2004; *Liao et al.*, 2011a, 2011b, 2012; *Mahajan et al.*, 2009; *Neuman et al.*, 2010; *Pommier et al.*, 2012; *van Roozendael et al.*, 2002; *Schofield et al.*, 2004]. But neither the distribution nor the partitioning of Br_y is zonally uniform in the troposphere [e.g., *von Glasow et al*., 2004; *Yang et al*., 2005]. To date, limited measurements in the tropical troposphere have solely focused on BrO and have drawn an uncertain picture. Retrieval of BrO from the Scanning Imaging Absorption Spectrometer for Atmospheric Chartography (SCIAMACHY) satellite instrument suggested that the BrO column below 15 km across the equator is equivalent to a uniform distribution of 1 pptv BrO throughout the tropospheric column [*Sinnhuber et al.*, 2005]. On the other hand, SCIAMACHY BrO retrieved in other work suggested the presence of 2 to 4 ppt of BrO in the tropical upper troposphere, with little or no BrO present below 15 km [*Sioris et al.*, 2005]. *Theys et al*. [2007] deduced a maximum 2 to 5 pptv of BrO in the free troposphere above Réunion Island (21°S, 56°E) according to the measured vertical tropospheric BrO column, $(1.1\pm0.45) \times 10^{13}$ molecule·cm^{-2}, by a Differential Optical Absorption Spectroscopy (DOAS). In contrast, another DOAS measurement performed in Teresina, Brazil (5.1°S, 42.9°W) concluded that BrO in the TFT is compatible with zero within the uncertainties of around 1 pptv [*Dorf et al.*, 2008]. In addition, the model simulation by *von Glasow et al.* [2004] suggested that an unknown source of Br_y would need to be assumed in the TFT to explain higher levels of observed BrO. It has also been suggested that the partitioning of Br_y in the TFT and TTL may be shifted to species other than BrO, such as HBr, HOBr, or Br [*Fernandez et al.*, 2014; *von Glasow et al.*, 2004;

Liang et al., 2014; *Yang et al*., 2005]. Thus, a small amount of BrO observed in the TFT and TTL can reflect the presence of a much higher amount of Br_y. Consequently, the assessment of PGI requires observations of a wider suite of inorganic bromine species in the tropics.

The CONvective TRansport of Active Species in the Tropics (CONTRAST) experiment was an airborne investigation utilizing the NCAR Gulfstream-V (GV) aircraft equipped with a suite of chemical and meteorological parameter instruments. The CONTRAST flights were based out of Guam (13.5°N, 144.6°E) during January and February, 2014. A complete description of the CONTRAST experiment is detailed in the overview paper [*Pan et al.*, 2016]. A primary scientific objective was to study the chemistry of Br_y and the transport of Br_y into the TTL and LMS over the tropical Western Pacific Ocean. During CONTRAST, BrO and the sum of Br_2 and HOBr ($HOBr+Br_2$) were measured using a chemical ionization mass spectrometer (CIMS). These results represent some of the first observations of Br_y species other than BrO in the tropics. Observations of both BrO and $HOBr+Br_2$ can provide more information for the assessment of local Br_y chemistry and PGI.

4.2 Measurements

A suite of instruments used during CONTRAST are listed in Table 4.2. The dynamical and chemical models for forecasting and flight planning are documented in the CONTRAST field catalog (http://catalog.eol.ucar.edu/contrast) and described in *Pan et al.* [2016]. This section focuses on the CIMS employed for measurements of BrO and HOBr+Br_2.

Table 4.2. Measurements of species and meteorological parameters relevant to this study.

Instruments	Measured species / parameters	PI/Institutions
CIMS	BrO, HOBr+Br_2, N_2O_5	Huey/GA Tech
Chemiluminescence	O_3	Weinheimer/NCAR
Chemiluminescence	NO, NO_2	Weinheimer/NCAR
Vacuum UV Fluorescence	CO	Campos/NCAR
Picarro WS-CRDS[a]	CH_4, CO_2	Campos/NCAR
TOGA[b]	VOCs/bromocarbons/HCN	Apel/NCAR & Riemer/U Miami
AWAS[c]	VOCs/bromocarbons	Atlas/U Miami
ISAF[d]	CH_2O	Hanisco/NASA
HARP[e]	actinic flux	Hall/NCAR
VCSEL[f]	H_2O vapor	Jensen/NCAR
2DC[g]	cloud droplets (12.5-3200 μm)	Jensen/NCAR
CDP[h]	particle (2-50 μm)	Jensen/NCAR
UHSAS[i]	particle (0.06-1 μm)	Jensen/NCAR
GV platform	time, location, *T*, *p*, Wind	Jensen/NCAR

a. Wavelength-Scanned Cavity Ring-down Spectroscopy.
b. Trace Organic Gas Analyzer
c. Advanced Whole Air Sampler
d. In-Situ Airborne Formaldehyde
e. HIAPER Airborne Radiation Package.
f. Vertical-Cavity Surface-Emitting Laser hygrometer.
g. 2-Dimentional optical array Cloud probe.
h. Cloud Droplet Probe.
i. Ultra-High Sensitivity Aerosol Spectrometer.

4.2.1 CIMS

The CIMS instrument used here is very similar to that described by *Kim et al.* [2007] and *Liao et al.* [2011a]. Here gives a briefly description of the configuration of the CIMS used in this experiment (Figure 4.1) and how it differed from earlier versions. As in previous work, the CIMS was comprised of the following differentially pumped regions: a flow tube, a collisional dissociation chamber (CDC), an octopole ion guide, a quadrupole mass filter and an ion detector. During CONTRAST, smaller turbo pumps were used to evacuate the octopole and quadrupole regions (i.e. Varian Turbo-V70 instead of Varian Turbo-V300), to reduce size, weight, and power consumption of this instrument relative to previous versions. In addition, the flow tube was elongated to ~20 cm and the operating pressure was increased from 20 to 50 torr to maximize the sensitivity of the CIMS to BrO species. This increased the concentrations of both the reagent ion and measured species in the flow tube while also increasing reaction time. This resulted in an increase in sensitivity for BrO from ~ 3 $Hz \cdot pptv^{-1}$ to ~10 $Hz \cdot pptv^{-1}$. In previous studies, an orifice of fixed area was used to the front of the flow tube to sample air. For an orifice of fixed area, the sampled volumetric flow (in $L \cdot min^{-1}$) is constant but the sampled mass flow (in slpm) decreases at high altitudes as the pressure decreases, resulting in a decreasing CIMS sensitivity. In CONTRAST, to stabilize the CIMS sensitivity at higher altitudes, an automatic variable orifice (AVO) was used to maintain the sample mass flow. The area of the AVO was controlled by the combination of a microprocessor and stepping motor which moved a polished stainless steel slide to maintain a constant flow tube pressure.

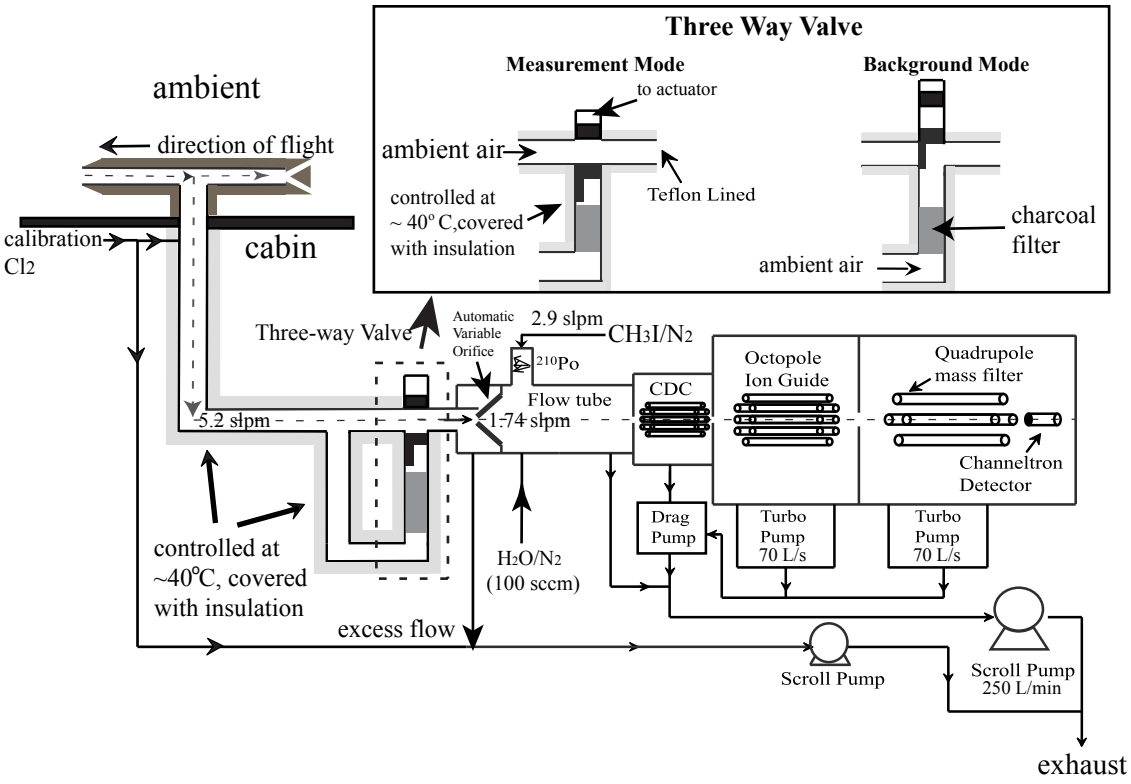

Figure 4.1. The configuration of CIMS used in CONTRAST, adapted from *Liao et al.* [2011a].

4.2.2 Inlet

Ambient air was delivered to the CIMS from a standard GV chemical inlet (Figure 4.1). The inlet probe was a cigar-shaped faring that housed a Teflon™ FEP tube (outer diameter = 1.3 cm, inner diameter = 1 cm, ~1 m long). The whole inlet was maintained at 40°C to keep it warmer than ambient for all flight conditions. At all altitudes, a constant flow of 5.2 slpm was maintained in the inlet tubing, of which 3.5 slpm was exhausted through a mass flow controller and the remaining 1.7 slpm sampled through the AVO.

4.2.3 Ion Chemistry

Hydrated iodide ion ($I^-\cdot(H_2O)_n$) was used as the reagent ion. $I^-\cdot(H_2O)_n$ has been utilized to selectively detect a series of halogen and nitrogen containing compounds [*Huey*, 2007; *Bertram and Thornton*, 2009; *Kercher et al.*, 2009; *Liao et al.* 2011a, 2011b, 2012, 2014; *Neuman et al.*, 2010; *Slusher et al.*, 2004; *Zheng et al*., 2011]. Iodide was produced by flowing 2.9 slpm of N_2 containing a few ppmv CH_3I (99.5%, Alfa Aesar) through a ^{210}Po ion source into the flow tube. In addition, 0.1 slpm of humidified N_2 was introduced separately into the flow tube to ensure that the iodide ion was hydrated throughout the altitude range of the aircraft. In the flow tube targeted species were ionized via the reactions below [*Liao et al.*, 2011a, 2011b, 2012; *Neuman et al.*, 2010]:

(R4.24) $I^-\cdot(H_2O)_n + BrO \rightarrow BrO\cdot I^-$ (*m/z* 222, 224) + nH_2O

(R4.25) $I^-\cdot(H_2O)_n + HOBr \rightarrow HOBr\cdot I^-$ (*m/z* 223, 225) + nH_2O

(R4.26) $I^-\cdot(H_2O)_n + Br_2 \rightarrow Br_2\cdot I^-$ (*m/z* 285, 287, 289) + nH_2O

BrO, HOBr and Br_2 were detected as their corresponding cluster ions with I^- (R4.24 – 4.26). However, it should be noted that the ionization products are expressed as their core

ion forms for simplicity; the water molecules in these clusters were removed in the CDC (Section 2.1). Each product ion has at least two isotopes due to the presence of natural ^{79}Br (50.69%) and ^{81}Br (49.31%), and thus the concentration of each species can be derived from signals at more than one mass. Concentrations of each species were derived from all the detected masses. For each flight, the mass peak with the least noise and/or interference levels was used to derive the concentrations from. However, for most of the experiment *m/z* 222 was used for BrO, *m/z* 225 for HOBr, and *m/z* 287 for Br_2. It should also be pointed out that HOBr can be efficiently converted to Br_2 in the type of inlet used in this study [*Neuman et al.*, 2010]. Hence HOBr+ Br_2 was reported instead of HOBr and Br_2 separately, although under sunlit conditions HOBr is expected to dominate due to the short photolytic lifetime of Br_2.

4.2.4 Background determination

The instrumental background was periodically determined during the research flights (RF) for 1 min out of every 10 min. A custom-made three-way Teflon™ valve was used to switch between measurement mode and background mode (Figure 4.1). In background mode, ambient air passed through an activated carbon scrubber before being introduced into the CIMS. The scrubber was found to remove >99% of targeted species in ambient air. The three-way Teflon™ valve and all tubing were also thermostatted at 40°C.

4.2.5 Calibrations

Since portable standards of BrO and HOBr have not yet been developed, the CIMS instrument was calibrated indirectly. In the field, a known amount of Cl_2 gas from a permeation tube (KIN-TEK) was introduced to the inlet to measure the sensitivity in flights [*Liao et al.*, 2012, 2014].

(R4.27) $I^-\cdot(H_2O)_n + Cl_2 \rightarrow Cl_2\cdot I^-$ (*m/z* 197, 199, 201) + nH_2O

The emission rates of the permeation tube were measured throughout the campaign by a spectrophotometric method [*Wu* et al., 1963; *Kazantseva et al.*, 2002]. After the campaign, the relative sensitivities of BrO, HOBr and Br_2 to Cl_2 were assessed in the laboratory using methods described by *Liao et al*. [2011a, 2012]. The absolute sensitivities of BrO, HOBr and Br_2 were obtained from their relative sensitivity to Cl_2. The calibration uncertainty is 23% for BrO and 25% for HOBr+Br_2, accounting for uncertainties of the emission rate of Cl_2, and the relative sensitivities of BrO, HOBr and Br_2 to Cl_2.

4.2.6 Limit of detection (LOD)

The accurate estimate of the imit of detection (LOD) is very important in this work because ambient levels were near LOD for much of the mission. Commonly, the CIMS LOD is estimated based on the standard deviation of the variation of background signals [e.g., *Liao et al.*, 2011a; *Neuman et al*., 2006]. In this mission, the LOD is defined as 3 times the standard deviation (3σ) of the background variations, and estimated average LODs for each flight (5.2 to 8.1 h long) for BrO and HOBr+Br_2. The LOD of HOBr+Br_2 combines LODs of both HOBr and Br_2 as in Equation 4.1.

$$\mathrm{LOD(HOBr + Br_2)} = \sqrt{[\mathrm{LOD(HOBr)}]^2 + [\mathrm{LOD(Br_2)}]^2} \qquad (4.1)$$

However, it should also be noted that this method may under or overestimate the true LOD when background levels varied more rapidly than the time scale of the background measurements (every 10 min), or are influenced by factors such as cabin temperature. For example, in this study it has been found that background levels were higher if the cabin temperature was warmer than normal. Since concentrations of a species were derived from several masses, for each period of time, the LOD was determined based on the mass used for the derivation of concentration. For all available BrO and HOBr+Br_2 data in CONTRAST, this method gave the 1-min based LOD of BrO ranging between 0.6 and 1.6 pptv, with an average of 1.0 pptv, and a median of 1.1 pptv; and gave the 1-min based LOD of HOBr+Br_2 ranging between 1.3 to 3.5 pptv, with an average of 2.2 pptv, and a median of 2.1 pptv. The LOD of HOBr+Br_2 was higher as it accounts for uncertainties of both HOBr and Br_2.

4.2.7 Interferences

Several interference issues that impacted observations due to the very low levels of halogens measured during CONTRAST. During the first several research flights Br_2 was utilized as the calibration gas to track the sensitivities of CIMS. However, it was found that the Br_2 residual in the inlet could have significantly interfered with measurements of BrO, HOBr and Br_2. For this reason, the calibration gas was switched to Cl_2 and the inlet was rinsed thoroughly before RF09 (5 Feb). No significant interference coming from the Br_2 residual was found on later RFs. NO sign of interference generated by the Cl_2 calibration was found, either. Here, only data from RF 09 to the end of the campaign were reported.

It has also been found that high O_3 levels in the LMS interfered with both HOBr+Br_2 and BrO measurements. Laboratory experiments showed that an unrecognized species, which does not contain bromine atoms appears at *m/z* 222 at high O_3 levels. This species interferes with the measurement of BrO at *m/z* 222. However, the mechanism for producing this and other interfering masses at high O_3 is not certain but may involve chemistry driven by the formation of $O_3 \cdot I^-$ and other ions associated with O_3. The interferences impacted part of the BrO and HOBr+Br_2 data during RF15 (24 Feb). For RF15, no HOBr+Br_2 data were reported when O_3 > ~125 ppbv, and no BrO data were reported when O_3 > ~480 ppbv.

4.3 Photochemical models

Both the steady-state model and the time-dependent model were applied in this study. Br, Br_2, BrO, HOBr, $BrNO_3$ and BrCl have much shorter lifetimes than HBr. Here Br, Br_2, BrO, HOBr, $BrNO_3$ and BrCl are collectively termed photo-reactive Br_y. The steady-state model was used to evaluate the partitioning amongst photo-reactive Br_y. The time-dependent model was used to evaluate the partitioning between HBr and photo-reactive Br_y.

Table 4.3 displays the setup for the steady-state model. Only relatively simple organics were considered as CONTRAST was carried out in a remote and clean environment. NO_2 was calculated assuming steady-state with observed NO, O_3, j_{NO2}, etc., because measurements of NO_2 at higher altitudes was likely interfered with by thermally labile NO_y such as HO_2NO_2 and $CH_3O_2NO_2$, which can decompose to NO_2 in the heated inlet [*Browne et al.*, 2011]. For photo-reactive Br_y, BrO was constrained and others species

are calculated. ClO and BrCl masses were indeed tracked during the campaign, but no significant signals were observed for either compound, although, the LODs for these species were relatively high (LOD(ClO) ~5 pptv, LOD(BrCl) ~2 pptv) as the measurement duty cycles on these masses were short. To estimate BrCl, the models was constrained by estimated Cl and HCl. Briefly, the ratio of [Cl] to [OH] was estimated from regressions of the ratios of various alkanes from *in situ* observations from the TOGA and AWAS instruments (Table 4.2) over a campaign-wide basis. The derived [Cl] to [OH] ratio was then multiplied by [OH] along the flight track, determined from a box model run constrained to various *in situ* observation, to determine the Cl concentration. See *Anderson et al.* [2016b, in preparation] for complete details.

The time-dependent model was run with Δt = 150s. T and p were held at observed values, while j values were parameterized as a function of solar zenith angle (SZA) and altitudes based on the dataset of measured j values. Table 4.4 lists the chemical species and how they are treated. The time-dependent model included the heterogeneous cycling of Br_y but neglected the deposition since the time scale of deposition is much longer than of partitioning [*Parrella et al.*, 2012]. The heterogeneous reaction rate constants were calculated based on measured particle distributions. Background fine particles were considered at all altitude levels and ice particles at T<−20°C. Background fine particles were measured by UHSAS (Table 4.4). There was no specific measurement of ice particles. However, at T<−20°C, it is assumed that particles detected by cloud particle probes (CDP and 2DC, Table 4.2) were ice particles. The Supporting Information provides more details of both models.

Table 4.3. Species included in the steady-state model[a].

	Species
constrained by measurement	O_3, H_2O(v), NO, CO, CH_4, C_2H_6, CH_3OH, CH_2O, CH_3CHO, $CH_3C(O)CH_3$, BrO
Constrained by model output[b]	HCl, Cl
steady-state	$O(^3P)$, $O(^1D)$, OH, HO_2, CH_3O_2, $CH_3C(O)CH_2O_2$, NO_2, HOBr, Br, $BrNO_3$, BrCl, ClO

a. For inorganic chlorine species the model only considered HCl, Cl, and ClO. The interconversions between Cl and ClO were rapid under CONTRAST conditions ($Cl+O_3 \rightarrow ClO+O_2$, $ClO+NO \rightarrow Cl+NO_2$, $ClO+h\upsilon \rightarrow Cl+O(^3P)$) and thus ClO can be estimated assuming steady state with the constraint of Cl.

b. See *Anderson et al.* [2016b].

Table 4.4. Species included in the time-dependent model.

	Species
Constrained[a]	O_3, H_2O(v), CO, CH_4, C_2H_6, CH_3OH, CH_2O, CH_3CHO, $CH_3C(O)CH_3$
Steady-state	$O(^3P)$, $O(^1D)$, OH, HO_2, CH_3O_2, $CH_3C(O)CH_2O$, NO[b], NO_2[b],Cl
Time-dependent	HBr, HCl
Time-dependent & Steady-state[c]	Br, BrO, HOBr, BrCl, $BrNO_3$, ClO, Cl_2O_2, OClO, HOCl, $ClNO_3$

a. constrained species are held at measured values.

b. NO_x is held as the sum of measured NO and calculated NO_2, while the NO/NO_2 partitioning is calculated assuming stead-state.

c. these species are treated as in steady-state if their (instantaneous) lifetimes are shorter than Δt (150s), and treated as time-dependent if their lifetimes are longer. Photo-reactive Br_y were initialized as calculated by the steady-state model. ClO, Cl_2O_2, OClO, HOCl, and $ClNO_3$ were initialized to be zero.

4.4 Results

4.4.1 Overview

CONTRAST data are available at http://data.eol.ucar.edu/master_list/?project=CONTRAST. All analyses are based on 1-min averaged data, and all times are in UTC (Guam local time is UTC+10 h). Flight paths for RFs 09 through 17 are shown in Figure 4.2. RF 17 was the returning transit fight and was out of the tropical West Pacific Ocean. Here RF 09 to RF16 were discussed.

From RF 09 to RF16, the GV covered a wide area above the tropical West Pacific Ocean, with an altitude range up to ~15.3 km. Sampling was mostly performed in the TTL (~32 h), with most of the remaining time in the TFT (~ 19 h). Observed BrO and HOBr+Br_2 in these flights are plotted against altitude in Figure 4.3. Most of the time BrO and HOBr+Br_2 were below the detection limit of the CIMS. However, significant levels of BrO and/or HOBr+Br_2, defined as consistently above the LOD, were observed episodically. They are highlighted in Figure 4.3 according to their locations (See section 4.4 for details). The means and medians of BrO and HOBr+Br_2 based on 2-km altitude intervals are superimposed in Figure 4.3. The median values are probably more representative of BrO and HOBr+Br_2 compared to mean values since episodic events can bias the means. However, both mean and median values are compatible with zero within the uncertainties at all levels.

Research flights targeted both sunlit and dark conditions. The diurnal patterns of BrO and HOBr+Br_2 were examined by plotting them against SZA (Figure 4.4). First, all data points were plotted against SZA (Figure 4.4a, b), then plotted data points against SZA

at three different altitude levels (<6km, 6 to 12km, >= 12km) (Figure 4.4, c to h). Similarly, averages and medians based on intervals of 10° of SZA were superposed in all panels of Figure 4.4. For the whole data set neither averages nor medians displayed significant departure from zero within uncertainties; and in general, the same conclusion holds for different altitude levels, especially in the TTL (alt >12km) where the sample size is relatively large. However, episodic significant levels can bias means and medians in lower altitudes (<6 km, and 6 to 12 km), due to smaller sample size in these altitude and SZA intervals.

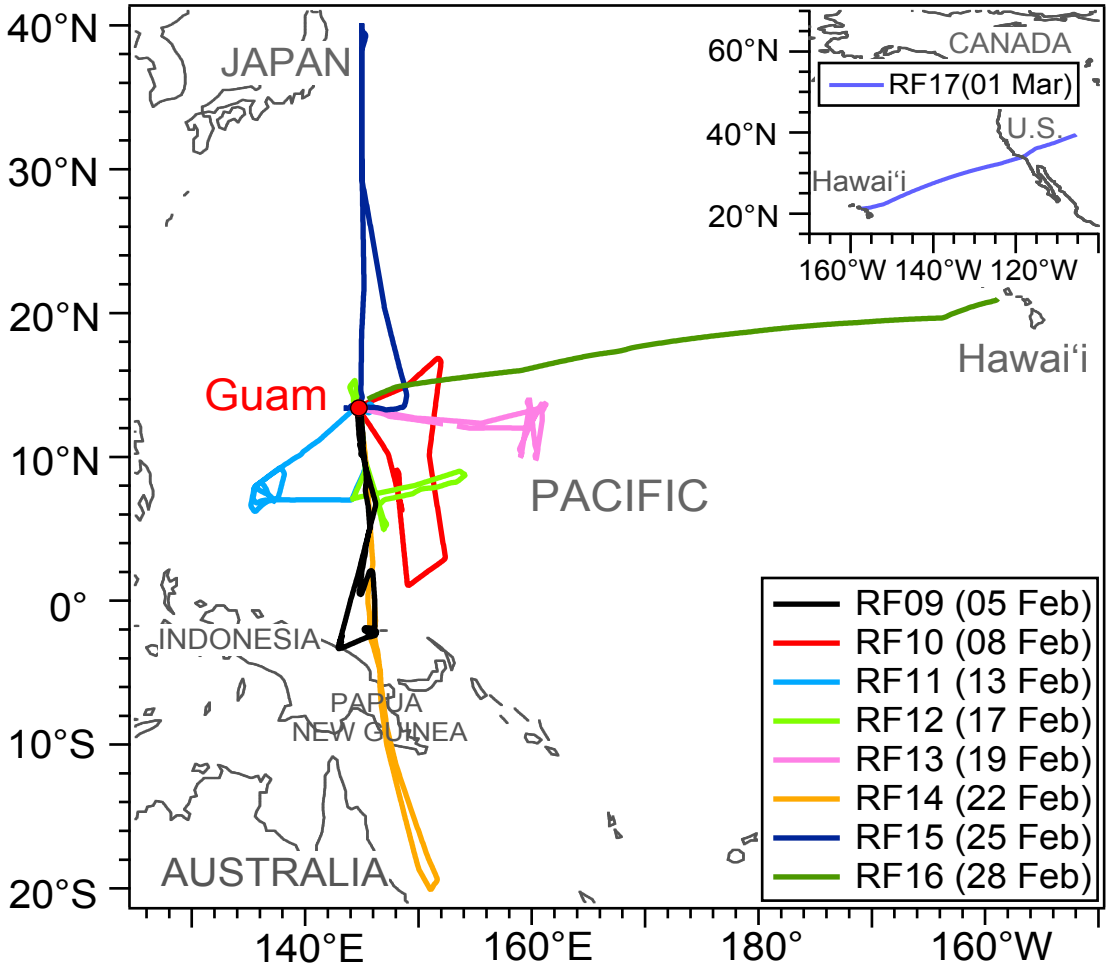

Figure 4.2. Flight paths during CONTRAST (RF09 to RF17).

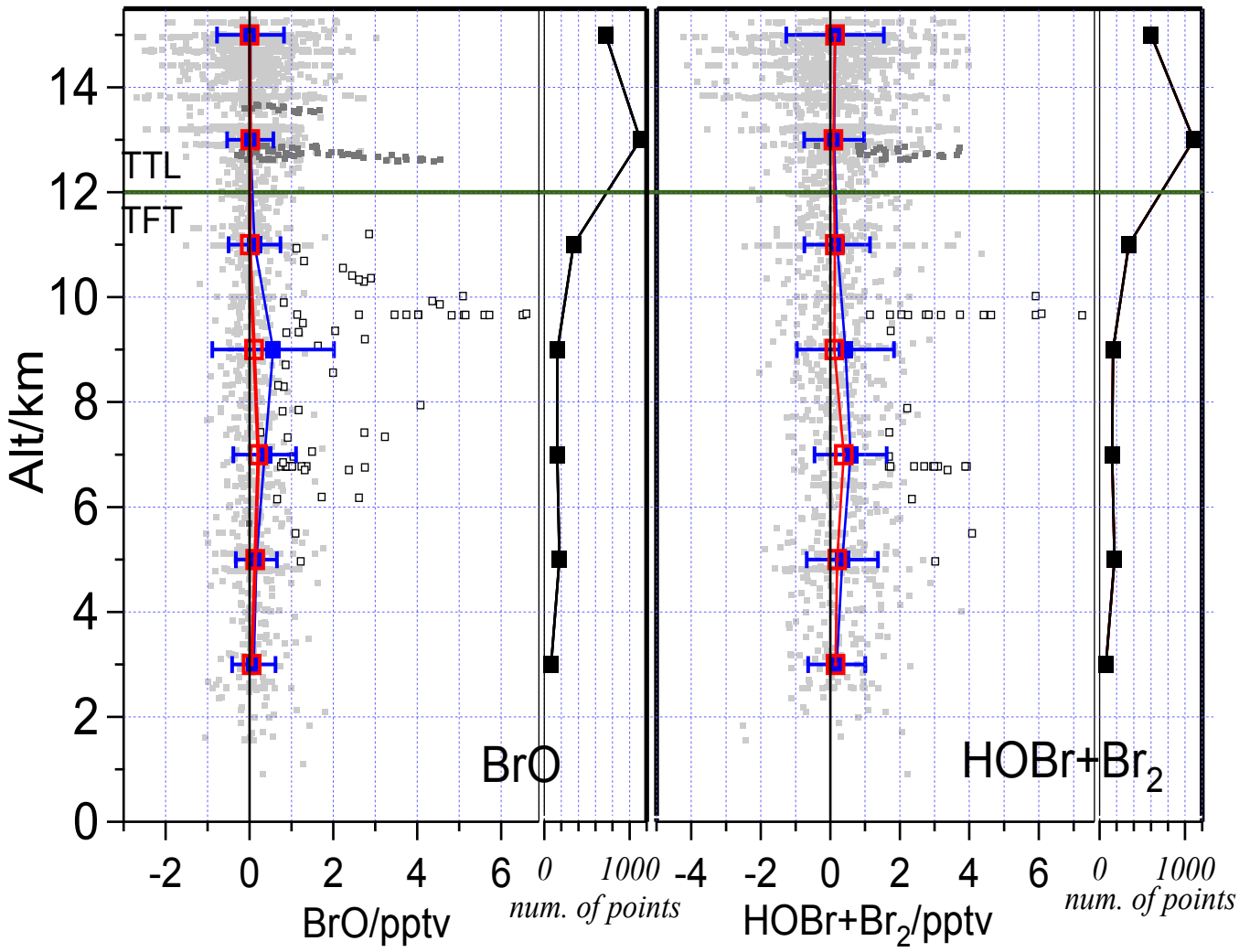

Figure 4.3. Vertical profiles of BrO (left panel) and HOBr+Br_2 (right panel). All 1-min averaged data points of BrO and HOBr+Br_2 are plotted. Significant BrO and HOBr+Br_2 levels are highlighted according to their locations: black open squares for the troposphere, and blacked filled squares for the TTL-LMS transition region and LMS (see section 4.4). The 2-km means with standard deviations (blue filled squares) and medians (red open squares) of all data points in the TTL and the TFT are superposed. Significant BrO and HOBr+Br_2 of LMS origin are excluded when means and medians were calculated. The numbers of data points falling into each 2-km bin are plotted on the side. Note that the medians are more representative than the means.

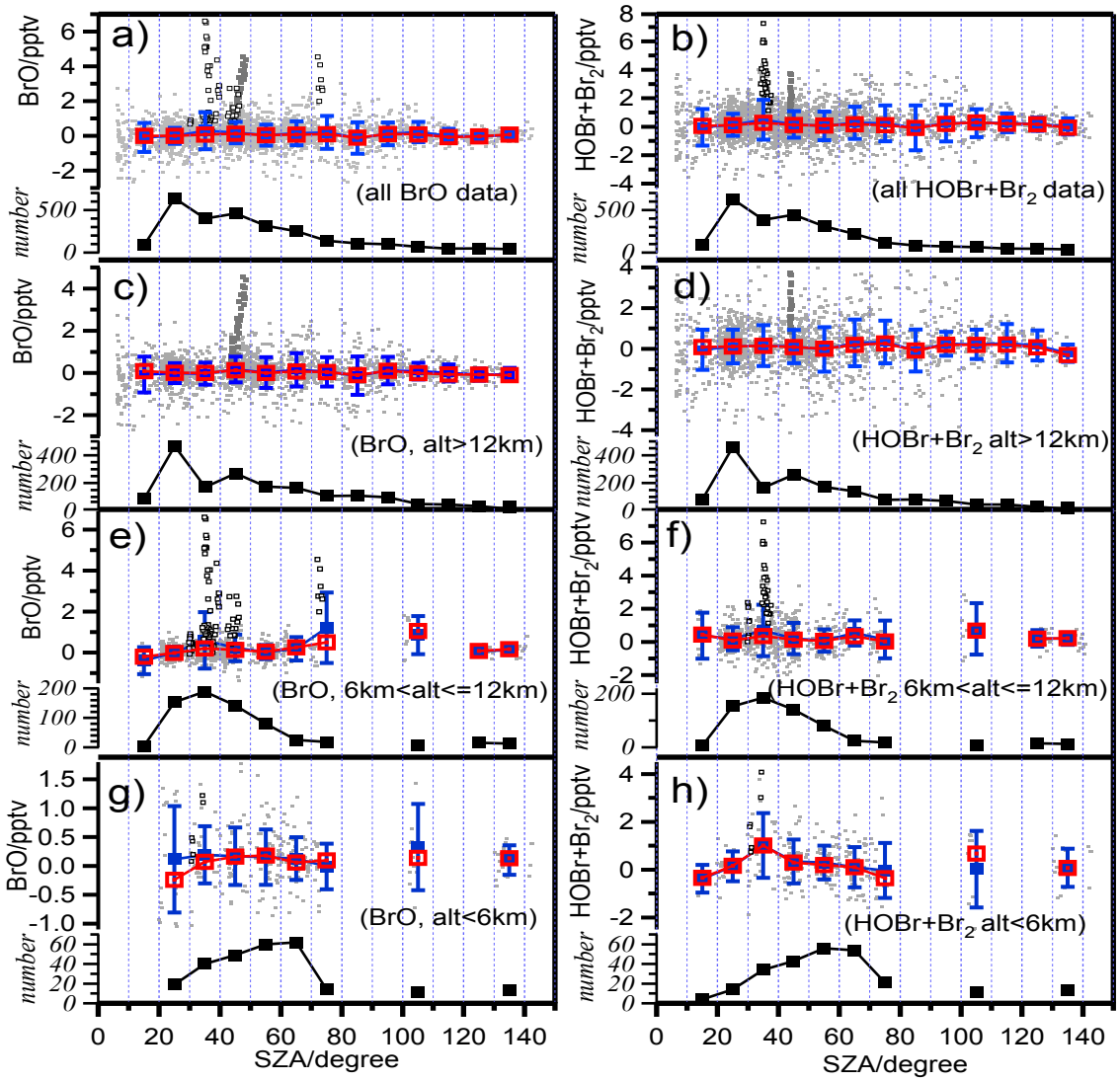

Figure 4.4. Diurnal profiles of BrO and HOBr+Br_2 plotted against SZA. In all panels, similar to Figure 4.3, all 1-min averaged data points are plotted, and significant BrO and HOBr+Br_2 are highlighted according to their locations, black open squares for troposphere, and black filled squares for the TTL-LMS transition region and LMS (see section 4.4). The 10° SZA-binned means with standard deviation (blue filled squares), and medians (red open squares) are superposed. The numbers of data points falling into each 2-km bin are plotted at the bottom of each panel. Note that scales may be different in different panels.

4.4.2 Fresh convective outflows and a stagnant anticyclone

Convective lifting is thought to be crucial for PGI, as it carries air from lower altitudes to the upper TFT and TTL, redistributing Br-containing species in the troposphere. In addition, an aged plume can allow Br_y to be produced from the decomposition of CBr_y^{VSL} precursors. Here, two fresh convective outflows and an aged anticyclone in the TTL are examined for enhanced Br_y in these air masses. The convective outflows and the aged anticyclone were identified and located prior to each RF with dynamic models, and confirmed by *in situ* measured trace gases in-flight.

In RF11 (13 Feb) between 12 and 14 km a fresh convective outflow originating from a clean MBL was targeted (Figure 4.5). The convective outflow was clearly characterized by high cloud particle concentrations (average 11.8 L^{-1}) and high water-ice content (average 1.3×10^{-3} $g\cdot m^{-3}$) Low O_3 (27.3±2.2 ppbv, average±1σ, *sic passim*) as well as background levels of CO (95.5±6.8 ppbv) and HCN (144±18 pptv) were consistent with an origin of the clean MBL. Inside the outflow, BrO was 0.03± 0.26 pptv (median 0.00 pptv), and HOBr+Br_2 was 0.003±0.42 (median 0.00 pptv). Significant BrO or HOBr+Br_2 inside this convective plume were observed. Significant levels of BrO and HOBr+Br_2 sampled during 00:30 to 01:00 UTC were not of convective origin (see section 4.3).

Similar results were found for the convective outflow sampled in RF12 (17 Feb) located between 12 and14 km to the south and southeast of Guam (Figure 4.5). This outflow can also be recognized by high water-ice content (average 1.8×10^{-3} $g\cdot m^{-3}$) and upward motion of air (vertical wind speed, W, up to ~ 1 $m\cdot s^{-1}$). The cloud particle

concentration is unavailable for this flight; but low O_3 (23.5±2.9 ppbv), background levels of CO (79.2±3.2 ppbv) and HCN (112±18 pptv) inside the outflow are consistent with an origin from the unpolluted MBL air. In the plume, BrO was −0.005±0.28 pptv (median 0.025 pptv), and HOBr+Br_2 was 0.19±0.55 pptv (median 0.105 pptv). In the adjacent air masses outside the plume (00:30 to 0116, 04:07 to 05:00 UTC), BrO was −0.04±0.32 pptv (median −0.02 pptv), and HOBr+Br_2 was 0.09±0.62 (median 0.07 pptv). No significant levels of BrO or HOBr+Br_2 were observed inside or outside the convective outflow.

A stagnant anticyclone centered at ~12°N, 160°E was probed in RF13 (19 Feb) before and after sunrise (Figure 4.6). The GV sampled inside the anticyclone between 19:00 and 22:20 UTC (local sunrise ~19:40 UTC). The GV stayed inside the anticyclone at ~13 km until ~21:40 UTC, then sampled a vertical profile from ~13 km down to ~2.5 km, then flew up to ~14 km. Although different levels of O_3 and CO were observed at different altitudes, no significant BrO or HOBr+Br_2 was observed at any altitude level, inside and outside the anticyclone, prior to and post sunrise.

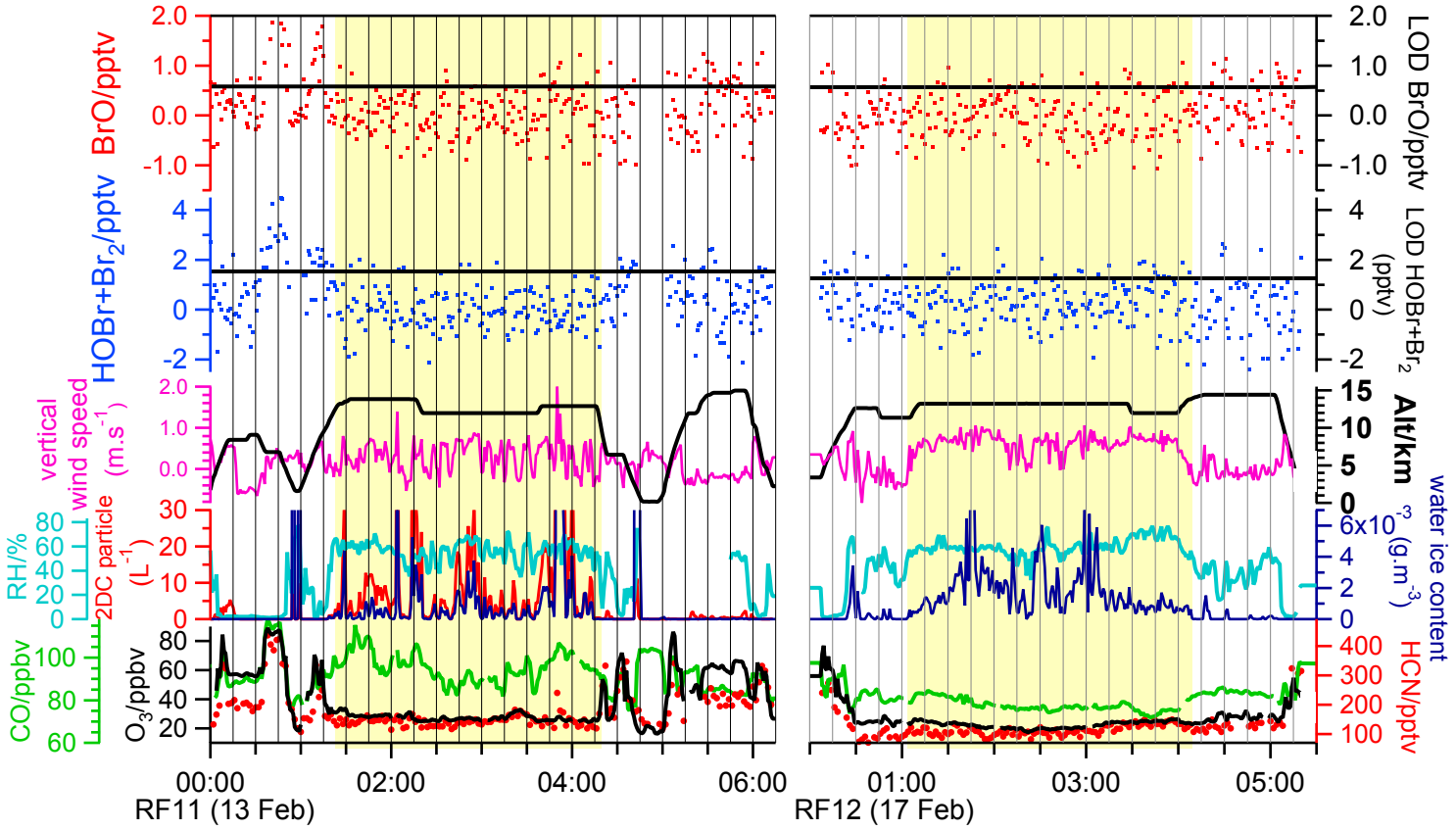

Figure 4.5. Time series of BrO, HOBr+Br2 and related species and parameters during RF 11 and RF 12. Convective outflow regions are shaded in light yellow.

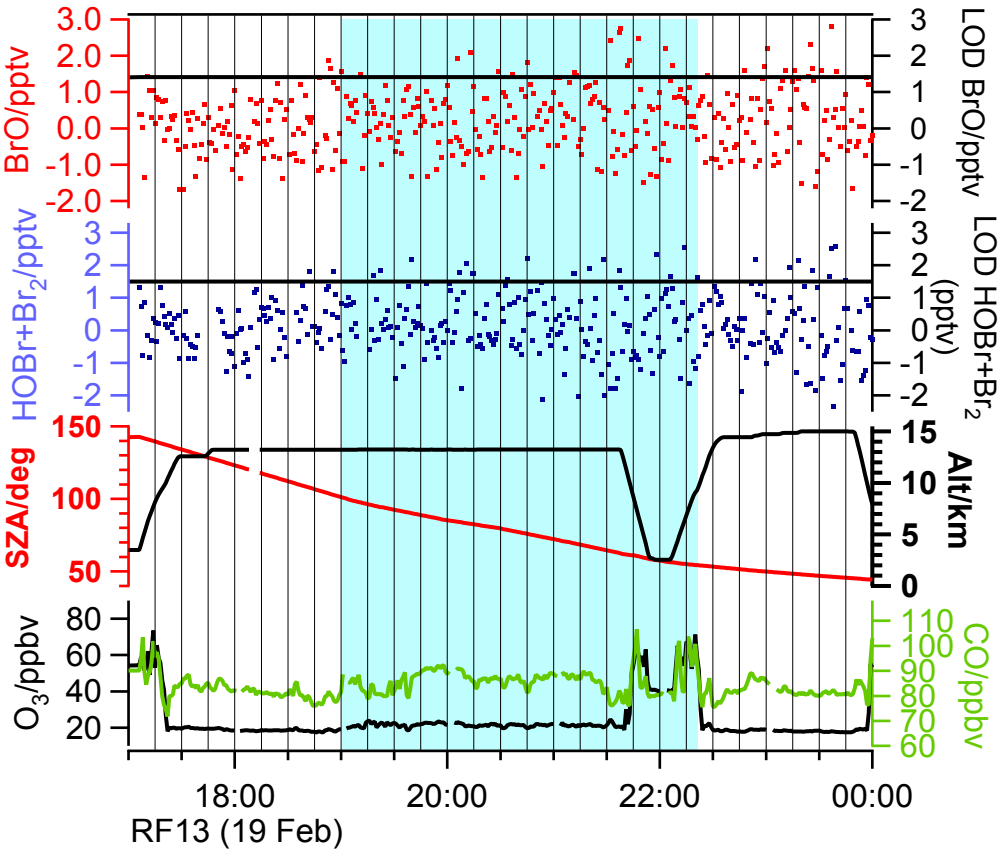

Figure 4.6. Time series of BrO, HOBr+Br_2 and related species and parameters during RF 13. The anticyclone region is shaded in light blue.

4.4.3 Enhanced BrO and/or HOBr+Br_2 in the tropical free troposphere

Plumes of significant BrO and/or HOBr+Br_2 were episodically observed in the TFT (Table 4.5). For convenience, these plumes are named with a prefix "Br" and a number (e.g., Br-1). Although the LODs varied with time, in all these plumes BrO and/or HOBr+Br_2 were clearly elevated. These plumes all featured high O_3, HCN and CH_3CN levels and low RH (Figure 4.7). O_3 in these plumes reached 60 to 90 ppbv, in contrast to the typical levels of 20 to 40 ppbv in the TFT. HCN in these plumes ranged from 200 pptv to 468 pptv, compared to background levels of 100 to 150 pptv. RH inside these plumes was generally <10%, except that in plume Br-2 RH varied from 8% to 75% and was probably influenced by mixing processes. In addition, in five out of the six plumes CO was clearly enhanced from the background levels. Finally, CH_3CN was moderately enhanced in all these plumes. Both HCN and CH_3CN are specific tracers of biomass burning emissions [e.g., *Holzinger et al.*, 1999]. All of these plumes are characteristic of the high-ozone, low-water (HOLW) structures that *Anderson et al.* [2016a] linked to biomass burning. Particularly, plume Br-4 was an interesting case known as the "CO River", where biomass burning-influenced air was trapped along the subtropical jet [*Pan et al.*, 2016].

The steady-state model was applied to check if observed BrO and HOBr+Br_2 levels in these plumes were self-consistent. HOBr+Br_2 was calculated with constraints of observed BrO and other measurements. In three out of the six plumes data are sufficient for model calculation of HOBr+Br_2. In all three plumes the calculated HOBr+Br_2 is consistent with the measured values (Figure 4.7).

Significant BrO and HOBr in biomass burning plumes have been reported [*Pommier et al.,* 2012]. However, to sustain these amounts of BrO and/or HOBr+Br_2, a strong source of Br_y must be present [*Pommier et al*., 2012]. Measured $CHBr_3$ and CH_2Br_2 appeared to be slightly lower inside these plumes compared to adjacent air masses. The degradation of $CHBr_3$ and CH_2Br_2 could be a source of Br_y. However, as the original plume concentrations are unknown this mechanism cannot be evaluated. However, bromocarbons are expected to be elevated in biomass plumes [e.g., *Simpson et al.,* 2011].

Table 4.5. Significant BrO and HOBr+Br_2 levels observed in the TFT.

plume	RF	highest BrO (LOD)/pptv[a]	highest HOBr+Br_2 (LOD)/pptv[a]
Br-1	RF 09	2.7 (1.3)	<LOD (3.5)
Br-2	RF 09	4.4 (1.3)	<LOD (3.5)
Br-3	RF 09	4.5 (1.3)	<LOD (3.5)
Br-4	RF 10	6.6 (1.1)	7.3 (3.0)
Br-5	RF 11	1.5 (0.6)	3.9 (1.5)
Br-6	RF 11	1.0 (0.6)	2.3 (1.5)

a. values quoted are flight-averaged LOD.

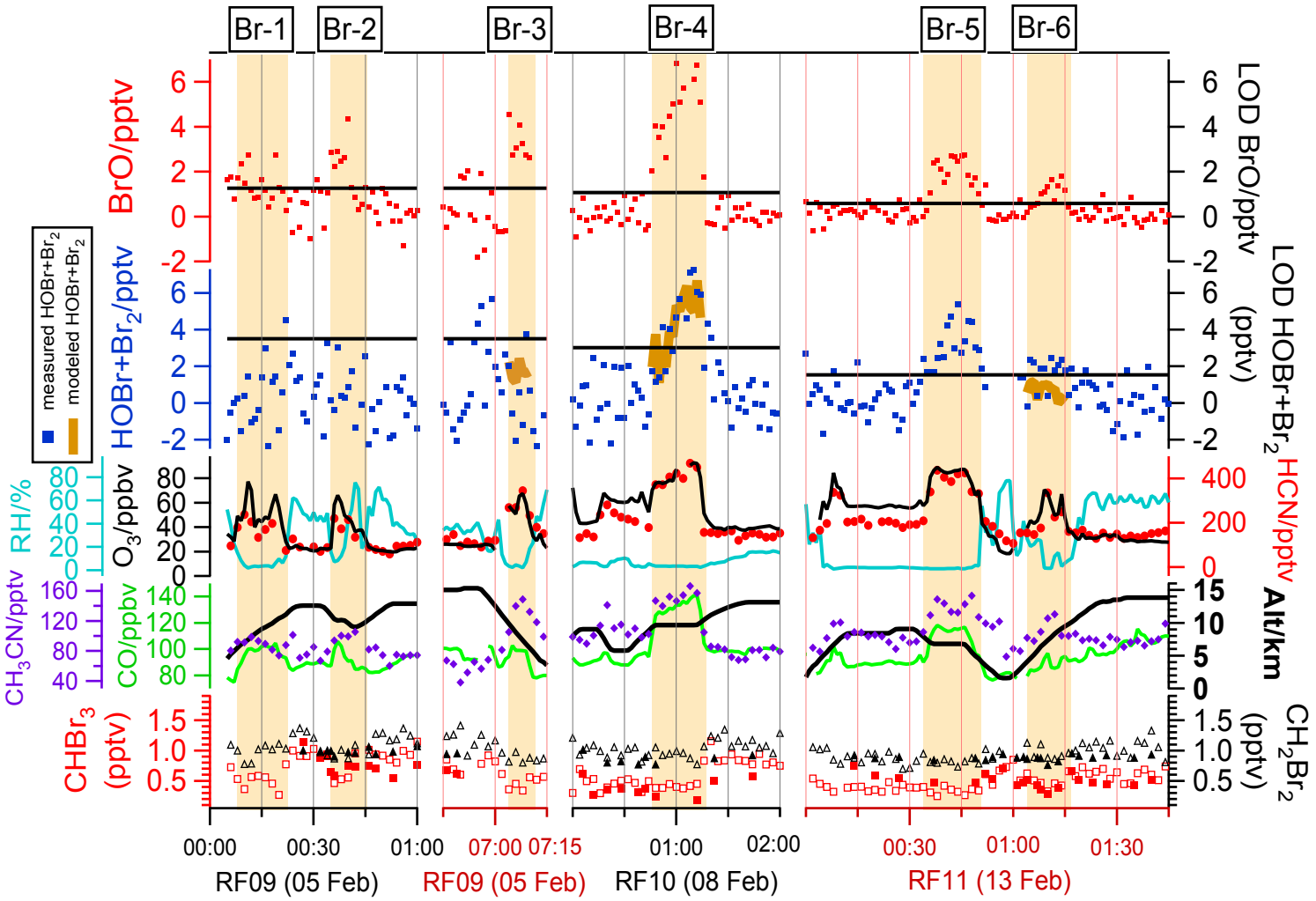

Figure 4.7. Episodic significant BrO, HOBr+Br$_2$ in the TFT and related species and parameters. Plumes of significant BrO and/or HOBr+Br$_2$ are shaded in light orange. In three of these plumes we had sufficient data to calculate HOBr+Br$_2$ with the steady-state model, using measured BrO as a constraint. Measured HOBr+Br$_2$ (blue squares) and calculated HOBr+Br$_2$ (brown solid line) are compared. CHBr$_3$ and CH$_2$Br$_2$ measured by AWAS (solid markers) and TOGA (open markers) are also plotted.

4.4.4 A survey from the TTL to the extratropical LMS

During RF15 (25 Feb) the GV sampled both the TTL and the extratropical LMS at altitudes of 12 to 14 km, with the northernmost point at ~40°N (see Figure 4.3 for flight path). Time series of BrO, HOBr+Br_2 and other species/parameters are plotted in Figure 4.8, together with the potential vorticity (PV). Here the PV was calculated from 6 hourly 1° latitude ×1° longitude, 26 vertical level NCEP GFS-FNL analyses and then co-located with GV observations by interpolating in space (latitude, longitude, pressure) and time along the GV track (http://www.emc.ncep.noaa.gov/gmb/para/parabout.html). A previous application example of the derived PV can be found in *Pan et al.* [2007]. Both chemical tracers and PV clearly displayed the sharp change in the transition from the TTL to the extratropical LMS (Figure 4.8). In the TTL, O_3, CO, and CFC-11 (CCl_3F) were roughly 20 ppbv, 100 ppbv and 235 pptv, respectively, and PV was consistently < 1.7 PVU (1 PVU = 10^{-6} $K \cdot m^2 \cdot kg^{-1} \cdot s^{-1}$). At latitudes greater than ~25°N, O_3 increased and CO decreased. Meanwhile H_2O vapor dropped to < 10 ppmv, and PV rapidly increased from roughly 1.4 PVU to roughly 7.5 PVU. However, CFC-11 still remained at ~235 pptv until ~ 33°N. At ~ 33°N CFC-11 sharply dropped to ~215 pptv while O_3 sharply increased from ~100 ppbv up to ~800 ppbv. H_2O vapor decreased to 3 to 4 ppmv. PV remained at ~8 PVU. Although O_3 started to increase and CO started to decrease at ~25°N, $\Delta CO/\Delta O_3$ was –0.395 between ~25°N to ~ 33°N, and –0.0239 between ~33°N to ~ 40°N. At latitudes greater than ~33 °N, the sharp increase of O_3, the decrease of CFC-11, plus the high PV values undoubtedly denoted the extratropical LMS. The region between ~25°N to ~33°N should be regarded as a transition region between the TTL and extratropical LMS. In this transition region CFC-11 level was the same as in the TTL (~235 pptv), but PV, and the CO – O_3 correlation

[e.g. *Pan et al.*, 2004] still distinguished it from the LMS and TTL (Figure 4.9). The discontinuity in CO – O_3 relationship occurred at latitude ~ 33° N, CO ~ 56 ppbv, O_3 ~138 ppbv, and PV ~ 6 to 8 PVU. It clearly marked the point of entering the stratosphere. The 6 to 8 PVU PV value near the discontinuity point is very consistent with the climatological PV value that represents the dynamical tropopause at the 370-380 K isentropic level during the Northern Hemisphere winter [*Kunz et al.*, 2011].

Different levels of BrO and HOBr+Br_2 were observed in the TTL, the TTL extratropical LMS transition region and the extratropical LMS. In the TTL, 0.11±0.35 pptv of BrO (median 0.10 pptv), and 0.17±0.64 pptv of HOBr+Br_2 (median 0.10 pptv) were observed. In the transition region, 0.48 ±0.58 pptv of BrO (median 0.34 pptv), and 0.63±1.14 pptv of HOBr+Br_2 (median 0.58 pptv) were observed. In the LMS, BrO levels were clearly above zero, up to roughly 4.5 pptv at 480 ppbv of O_3. This survey indicates that BrO and HOBr+Br_2 were near zero in the TTL, and started to increase in the TTL-LMS transition region.

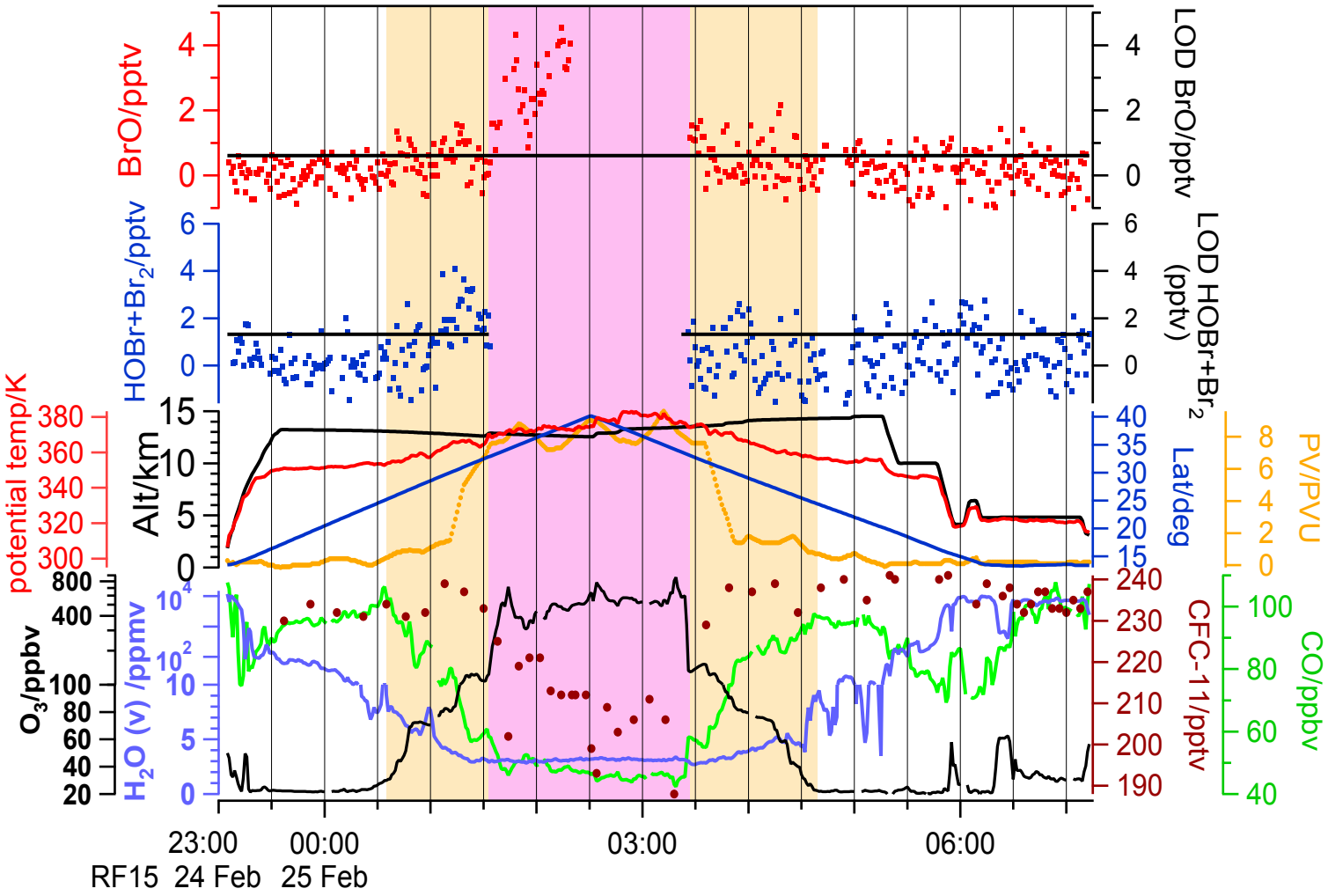

Figure 4.8. Time series of BrO, HOBr+Br_2 and related species /parameters during RF 15. The LMS leg is highlighted in pink, and the TTL-LMS transition region is highlighted in light gold. Note: because of interferences, BrO data are unavailable when O_3 > ~480 ppbv, and HOBr+Br_2 data are unavailable when O_3 > ~125 ppbv.

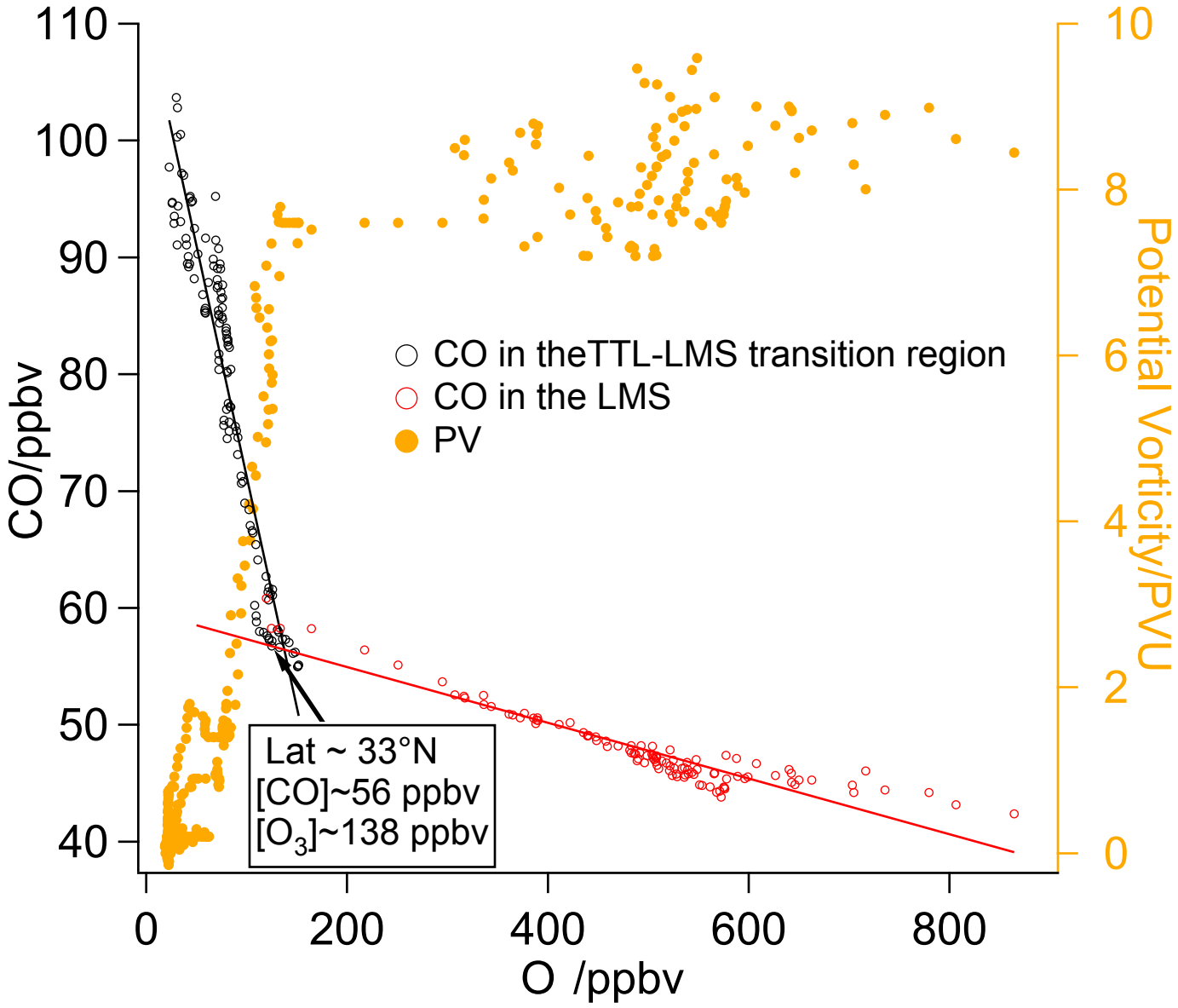

Figure 4.9. Correlation between CO and O_3 in the TTL-LMS transition region (open black circles) and the LMS (open red circles). In the TTL-LMS transition region, [CO]/ppbv = 110.8−0.395×[O_3]/ppbv (r = −0.952). In the LMS, [CO]/ppbv = 59.7−0.0239×[O_3]/ppbv (r = −0.933). The CO - O_3 correlations were different in the TTL-LMS transition region and the LMS. The potential vorticity (PV) (solid yellow circles) rapidly increased in the TTL-LMS transition region but was relatively stable in the LMS.

4.5 Dicussions

4.5.1 Br_y partitioning in the TFT and TTL

The partitioning of Br_y in the TFT and TTL was estimated in two steps. First, photo-reactive Br_y was estimated with the steady-state model. A constant level of 1 pptv of BrO was assumed for these calculations as this was the approximate LOD for BrO for most of the campaign. For the steady-state model, since the steady-state assumption does not hold if *j* values are low, only daytime chemistry were considered, and those data points with SZA > 80° were filtered out. After that, HBr was estimated with the time-dependent model. The time-dependent model was run until stable diurnal profiles of Br_y were reached, and thus the estimated HBr must be regarded as a regional average. Daytime averages of HBr were calculated for comparisons with other Br species. the daytime vertical profiles of ([HOBr]+[Br_2])/[BrO], [$BrNO_3$]/]BrO], [Br]/[BrO], ([Br_y]−[HBr])/[BrO] and [HBr]/[Br_y] were estimated as in Figure 4.10. Given both gas-phase and heterogeneous sources of BrCl (R8c, R22, R23), BrCl was still found to be negligible (on the order of 10^{-3} pptv) in the daytime due to its rapid photo dissociation (j(BrCl) ~10^{-2} s^{-1}).

For the daytime photo-reactive Br_y budget HOBr was the dominant species from the bottom of the TFT to ~8 km, where ([HOBr]+[Br_2])/[BrO] ranged from 1 to 4 (Figure 4.10). Yet no significant HOBr+Br_2 was observed, indicating very low BrO in these altitude levels. The ratio of [Br]/[BrO] increased with altitude and is significantly greater than 1 in the TTL, making Br atom the dominant daytime photo-reactive Br_y component from ~11 km to the highest altitude (~ 15 km). HBr was the major component of Br_y throughout the TFT, accounting for ~70% of Br_y (Figure 4.10). The dominance of HBr is

driven by (1) low O_3, which favors Br atom rather than BrO, and (2) sufficient CH_2O, which reacts with Br atoms to form HBr. BrO was not the dominant Br_y species nor even the dominant photo-reactive Br_y species. In the TTL at ~14 km HBr/Br_y dropped to 60%, mostly due to the heterogeneous cycling of HBr (R21, R22). However, as the ice particle distribution is highly variable in the TTL, the calculation of HBr/Br_y there is uncertain, although it is difficult to estimate the uncertainty based on this dataset and model scheme. Consequently, it is possible that HBr/Br_y was less than what is estimated here and Br atoms dominate the bromine distribution in the TTL.

These findings do not support significant "excess" BrO in the TFT [e.g., *Wang et al*., 2015], in good agreement with the observation by *Dorf et al*. [2008], and modeling studies by *von Glasow et al.* [2004], *Yang et al*. [2005], *Parrella et al.* [2012], *Liang et al.* [2014], and *Fernandez et al.* [2014]. However, it should be pointed out that low and nearly insignificant levels of BrO and $HOBr+Br_2$ do not necessitate insignificant Br_y. Indeed, analysis above suggests that HBr is the most abundant Br_y species in the TFT, either HBr or Br is the most abundant Br_y species in the TTL up to ~ 15 km. However, HBr and Br atom levels are not constrained by observations and measurement of these species is needed in future studies.

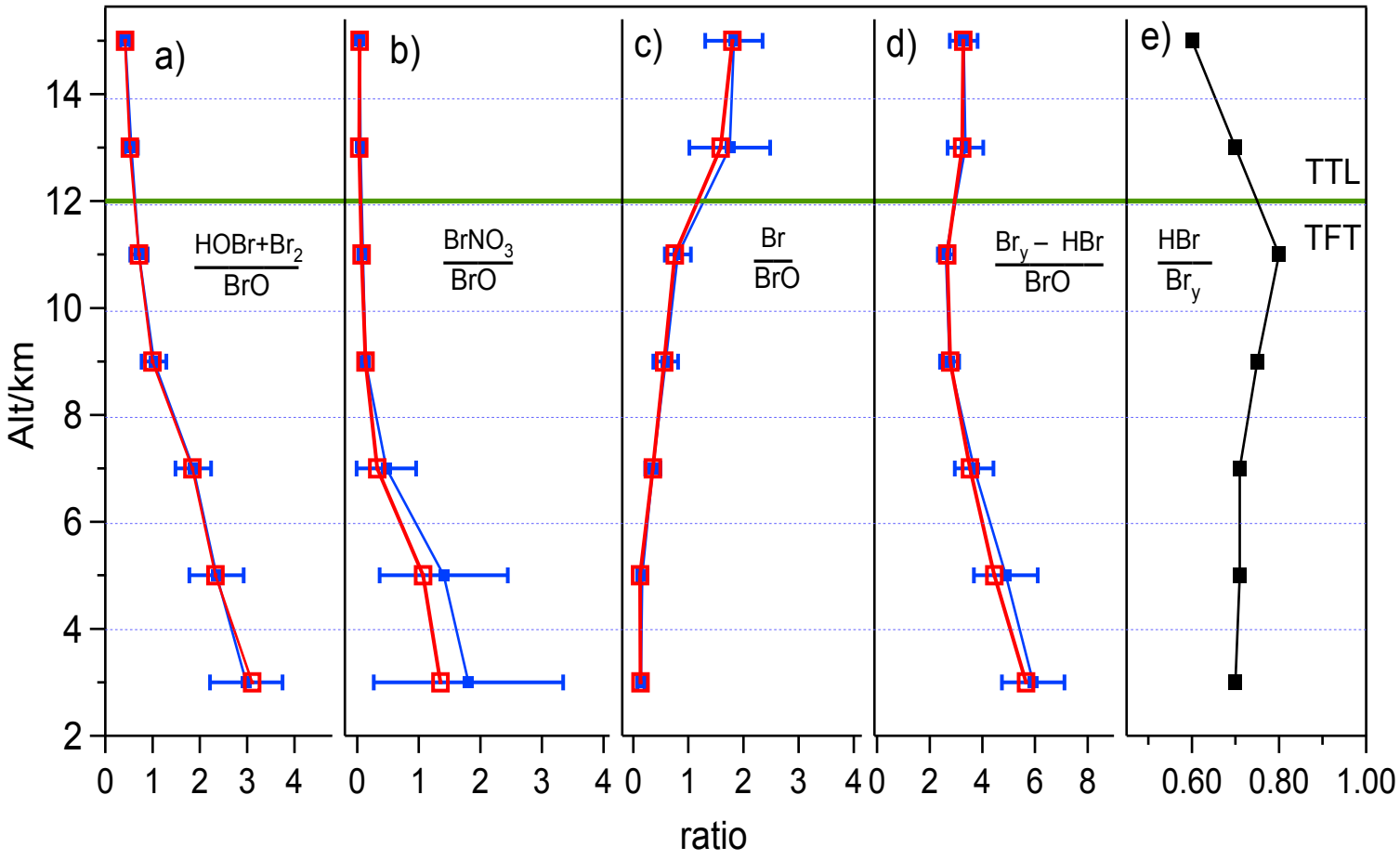

Figure 4.10. (a) to (d), Vertical profiles of ([HOBr]+[Br_2])/[BrO], [$BrNO_3$]/[BrO], [Br]/[BrO], and ([Br_y]−[HBr])/[BrO] ratios while SZA<80°, estimated by the steady-state model. 2-km means with standard deviations are shown in blue, and 2-km medians are shown in red. (e) Daytime vertical profile of [HBr]/[Br_y] ratio estimated by the time-dependent model.

4.5.2 Estimation of PGI of bromine species

PGI from bromine species was estimated based on RF15 data. The Br_y profiles from the TTL-LMS transition region to the LMS were inferred with similar processes as in section 5.1. Since CH_2O was well constrained in the TTL-LMS transition region but not in the LMS, the models were constrained with measured CH_2O in the TTL-LMS transition region but assumed levels of CH_2O (1 pptv, 5pptv, and 20 pptv) in the LMS leg. However, HBr was found much less sensitive to CH_2O in the LMS than in the TTL/TFT, since partitioning to BrO is favoured at high O_3, which supresses the reaction of Br with CH_2O. The inferred Br_y profiles were plotted against O_3 in Figure 4.11. The inferred Br_y was about 1 to 2 pptv in the TTL-LMS transition region, then slowly increased with increasing O_3. The PGI of bromine species was estimated to be roughly 2 pptv, based on the Br_y level inferred at the boundary between the TTL-LMS transition region and the LMS. This estimate of Br_y is in the range of values recently reported in *Carpenter et al*. [2014] and *Navarro et al*. [2015]. Complete assessments of both PGI and SGI of bromine species for CONTRAST will be presented in an upcoming paper [*Wales et al.*, in preparation].

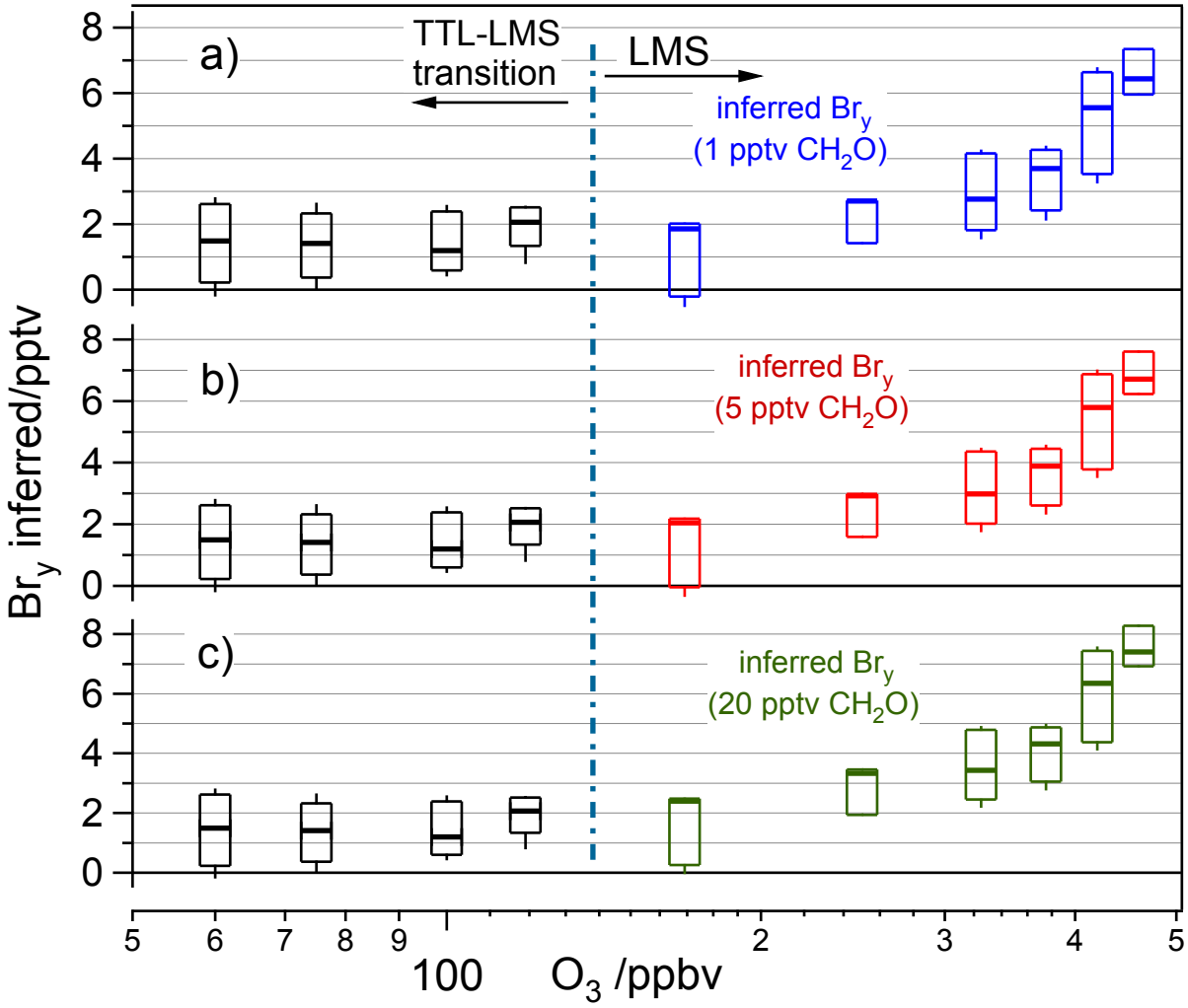

Figure 4.11. Box and whisker plot of inferred Br_y from the TTL-LMS transition region to the LMS. The bottom and top of the boxes are the first and third quartiles, and the bands inside the box are the medians. The ends of whiskers represent the 10th and 90th percentiles. Br_y in the TTL-LMS transition region was inferred based on measured CH_2O, and are plotted in all panels. Br_y in LMS was inferred assuming 1 pptv, 5 pptv and 20 pptv CH_2O, plotted in panels (a), (b), and (c), respectively. The boundary between the TTL-LMS transition region and the LMS is marked.

4.6 Conclusions

Observations of BrO and HOBr+Br_2 were performed using CIMS during CONTRAST over the tropical West Pacific. Observations showed that the levels of BrO and HOBr+Br_2 were effectively below the LODs in the TFT and TTL from ~1 km up to ~15.3 km. No significant levels of BrO and HOBr+Br_2 were observed inside multiple fresh deep convective plumes and an aged anticyclone in the TTL. The episodic significant BrO and HOBr+Br_2 in the troposphere were found to be associated with elevated O_3, CO, HCN, CH_3CN, and low RH. It is postulated here that these significant Br_y originated from biomass burning. However, the relevant mechanism of the release of Br_y remains unclear. In RF15, profiles of BrO and HOBr+Br_2 from the TTL to the extratropical LMS were obtained. In this flight, significant levels of BrO were observed in the extratropical LMS, slightly elevated BrO and HOBr+Br_2 were observed in the TTL-LMS transition region, but no significant amount of BrO and HOBr+Br_2 were found in the TTL. This is consistent with the findings during other flights that BrO and HOBr+Br_2 were near zero in the TTL.

Observations of BrO gave no indication for "excess" BrO in the TFT. Furthermore, analysis of Br_y partitioning shows that during the day HOBr and Br were the dominant photo-reactive Br_y species at altitude levels of 1 to 8 km, and 11 km to 15 km, respectively. The low levels of HOBr+Br_2 observed from the bottom of the TFT to ~8 km were consistent with even lower BrO. Analysis also suggests that HBr is the most abundant Bry species in the TFT, and either HBr or the Br atom is the most abundant Bry species in the TTL below 15 km. Future measurements of HBr and Br atoms are strongly suggested. The Br_y profile was inferred from the TTL to the extratropical LMS based on RF15, and estimated bromine PGI to be roughly 2 pptv based on the inferred Br_y profiles.

4.7 Acknowledgements

This work was supported by the NSF grant #1262033. I would like to thank CONTRAST team and the GV crew. CONTRAST data are available online at http://data.eol.ucar.edu/master_list/?project=CONTRAST. CONTRAST data are managed by the Earth Observing Laboratory of the National Center for Atmospheric Research (NCAR/EOL). NCAR is sponsored by the National Science Foundation.

CHAPTER 5. CONCLUSIONS

In this thesis chemical ionization mass spectrometry (CIMS) was used to investigate HO_2NO_2 and Br_y. This work demonstrates the capability of CIMS in measuring a series of trace gases, and advances our understanding of HO_x-NO_x-HO_2NO_2 chemistry and Br_y chemistry.

This thesis presents CIMS measurements of HO_2NO_2 in metropolitan Atlanta, and the inference of HO_2 concentrations based on HO_2NO_2 measurements. This inference method was evaluated by analyzing the suppression of HO_2 at high NO, the correlation of HO_2 with O_3 and NO_3 at night, and comparing inferred HO_2 with model calculations. The analyses show the feasibility of inferring HO_2 via HO_2NO_2 measurement in warm regions.

This thesis reports CIMS measurements of BrO and HOBr+Br_2 over the tropical West Pacific Ocean within the altitude range of 1 to 15 km, during the CONvective TRansport of Active Species in the Tropics (CONTRAST) campaign. Isolated episodes of elevated BrO (up to 6.6 pptv) and/or HOBr+Br_2 (up to 7.3 pptv) were observed in the tropical free troposphere and were associated with biomass burning. However, most of the time BrO or HOBr+Br_2 in the TFT and the TTL were found below the LOD of the CIMS. The 1-min average LOD for BrO ranged between 0.6 and 1.6 pptv, and for HOBr+Br_2 ranged between 1.3 to 3.5 pptv. During one flight, BrO observations from the TTL to the extratropical lowermost stratosphere (LMS) were used to infer a profile of inorganic bromine (Br_y). Based on this profile, the product gas injection (PGI) of bromine species into the stratosphere to was estimated be roughly 2 pptv. Analysis of Br_y partitioning

further indicates that BrO levels are likely very low in the TFT environment and that future studies should target the measurement of HBr or Br atoms.

APPENDIX A. THE ZERO DIMENSIONAL STEADY-STATE AND TIME-DEPENDENT BOX MODELS

Both 0−D models include 150 reactions, of which 101 are bimolecular reactions (Table A 1), 13 are termolecular reactions (Table A 2), 22 are photo−dissociation reactions (Table A 4), and 10 are heterogeneous reactions (Table A 5). The thermal dissociation rates for HO_2NO_2, N_2O_5, PAN, and Cl_2O_2 were obtained from their formation rates (Table A 1) and their equilibrium constants (Table A 3).

Heterogeneous chemistry is considered for the evaluation of the Br_y partitioning (Chapter 4). For X + Y → P, where X is in gas−phase, Y is adsorbed on particle surfaces, the rate constant is parameterized as the first-order loss rate of X in gas phase (Eq. A1) [*Schwartz*, 1986; *Jacob*, 2000].

$$k_{\text{het}} \equiv -\frac{1}{[\text{X}]}\frac{d[\text{X}]}{dt} = \left(\frac{r}{\mathcal{D}_g} + \frac{4}{\bar{v}\,\gamma}\right)^{-1} A \qquad \text{(A.1)}$$

where:

k_{het} first-order heterogeneous reaction rate, s^{-1};

r particle radius;

$\mathcal{D}_g$ gas−phase diffusivity, assumed to be 0.2 $cm^2 \cdot s^{-1}$;

$\bar{v}$ mean molecular speed, $cm \cdot s^{-1}$; $\bar{v} = \sqrt{\frac{8k_B T}{\pi m}}$ (k_B, Boltzmann's constant; m, mass of the molecule);

γ reactive uptake coefficient, unitless;

A surface area density of particles, $cm^2 \cdot cm^{-3}$;

k_{het} was integrated over the particle distribution. γ values are listed in Table A5.

For each study in this thesis, only a subset of these reactions was included, and other reactions were excluded by setting the rate constants to be zero.

Table A 1. Bimolecular reactions.

No.	Reactions	rate constant/$cm^3 \cdot s^{-1}$	Notes
B1	$O(^1D)+H_2O \rightarrow OH+OH$	$1.63e{-}10\times\exp(60/T)$	a
B2	$O(^1D)+CH_4(+O_2) \rightarrow OH+CH_3O_2$	$1.31e{-}10$	a
B3	$O(^1D)+N_2(+O_2) \rightarrow O_3+N_2$	$2.15e{-}11\times\exp(110/T)$	a
B4	$O(^1D)+O_2(+O_2) \rightarrow O_3+O_2$	$3.3e{-}11\times\exp(55/T)$	a
B5	$O_3+NO \rightarrow NO_2+O_2$	$3.0e{-}12\times\exp(-1500/T)$	a
B6	$O_3+NO_2 \rightarrow NO_3+O_2$	$1.2e{-}13\times\exp(-2450/T)$	a
B7	$NO_3+NO \rightarrow NO_2+NO_2$	$1.5e{-}11\times\exp(170/T)$	a
B8	$OH+O_3 \rightarrow HO_2+O_2$	$1.7e{-}12\times\exp(-940/T)$	a
B9	$OH+CH_4(+O_2) \rightarrow CH_3O_2+H_2O$	$2.45e{-}12\times\exp(-1775/T)$	a
B10	$OH+CH_3OH(+O_2) \rightarrow HO_2+CH_2O+H_2O$	$7.3e{-}12\times\exp(-620/T)$	a
B11	$OH+CH_2O(+O_2) \rightarrow CO+HO_2+H_2O$	$5.4e{-}12\times\exp(135/T)$	a
B12	$OH+C_2H_6(+O_2) \rightarrow C_2H_5O_2+H_2O$	$8.7e{-}12\times\exp(-1070/T)$	a
B13	$OH+CH_3CHO(+O_2) \rightarrow CH_3C(O)O_2+H_2O$	$4.63e{-}12\times\exp(350/T)$	a
B14	$OH+C_3H_8+(O_2) \rightarrow C_3H_7O_2+H_2O$	$8.7e{-}12\times\exp(-615/\mathrm{T})$	a
B15	$OH+CH_3C(O)CH_3(+O_2) \rightarrow CH_3C(O)CH_2O_2+H_2O$	$1.33e{-}13+3.82e{-}11\times\exp(-2000/T)$	a
B16	$OH+CH_3C(O)CH_2OH(+O_2) \rightarrow CH_3C(O)CHO+HO_2+H_2O$	$1.6e{-}12\times\exp(-305/T)$	b
B17	$OH+CH_3C(O)CHO(+O_2) \rightarrow CH_3C(O)O_2+CO+H_2O$	$1.9e{-}12\times\exp(575/T)$	b
B18	$OH+\mathrm{MACR} \rightarrow 0.5MOHO_2+0.5MCO_3$	$8e{-}12\times\exp(380/T)$	c
B19	$OH+\mathrm{MVK} \rightarrow MOHO_2$	$2.6e{-}12\times\exp(610/T)$	c
B20	$OH+\mathrm{Isoprene}(+O_2) \rightarrow Isop(OH)O_2$	$3.1e{-}11\times\exp(350/T)$	a
B21	$OH+\mathrm{Benzene}(+O_2) \rightarrow 0.43ArO_2+0.57HO_2+\mathrm{others}$	$2.3e{-}12\times\exp(-190/T)$	d
B22	$OH+\mathrm{Toluene}(+O_2) \rightarrow 0.43ArO_2+0.57HO_2+\mathrm{others}$	$1.8e{-}12\times\exp(340/T)$	d
B23	$NO_3+CH_2O(+O_2) \rightarrow HO_2+CO+HNO_3$	$5.5e{-}16$	b
B24	$NO_3+CH_3OH \rightarrow HO_2+CH_2O+HNO_3$	$9.4e{-}13\times\exp(-2650/T)$	b
B25	$NO_3+C_2H_4(+O_2) \rightarrow R(NO_3)O_2$	$3.3e{-}12\times\exp(-2880/T)$	b
B26	$NO_3+CH_3CHO(+O_2) \rightarrow CH_3C(O)O_2+HNO_3$	$1.4e{-}12\times\exp(-1860/T)$	b
B27	$NO_3+\mathrm{Isoprene}(+O_2) \rightarrow R(NO_3)O_2$	$2.95e{-}12\times\exp(-450/T)$	b
B28	$O_3+C_2H_4 \rightarrow CH_2O+0.16OH+0.16HO_2+\mathrm{others}$	$9.1e{-}15\times\exp(-2580/T)$	e
B29	$O_3+C_3H_6 \rightarrow CH_2O+CH_3CHO+0.3OH+0.08HO_2+\mathrm{others}$	$5.5e{-}15\times\exp(-1880/T)$	e

B30	O_3+Isoprene→0.06HO_2+0.68OH+others		1.03e−14×exp(−1995/*T*)	c
B31	O_3+MACR→0.275HO_2+0.215OH+others		2.6e−12×exp(610/*T*)	c
B32	O_3+MVK→0.06HO_2+0.08OH+others		8.5e−16×exp(−1520/*T*)	c
B33	OH+HO_2→H_2O+O_2		4.8e−11×exp(250/*T*)	a
B34	OH+H_2O_2→HO_2+H_2O		1.8e−12	a
B35	OH+CH_3OOH→0.7CH_3O_2+0.3CH_2O+0.3OH+H_2O		3.8e−12×exp(200/*T*)	a
B36	OH+HONO→NO_2+H_2O		1.8e−11×exp(−390/*T*)	a
B37	OH+HO_2NO_2→NO_2+H_2O+O_2		1.3e−12×exp(380/*T*)	a
B38	HO_2+O_3→OH+2O_2		1.0e−14×exp(−490/*T*)	a
B39	HO_2+HO_2→H_2O_2+O_2	F_w =(1+1.4e−21×[H_2O]×exp(2200/*T*)) k_{B39}=(3.0e−13×exp(460/*T*)+ 2.1e−33×[M]×exp(920/*T*))×F_w		a
B40	HO_2+CH_3O_2→CH_3OOH+O_2		4.1e−13×exp(750/*T*)	a
B41	HO_2+$C_2H_5O_2$→C_2H_5OOH+O_2		7.5e−13×exp(700/*T*)	b
B42	HO_2+$C_2H_4(OH)O_2$→$C_2H_4(OH)OOH$+O_2		assumed = k_{B41}	
B43a	HO_2+$CH_3C(O)O_2$→$CH_3C(O)OOH$+O_2		4.3e−13×exp(1040/*T*)/(1+37×exp(−660/*T*))	a
B43b	HO_2+$CH_3C(O)O_2$(+O_2)→CH_3O_2+CO_2+OH+O_2		k_{B43b}=k_{B43a}×37×exp(−660/*T*)	a
B44	HO_2+$CH_3C(O)CH_2O_2$→$CH_3C(O)CH_2OOH$+O_2		8.6e−13×exp(700/*T*)	a
B45	HO_2+Isop(OH)O_2→Isop(OH)OOH+O_2		7.5e−13×exp(700/*T*)	c
B46	HO_2+$MOHO_2$→ 0.3CH_3CO_3+0.3CH_2OHCHO		7.5e−13×exp(700/*T*)	c
B47	HO_2+MCO_3→$MOHO_2$		4.5e−13×exp(1040/*T*)	c
B48	HO_2+$R(NO_3)O_2$→products		3.4e−13×exp(800/*T*)	f
B49a	CH_3O_2+CH_3O_2→CH_3OH+CH_2O		9.5e−14×exp(390/*T*)/(1+26.2×exp(−1100/*T*))	a
B49b	CH_3O_2+CH_3O_2(+2O_2)→2CH_2O+2HO_2+O_2		k_{B49b}=k_{B49a}×26.2×exp(−1100/*T*)	a
B50a	CH_3O_2+$C_2H_5O_2$(+2O_2)→ CH_2O+CH_3CHO+2HO_2+O_2		9.5e−14×exp(390/*T*)×0.5	h
B50b	CH_3O_2+$C_2H_5O_2$→ CH_3OH+CH_3CHO+O_2		9.5e−14×exp(390/*T*)×0.3	h
B50c	CH_3O_2+$C_2H_5O_2$→ CH_2O+C_2H_5OH+O_2		9.5e−14×exp(390/*T*)×0.2	h
B51a	CH_3O_2+$CH_3C(O)O_2$(+2O_2) →CH_2O+HO_2+CH_3O_2+O_2		2.0e−12×exp(500/*T*)×0.9	b
B51b	CH_3O_2+$CH_3C(O)O_2$→CH_2O+$CH_3C(O)OH$+O_2		2.0e−12×exp(500/*T*)×0.1	b
B52a	CH_3O_2+$CH_3C(O)CH_2O_2$(+2O_2)→$CH_3C(O)O_2$+2CH_2O+HO_2+O_2		7.5e−13×exp(500/*T*)×0.5	i
B52b	CH_3O_2+$CH_3C(O)CH_2O_2$→CH_3OH+$CH_3C(O)CHO$		7.5e−13×exp(500/*T*)×0.2	i
B52c	CH_3O_2+$CH_3C(O)CH_2O_2$→CH_2O+$CH_3C(O)CH_2OH$		7.5e−13×exp(500/*T*)×0.3	i
B53	CH_3O_2+Isop(OH)O_2→MACR+2CH_2O+2HO_2		1.3e−14	c

B54	$CH_3O_2+MCO_3 \rightarrow CH_3C(O)CHO + CH_2O + HO_2$	1.3e−14	c
B55	$HO_2+NO \rightarrow NO_2+OH$	3.3e−12×exp(270/*T*)	a
B56	$CH_3O_2+NO(+O_2) \rightarrow NO_2+CH_2O+HO_2$	2.8e−12×exp(300/*T*)	a
B57	$C_2H_5O_2+NO(+O_2) \rightarrow NO_2+CH_3CHO+HO_2$	2.6e−12×exp(365/*T*)	a
B58	$C_2H_4OHO_2+NO(+O_2) \rightarrow 2CH_2O+HO_2+NO_2$	Assumed = k_{B57}	
B59	$CH_3C(O)O_2+NO(+O_2) \rightarrow NO_2+CH_3O_2+CO_2$	7.5e−12×exp(290/*T*)	a
B60	$CH_3C(O)CH_2O_2+NO \rightarrow CH_3C(O)O_2+CH_2O+NO_2$	2.9e−12×exp(300/*T*)	a
B61	$Isop(OH)O_2+NO \rightarrow 0.59CH_3CO_3+CH_2O+0.59CH_2OHCHO+0.59NO_2+0.41RNO_3$	5e−13×exp(180/*T*)	g
B62	$Isop(OH)O_2+NO \rightarrow 0.42MVK+0.58MACR+CH_2O+HO_2+NO_2$	3e−12×exp(180/*T*)	g
B63	$MOHO_2+NO \rightarrow CH_2OHCHO+CH_3C(O)O_2+NO_2$	3.5e−12×exp(180/*T*)	g
B64	$MCO_3+NO \rightarrow CH_3COCHO+NO_2$	2.4e−11	g
B65	$ArO_2+NO \rightarrow NO_2+HO_2+others$	4.2e−12×exp(180/*T*)	f
B66	$R(NO_3)O_2+NO \rightarrow NO_2+HO_2+others$	4.2e−12×exp(180/*T*)	f
B67	$OH+NO_3 \rightarrow HO_2+NO_2$	2.0e−11	b
B68	$HO_2+NO_3 \rightarrow 0.7OH+0.7NO_2+0.3HNO_3+O_2$	4.0e−12	b
B69	$CH_3O_2+NO_3(+O_2) \rightarrow CH_2O+HO_2+NO_2+O_2$	1.8e−11×exp(−460/*T*)	b
B70	$C_2H_5O_2+NO_3(+O_2) \rightarrow CH_3CHO+HO_2+NO_2+O_2$	4.8e−12×exp(−300/*T*)	a
B71	$CH_3C(O)O_2+NO_3(+O_2) \rightarrow CH_3O_2+CO_2+HO_2+NO_2+O_2$	8.8e−12×exp(260/*T*)	a
B72	$O_3+Br \rightarrow BrO+O_2$	1.6e−11×exp(−780/*T*)	a
B73	$Br+CH_2O(+O_2) \rightarrow HBr+HO_2+CO$	1.7e−11×exp(−800/*T*)	a
B74	$Br+CH_3CHO(+O_2) \rightarrow HBr+CH_3C(O)O_2$	1.8e−11×exp(−460/*T*)	b
B75	$Br+HO_2 \rightarrow HBr+O_2$	4.8e−12×exp(−300/*T*)	a
B76	$BrO+NO \rightarrow Br+NO_2$	8.8e−12×exp(260/*T*)	a
B77a	$BrO+BrO \rightarrow Br+Br+O_2$	2.4e−12×exp(40/*T*)	a
B77b	$BrO+BrO \rightarrow Br_2+O_2$	2.8e−14×exp(860/*T*)	a
B78a	$BrO+ClO \rightarrow Br+OClO$	9.5e−13×exp(550/*T*)	a
B78b	$BrO+ClO \rightarrow Br+ClOO$	2.3e−12×exp(260/*T*)	a
B78c	$BrO+ClO \rightarrow BrCl+O_2$	4.1e−13×exp(290/*T*)	a
B79	$BrO+HO_2 \rightarrow HOBr+O_2$	4.5e−12×exp(460/*T*)	a
B80a	$BrO+CH_3O_2(+O_2) \rightarrow Br+ O_2+ CH_2O+ HO_2$	4.6e−13×exp(798/*T*)×0.25	b
B80b	$BrO+CH_3O_2 \rightarrow HOBr + CH_2O_2$	4.6e−13×exp(798/*T*)×0.75	b

B81	$OH+HBr \rightarrow Br+H_2O$	$5.5e{-}12\times\exp(200/T)$	a
B82	$OH+Br_2 \rightarrow HOBr+Br$	$2.1e{-}11\times\exp(240/T)$	a
B83	$BrO+O(^3P) \rightarrow Br+O_2$	$1.9e{-}11\times\exp(230/T)$	a
B84	$HOBr+O(^3P) \rightarrow BrO+OH$	$1.2e{-}10\times\exp(-430/T)$	a
B85	$BrNO_3+O(^3P) \rightarrow BrO+NO_3$	$1.9e{-}11\times\exp(215/T)$	a
B86	$HBr+O(^3P) \rightarrow Br+OH$	$5.8e{-}12\times\exp(-1500/T)$	a
B87a	$HBr+O(^1D) \rightarrow BrO+H$	$3e{-}11$	a
B87b	$HBr+O(^1D) \rightarrow Br+OH$	$9e{-}11$	a
B88	$O_3+Cl \rightarrow ClO+O_2$	$2.3e{-}11\times\exp(-200/T)$	a
B89	$Cl+CH_4(+O_2) \rightarrow CH_3O_2+HCl$	$7.1e{-}12\times\exp(-1270/T)$	a
B90	$Cl+C_2H_6(+O_2) \rightarrow C_2H_5O_2+HCl$	$7.2e{-}11\times\exp(-70/T)$	a
B91	$Cl+CH_3OH(+O_2) \rightarrow HO_2+CH_2O+HCl$	$5.5e{-}11$	a
B92	$Cl+CH_2O(+O_2) \rightarrow HO_2+CO++HCl$	$8.1e{-}11\times\exp(-30/T)$	a
B93	$Cl+CH_3C(O)CH_3(+O_2) \rightarrow CH_3C(O)CH_2O_2+HCl$	$7.7e{-}11\times\exp(-1000/T)$	a
B94	$Cl+H_2O_2 \rightarrow HO_2+HCl$	$1.1e{-}11\times\exp(-980/T)$	a
B95a	$Cl+HO_2 \rightarrow HCl+O_2$	$1.4e{-}11\times\exp(270/T)$	a
B95b	$Cl+HO_2(+O_2) \rightarrow OH+ClO$	$3.6e{-}11\times\exp(-375/T)$	a
B96	$ClO+HO_2 \rightarrow HOCl+O_2$	$2.6e{-}12\times\exp(290/T)$	a
B97	$ClO+NO \rightarrow Cl+NO_2$	$6.4e{-}12\times\exp(290/T)$	a
B98a	$ClO+ClO \rightarrow Cl_2+O_2$	$1.0e{-}12\times\exp(-1590/T)$	a
B98b	$ClO+ClO \rightarrow Cl+Cl+O_2$	$3.0e{-}11\times\exp(-2450/T)$	a
B98c	$ClO+ClO \rightarrow Cl+OClO$	$3.5e{-}13\times\exp(-1370/T)$	a
B99	$OH+OClO \rightarrow HOCl+O_2$	$1.4e{-}12\times\exp(600/T)$	a
B100	$OClO+NO \rightarrow ClO+NO_2$	$2.5e{-}12\times\exp(-600/T)$	a
B101	$OH+HCl \rightarrow H_2O+Cl$	$1.8e{-}12\times\exp(-250/T)$	a

a. Rate constants taken from JPL compilation 2015 [*Burkholder et al.*, 2015].
b. Rate constants taken from IUPAC kinetics: http://iupac.pole-ether.fr/
c. Rate constants taken from IUPAC kinetics (http://iupac.pole-ether.fr/). Branching ratios taken from *Brasseur et al.* [1998].
d. Rate constants taken from IUPAC kinetics (http://iupac.pole-ether.fr/). Branching ratios taken from MCM v3 [*Jenken et al.*, 2003]
e. The ozonolysis of alkenes generates Criegee Intermediates (CI)
$O_3+C_2H_4 \rightarrow CH_2O+[CH_2OO]^*$
$O_3+C_3H_6 \rightarrow CH_2O+[CH_3CH_2OO]^*$ (50%)

→CH_3CHO+[CH_2OO]* (50%)

The branching ratios for the subsequent reactions of CI are assigned as followed, according to the IUPAC (http://iupac.pole-ether.fr/). Rate constants are taken from IUPAC kinetics (http://iupac.pole-ether.fr/).

[CH_2OO]*(+M)→ CH_2OO (stabilized) + M (37%)
→ CO+H_2O
→ CO_2+H_2
→ OH+HO_2+CO (16%)

[CH_3CH_2OO]*(+M)→ CH_3CH_2OO (stabilized) + M (16%)
→ OH+CH2CHO (45%)
→CH_2CO+H_2O (5%)
→CH_3OH+CO (9%)
→ CH_4+CO_2 (15%)
→ others (16%)

f. Estimated according to *Atkinson et al*. [2007].

g. *Brasseur et al.* [1998].

h. Total rate constants taken from JPL compilation 2015 [*Burkholder et al.*, 2015]. Branching ratios are assumed to be the same as reaction B49.

i. Total rate constants taken from JPL compilation 2010 [*Burkholder et al.*, 2015]. Branching ratios (measured at 298K) taken from IUPAC kinetics http://iupac.pole-ether.fr/

Table A 2. Termolecular reactions.

No.	Reaction	k_0/ cm^6·s^{-1}	k_∞/ cm^3·s^{-1}	*Fc*	Notes
T1	$O_2+O(^3P)+M \rightarrow O_3+M$	$6.0e{-}34\times(T/300)^{-2.4}$		0.6	a
T2	$OH+NO+M \rightarrow HONO+M$	$7.0e{-}31\times(T/300)^{-2.6}$	$3.6e{-}11\times(T/300)^{-0.1}$	0.6	a,c
T3	$OH+NO_2+M \rightarrow HNO_3+M$	$1.8e{-}30\times(T/300)^{-3.0}$	$2.8e{-}11$	0.6	a,c
T4a	$OH+CO+M \rightarrow HOCO+M$	$5.9e{-}33\times(T/300)^{-1.0}$	$1.1e{-}12\times(T/300)^{-1.3}$	0.6	a,d
T4b	$OH+CO+M \rightarrow H+CO_2+M$	$1.5e{-}13$	$2.1e{+}9\times(T/300)^{6.1}$	0.6	a,d
T5	$OH+OH+M \rightarrow H_2O_2+M$	$6.9e{-}31\times(T/300)^{-1.0}$	$2.6e{-}11$	0.6	a,c
T6	$OH+C_2H_4(+O_2) \rightarrow C_2H_4(OH)O_2+H_2O$	$1.1e{-}28\times(T/300)^{-3.5}$	$8.4e{-}12\times(T/200)^{-1.75}$	0.6	a,c
T7	$OH+C_3H_6(+O_2) \rightarrow C_3H_6(OH)O_2+H_2O$	$8.6e{-}27\times(T/300)^{-3.5}$	$3e{-}11\times(T/300)^{-1}$	0.5	b,c
T8	$HO_2+NO_2+M \rightarrow HNO_4+M$	$1.9e{-}31\times(T/300)^{-3.4}$	$4.0e{-}12\times(T/300)^{-0.3}$	0.6	a,c
T9	$NO_2+NO_3+M \rightarrow N_2O_5+M$	$2.4e{-}30\times(T/300)^{-3.0}$	$1.6e{-}12\times(T/300)^{0.1}$	0.6	a,c
T10	$CH_3C(O)O_2+NO_2+M \rightarrow PAN+M$	$9.7e{-}29\times(T/300)^{-5.6}$	$9.3e{-}12\times(T/300)^{-1.5}$	0.6	a,c
T11	$BrO+NO_2+M \rightarrow BrNO_3+M$	$5.4e{-}31\times(T/300)^{-3.1}$	$6.5e{-}12\times(T/300)^{-2.9}$	0.6	a,c
T12	$ClO+NO_2+M \rightarrow ClNO_3+M$	$1.8e{-}31\times(T/300)^{-3.4}$	$1.5e{-}11\times(T/300)^{-1.9}$	0.6	a,c
T13	$ClO+ClO+M \rightarrow Cl_2O_2+M$	$1.9e{-}32\times(T/300)^{-3.6}$	$3.7e{-}12\times(T/300)^{-1.6}$	0.6	a,c

a. Rate constant taken from JPL compilation 2015 [*Burkholder et al.*, 2015].
b. Rate constants taken from IUPAC kinetics (http://iupac.poleether.fr/).
c. To obtain the effective second-order rate constant in cm^3·s^{-1}, the following formula is used:

$$k([\mathrm{M}],T)=\left(\frac{k_0(T)\times[\mathrm{M}]}{1+\frac{k_0(T)\times[\mathrm{M}]}{k_\infty(T)}}\right)\times Fc^{\left\{1+\left[\log_{10}\left(\frac{k_0(T)\times[\mathrm{M}]}{k_\infty(T)}\right)\right]^2\right\}^{-1}}$$

d. To obtain the effective second-order rate constant in cm^3·s^{-1}, the following formula is used:

$$k([\mathrm{M}],T)=\left(\frac{k_0(T)}{1+\frac{k_0(T)}{k_\infty(T)/[\mathrm{M}]}}\right)\times Fc^{\left\{1+\left[\log_{10}\left(\frac{k_0(T)}{k_\infty(T)/[\mathrm{M}]}\right)\right]^2\right\}^{-1}}$$

where $k_0(T)$ in cm^3·s^{-1}. and $k_\infty(T)$ in s^{-1}.
d. Reaction OH+CO occurs via two channels (T4a, T4b). In the atmosphere, both HOCO and H are converted to HO_2 immediately, and both channels yield the same products HO_2

+ CO_2. The overall rate constant for $OH+CO \rightarrow HO_2+CO_2$ is the sum of the rate constants for both channels.

Table A 3. Equilibrium constants.

No.	Equilibrium	K /cm^3	Note
E1	$HO_2+NO_2+M \leftrightarrow HO_2NO_2+M$	2.1e–27×exp(10900/T)	a
E2	$NO_2+NO_3+M \leftrightarrow N_2O_5+M$	2.7e–27×exp(11000/T)	a
E3	$CH_3C(O)O_2+NO_2+M \leftrightarrow PAN+M$	9.0e–29×exp(14000/T)	a
E4	$ClO+ClO+M \leftrightarrow Cl_2O_2+M$	2.16e−27×exp(8537/T)	a

a. Rate constant taken from JPL compilation 2015 [*Burkholder et al.*, 2015].

Table A 4. Photo-dissociation reactions.

No.	Reaction
P1	$O_3+h\upsilon \rightarrow O_2+O(^1D)$
P2	$NO_2+h\upsilon(+O_2) \rightarrow NO+O_3$
P3	$H_2O_2+h\upsilon \rightarrow OH+OH$
P4	$HONO+ h\upsilon \rightarrow OH+NO$
P5a	$HO_2NO_2+ h\upsilon \rightarrow HO_2+NO_2$
P5b	$HO_2NO_2+ h\upsilon \rightarrow OH+NO_3$
P6a	$NO_3+ h\upsilon \rightarrow NO+O_2$
P6b	$NO_3+ h\upsilon \rightarrow NO_2+O(^3P)$
P7	$N_2O_5+ h\upsilon \rightarrow NO_3+NO_2$
P8a	$CH_2O+h\upsilon(+2O_2) \rightarrow 2HO_2+CO$
P8b	$CH_2O+h\upsilon \rightarrow CO+H_2$
P9	$CH_3OOH+h\upsilon \rightarrow CH_3O+OH$
P10	$CH_3CHO+h\upsilon(+2O_2) \rightarrow CH_3O_2+HO_2+CO$
P11	$CH_3C(O)CH_3+h\upsilon(+2O_2) \rightarrow CH_3C(O)O_2+CH_3O_2$
P12a	$PAN+ h\upsilon \rightarrow CH_3C(O)O_2+NO_2$
P12b	$PAN+ h\upsilon(+O_2) \rightarrow CH_3O_2+CO_2+NO_3$
P13	$Br_2+h\upsilon \rightarrow Br+Br$
P14	$BrO+h\upsilon \rightarrow Br+O(^3P)$
P15a	$BrNO_3+h\upsilon \rightarrow BrO+NO_2$
P15b	$BrNO_3+h\upsilon \rightarrow Br+NO_3$
P16	$HOBr+h\upsilon \rightarrow OH+Br$
P17	$Cl_2+h\upsilon \rightarrow Cl+Cl$
P18	$ClO+h\upsilon \rightarrow Cl+O(^3P)$
P19a	$ClNO_3+h\upsilon \rightarrow ClO+NO_2$
P19b	$ClNO_3+h\upsilon \rightarrow Cl+NO_3$
P20	$HOCl+h\upsilon \rightarrow OH+Cl$
P21	$Cl_2O_2+h\upsilon \rightarrow Cl+Cl+O_2$
P22	$OClO+h\upsilon \rightarrow ClO+ O(^3P)$

Table A 5. Heterogeneous reactions.

No.	Reaction X+ Y→ P	reactive uptake coefficient γ	Note
H1	HOBr +HCl→BrCl+H_2O	4×10^{-3}	a
H2	HOBr +HBr→Br_2+H_2O	0.1	a,
H3	HOCl +HCl→Cl_2+H_2O	0.1	a
H4	HOCl +HBr→BrCl+H_2O	$(0.3+2.7/\theta_{HBr})^{-1}$	a, b
H5	$BrNO_3$+H_2O →HOBr+HNO_3	0.1	a
H6	$BrNO_3$+HBr →Br_2 +HNO_3	0.2	a
H7	$BrNO_3$+HCl →BrCl+HNO_3	0.3	a
H8	$ClNO_3$+H_2O →HOCl+HNO_3	0.01	a
H9	$ClNO_3$+HBr →BrCl+HNO_3	$0.56\times\theta_{HBr}$	a, b
H10	$ClNO_3$+HCl →Cl_2+HNO_3	0.04	a

a: IUPAC kinetics: http://iupac.pole−ether.fr/,also seen in *Crowley et al*. [2010].
b: the unitless surface coverage of HBr (θ_{HBr}) is a function of gas phase [HBr] (in cm^{-3}). θ_{HBr} should always be ≤1.

$$\theta_{HBr} = 4.14 \times 10^{-10}[HBr]^{0.88}$$

REFERENCES

Abida, O., L. H. Mielke, and H. D. Osthoff (2011), Observation of gas-phase peroxynitrous and peroxynitric acid during the photolysis of nitrate in acidified frozen solutions, *Chem. Phys Lett.*, *511*, 187−192.

Anderson, D. C., J. M. Nicely, R. J. Salawitch, T. P. Canty, R. R. Dickerson, T. F. Hanisco, G. M. Wolfe, E. C. Apel, E. Atlas, T. Bannan, S. Bauguitte, N. J. Blake, J. F. Bresch, T. L. Campos, L. J. Carpenter, M. D. Cohen, M. Evans, R. P. Fernandez, B. H. Kahn, D. E. Kinnison, S. R. Hall, N. R. P. Harris, R. S. Hornbrook, J.-F. Lamarque, M. Le Breton, J. D. Lee, C. Percival, L. Pfister, R. B. Pierce, D. D. Riemer, A. Saiz-Lopez, B. J. B. Stunder, A. M. Thompson, K. Ullmann, A. Vaughan and A. J. Weinheimer (2016a), A pervasive role for biomass burning in tropical high ozone/low water structures, *Nature Communications*, *7*:10267, doi: 10.1038/ncomms10267.

Anderson, D. C. *et al.* (2016b), Formaldehyde in the Tropical Western Pacific: Evaluation of the HCHO distribution, satellite retrievals, models, and its effects on the atmospheric oxidative capacity, in preparation, to be submitted to *J. Geophys. Res. Atmos.*

Ashfold, M. J., N. R. P. Harris, E. L. Atlas, A. J. Manning, and J. A. Pyle (2012), Transport of short-lived species into the Tropical Tropopause Layer, *Atmos. Chem. Phys.*, *12*, 6309-6322, doi: 10.5194/acp-12-6309-2012.

Aschmann, J., B.-M. Sinnhuber, E. L. Atlas, and S. Schauffler (2009), Modeling the transport of very short-lived substance into the tropical upper troposphere and lower stratosphere, *Atmos. Chem. Phys.*, *9*, 9237-9247.

Aschmann, J., and B.-M. Sinnhuber (2013), Contribution of very short-lived substances to stratospheric bromine loading: uncertainties and constraints, *Atmos. Chem. Phys.*, *13*, 1203-1219, doi: 10.5194/acp-13-1203-2013.

Atkinson, R.: Gas-phase tropospheric chemistry of organic compounds: a review, *Atmos. Environ.*, *41*., S200-S400, 2007.

Bacak, A., M. C. Cooke, M. W. Bardwell, M. R. McGillen, A. T. Archibald, L. G. Huey, D. J. Tanner, S. R. Utembe, M. E. Jenkin, R. G. Derwent, D. E. Shallcross, and C. J. Percival (2011), Kinetics of the HO_2+NO_2 Reaction: On the impact of new gas-

phase kinetic data for the formation of HO_2NO_2 on HO_x, NO_x and HO_2NO_2 levels in the troposphere, *Atmos. Environ.*, *45*, 6414-6422, doi:10.1016/j.atmosenv.2011.08.008.

Bey, I., D. J. Jacob, R. M. Yantosca, J. A. Logan, B. D. Field, A. M. Fiore, Q. B. Li, H. G. Y. Liu, L. J. Mickley, and M. G. (2001), Global modeling of tropospheric chemistry with assimilated meteorology: Model description and evaluation, *J. Geophys. Res.*, *106*(D19), 23073–23095, doi: 10.1029/2001JD000807.

Bertram, T. H., and J. A. Thornton (2009), Toward a general parameterization of N_2O_5 reactivity on aqueous particles: the competing effects of particle liquid water, nitrate and chloride, *Atmos. Chem. Phys.*, *9*, 8351-8363.

Brasseur, G. P., D. A. Hauglustaine, S. Walters, P. J. Rasch, J.-F. Müller, J.-F., C. Granier, and X. X. (1998), MOZART, a global chemical transport model for ozone and related chemical tracers 1. Model description, *J. Geophys. Res.*, *103*(D21), 28265-28289.

Brown, S. S., J. A. de Gouw, C. Warneke, T. B. Ryerson, W. P. Dubé, E. Atlas, R. J. Weber, R. E. Peltier, J. A. Neuman, J. M. Roberts, A. Swanson, F. Flocke, S. A. McKeen, J. Brioude, R. Sommariva, M. Trainer, F. C. Fehsenfeld, and A. R. Ravishankara (2009), Nocturnal isoprene oxidation over the Northeast United States in summer and its impact on reactive nitrogen partitioning and secondary organic aerosol, *Atmos. Chem. Phys.*, *9*, 3027–3042.

Browne, E. C., A. E. Perring, P. J. Wooldridge, E. Apel, S. R. Hall, L. G. Huey, J. Mao, K. M. Spencer, J. M. St. Clair, A. J. Weinheimer, A. Wisthaler, and R. C. Cohen (2011), Global and regional effects of the photochemistry of $CH_3O_2NO_2$: evidence from ARCTAS, *Atmos. Chem. Phys.*, *11*, 4209–4219, doi: 10.5194/acp-11-4209-2011.

Burkholder, J. B., S. P. Sander, J. P. D. Abbatt, J. R. Barker, R. E. Huie, C. E. Kolb, M. J. Kurylo, V. L. Orkin, D. M. Wilmouth, and P. H. Wine (2015), Chemical Kinetics and Photochemical Data for Use in Atmospheric Studies, Evaluation No. 18, JPL Publication 15−10, Jet Propulsion Laboratory, Pasadena, USA, http://jpldataeval.jpl.nasa.gov.

Carpenter, L. J. and S. Reimann (Lead Authors), J. B. Burkholder, C. Clerbaux, B. D. Hall, R. Hossaini, J. C. Laube, and S. A. Yvon-Lewis (2014), Ozone-Depleting Substances (ODSs) and Other Gases of Interest to the Montreal Protocol, Chapter 1 in *Scientific Assessment of Ozone Depletion: 2014*, Global Ozone Research and

Monitoring Project-Report No. 55, World Meteorological Organization, Geneva, Switzerland.

Carton, A. G., C. Wiedinmyer, and J. H. Kroll (2009), A review of Secondary Organic Aerosol (SOA) formation from isoprene, *Atmos. Chem. Phys.*, *9*, 4987–5005.

Chameides, W., and J. C. G. Walker (1973), A photochemical theory of tropospheric ozone, *J. Geophys. Res.*, *78*, 36.

Chen D *et al.* (2016), Measurement of pernitric acid (HO_2NO_2) at Summit, Greenland using chemical ionization mass spectrometry (CIMS) with the reagent ions $I^-/I^-\cdot H_2O$, *in preparation*.

Chen, D., L. G. Huey, D. J. Tanner, J. Li, N. L. Ng, and Y. Wang (2016a), Inferring hydroperoxyl radical (HO_2) in an urban site via measurement of pernitric acid (HO_2NO_2) using chemical ionization mass spectrometry (CIMS) with the reagent ion $I^-\cdot(H_2O)_n$, *in preparation*.

Chen, D., L. G. Huey, D. J. Tanner, R. J. Salawitch, D. C. Anderson, P. A. Wales, L. L. Pan, E. L. Atlas, R. S. Hornbrook, E. C. Apel, N. J. Blake, T. L. Campos, V. Donets, F. M. Flocke, S. R. Hall, T. F. Hanisco, A. J. Hills, S. B. Honomichl, J. B. Jensen, L. Kaser, D. D. Montzka, J. M. Nicely, J. M. Reeves, D. D. Riemer, S. M. Schauffler, K. Ullmann[5], A. J. Weinheimer, and G. M. Wolfe (2016b), Airborne measurements of BrO and the sum of HOBr and Br_2 over the tropical West Pacific from 1 to 15 km during the CONvective TRansport of Active Species in the Tropics (CONTRAST) experiment, submitted to *J. Geophys. Res. Atmos.*

Chen, G., D. D. Davis, J. Crawford, J. B. Nowak, F. Eisele, R. L. Mauldin II, D. J. Tanner, M. Buhr, R. Shetter, B. Lefer, R. Arimoto, A. Hogan, and D. Blake (2001), An Investigation of South Pole HO_x chemistry: comparison of model results with ISCAT observations, *Geophys. Res. Lett.*, *28*, 3633-3636.

Chen, G., D. Davis, J. Crawford, L. M. Hutterli, L. G. Huey, D. Slusher, L. Mauldin, F. Eisele, D. Tanner, J. Dibb, M. Buhr, J. McConnell, B. Lefer, R. Shetter, D. Blake, C. H. Song, K. Lombardi, and J. Arnoldy (2004), A reassessment of HO_x South Pole chemistry based on observations recorded during ISCAT 2000, *Atmos. Environ.*, *38*, 5451-5461, doi:10.1016/j.atmosenv.2003.07.018.

Choi, S., Y. Wang, R. J. Salawitch, T. Canty, J. Joiner, T. Zeng, T. P. Kurosu, K. Chance, A. Richter, L. G. Huey, J. Liao, J. A. Neuman, J. B. Nowak, J. E. Dibb, A. J. Weinheimer, G. Diskin, T. B. Ryerson, A. da Silva, J. Curry, D. Kinnison, S.

Tilmes, and P. F. Levelt (2012), Analysis of satellite-derived Arctic tropospheric BrO columns in conjunction with aircraft measurements during ARCTAS and ARCPAC, *Atmos. Chem. Phys.*, *12*, 1255–1285, doi:10.5194/acp-12-1255-2012.

Choi, Y., Y. H. Wang, T. Zeng, R. V. Martin, T. P. Kurosu, and K. Chance (2005), Evidence of lightning NO_x and convective transport of pollutants in satellite observations over North America, *Geophys. Res. Lett.*, *32*, L02805, doi: 10.1029/2004GL021436.

Christensen, L. E., M. Okumura, S. P. Sander, R. R. Friedl, C. E. Miller, and J. J. Sloan (2004), Measurements of the rate constant of $HO_2 + NO_2 + N_2 \rightarrow HO_2NO_2 + N_2$ using near-infrared wavelength-modulation spectroscopy and UV-visible absorption spectroscopy, *J. Phys. Chem. A, 108*, 80-91.

Commane, R., C. F. A. Floquet, T. Ingham, D. Stone, M. J. Evans, and D. E. Heard, D (2010), Observations of OH and HO_2 radicals over West Africa, *Atmos. Chem. Phys.*, *10*, 8783–8801, doi:10.5194/acp-10-8783-2010.

Crowley, J. N., M. Ammann, R. A. Cox, R. G. Hynes, M. E. Jenkin, A. Mellouki, M. J. Rossi, J. Troe, and, T. J. Wallington (2010): Evaluated kinetic and photochemical data for atmospheric chemistry: Volume V – heterogeneous reactions on solid substrates, *Atmos. Chem. Phys*., *10*, 9059–9223, doi:10.5194/acp−10−9059−2010, http://www.atmos−chem−phys.net/10/9059/2010/.

Crutzen, P. (1974), A Review of upper atmosphere photochemistry, *Can. J. Chem.*, *52*, 1569-1581.

Danilin, M. Y., N.-D. Sze, M. K. W. Ko, J. M. Rodriguez, and M. J. Prather (1996), Bromine-chlorine coupling in the Antarctic ozone hole, *Geophys. Res. Lett.*, *23*(2), 153-156.

Daniel, J. S., S. Solomon, R. W. Portmann, and R. R. Garcia (1999), Stratospheric ozone destruction: the importance of bromine relative to chlorine, *J. Geophys. Res. Atmos.*, *104*(D19), 23871-23880.

Dibb, J. E., L. D. Ziemba, J. Luxford, and P. Beckman (2010), Bromide and other ions in the snow, firn air, and atmospheric boundary layer at Summit during GSHOX, *Atmos. Chem. Phys.*, *10*, 9931-9942.

Dorf, M., A. Butz, C. Camy-Peyret, M. P. Chipperfield, L. Kritten, and K. Pfeilsticker (2008), Bromine in the tropical troposphere and stratosphere as derived from balloon-borne BrO observations, *Atmos. Chem. Phys., 8*, 7265–7271.

Fernandez, R. P., R. J. Salawitch, D. E. Kinnison, J.-F. Lamarque, and A. Saiz-Lopez (2014), Bromine partitioning in the tropical tropopause layer: implications for stratospheric injection, *Atmos. Chem. Phys., 14*, 13391-13410.

Finlayson-Pitts, B. J., and J. N. Pitts Jr (2000), Chemistry of the upper and lower atmosphere, theory, experiments and applications, Academic Press, San Diego, USA.

Fitzenberger, R., H. Bösch, C. Camy-Peyret, M. P. Chipperfield, H. Harder, U. Platt, B.-M. Sinnhuber, T. Wagner, and K. Pfeilsticker (2000), First Profile Measurements of Tropospheric BrO, *Geophys. Res. Lett.*, *27*(18), 2921-2924.

Frieler, K., M. Rex, R. J. Salawitch, T. Canty, M. Streibel, R. M. Stimpfle, K. Pfeilsticker, M. Dorf, D. K. Weisenstein, and S. Godin-Beekmann (2006), Toward a better quantitative understanding of polar stratospheric ozone loss, *Geophys. Res. Lett.*, *33*, L10812.

Fuchs, H., F. Holland, and A. Hofzumahaus (2008), Measurement of tropospheric RO_2 and HO_2 radicals by a laser-induced fluorescence instrument, *Rev. Sci. Instrum*. *79*, 084104.

Garcia, R. R., and S. Solomon (1994), A new numerical model of the middle atmosphere 2. Ozone and related species, *J. Geophys. Res. Atmos.*, *99*(D6), 12931-23951.

Geyer, A., K. Bächmann, A. Hofzumahaus, F. Holland, S. Konrad, T. Klüpfel, H. -W. Pätz, D. Perner, D. Mihelcic, H. -J. Schäfer, A. Volz-Thomas, and U. Platt (2003), Nighttime formation of peroxy and hydroxyl radicals during the BERLIOZ campaign: Observations and modeling studies, *J. Geophys., Res. Atmos*., *108*, D4, 8249, doi:10.1029/2001JD000656

Gierczak, T., E. Jimenez, V. Riffault, J. B. Burkholder, and A. R. Ravishankara (2005), Thermal decomposition of HO_2NO_2 (Peroxynitric Acid, PNA): rate coefficient and determination of the enthalpy of formation, *J. Phys. Chem. A, 109*, 586-596.

von Glasow, R., R. von Kuhlmann, M. G. Lawrence, U. Platt, and P. J. Crutzen (2004), Impact of reactive bromine chemistry in the troposphere, *Atmos. Chem. Phys.*, *4*, 2481–2497.

Hanson, D. R., and A. R. Ravishankara (1991), The reaction probabilities of $ClONO_2$ and N_2O_5 on polar stratospheric cloud materials, *J. Geophys. Res. Atmos.*, *96*, D3, 5081-5090

Hebestreit, K., J. Stutz, D. Rosen, V. Matveiv, M. Peleg, M. Luria, and U. Platt (1999), DOAS Measurements of Tropospheric Bromine Oxide in Mid-Latitudes, *Science*, *283*, 55-57.

Holland, F., A. Hofzumahaus, J. Schäfer, A. Kraus, and H. -W. Pätz (2003), Measurements of OH and HO_2 radical concentrations and photolysis frequencies during BERLIOZ, *J. Geophys. Res. Atmos.*, *108*, D4, 8246, doi:10.1029/2001JD001393.

Holzinger, R., C. Warneke, A. Hansel, A. Jordan and W. Lindinger (1999), Biomass burning as a source of formaldehyde, acetaldehyde, methanol, acetone, acetonitrile, and hydrogen cyanide, *Geophys. Res. Lett.*, *26*(8), 1161-1164.

Hönninger, G., H. Leser, O. Sebastián, and U. Platt (2004), Ground-based measurements of halogen oxides at the Hudson Bay by active long path DOAS and passive MAX-DOAS, *Geophys. Res. Lett.*, *31*, L04111.

Hossaini, R., M. P. Chipperfield, B. M. Monge-Sanz, N. A. D. Richards, E. Atlas, and D. R. Blake (2010), Bromoform and dibromomethane in the tropics: a 3-D model study of chemistry and transport, *Atmos. Chem. Phys.*, *10*, 719-735.

Huey, L. G., D. R. Hanson, and C. J. Howard (1995), Reactions of SF_6^- and I^- with atmospheric trace gases, *J. Phys. Chem.*, *99*, 5001-5008.

Huey, L. G., E. J. Dunlea, E. R. Lovejoy, D. R. Hanson, R. B. Norton, F, C. Fehsenfeld and C. J. Howard (1998), Fast time response measurements of HNO_3 in air with a chemical ionization mass spectrometer, *J. Geophys. Res.*, *103*, D3, 3355-3360.

Huey, L. G. (2007), Measurement of trace atmospheric species by Chemical Ionization Mass Spectrometry: speciation of reactive nitrogen and future directions, *Mass Spectrom Rev.*, *26*, 166-184.

Iraci, L. T., R. R. Michelsen, S. F. M. Ashbourn, T. A. Rammer, and D. M. Golden (2005), Uptake of hypobromous acid (HOBr) by aqueous sulfuric acid solutions: low-temperature solubility and reaction, *Atmos. Chem. Phys.*, *5*, 1577-1587.

Jacob, D. J. (2000), Heterogeneous chemistry and tropospheric ozone, *Atmos. Environ.*, 34, 2131–2159.

Jaeglé, L., D. J. Jacob, W. H. Brune, and P. O. Wennberg (2001), Chemistry of HO_x radicals in the upper troposphere, *Atmos. Environ.*, *35*, 469-489

Jenkin, M. E., S. M. Saunders, V. Wagner, and M. J. Pilling (2003), Protocol for the development of the Master Chemical Mechanism, MCM v3 (Part B): tropospheric degradation of aromatic volatile organic compounds, *Atmos. Chem. Phys.*, *3*, 181-193.

Jiménez, E., T. Gierczak, H. Stark, H., J. B. Burkholder, and A. R. Ravishankara (2004), Reaction of OH with HO_2NO_2 (peroxynitric acid): rate coefficients between 218 and 335 K and product yields at 298 K, *J. Phys. Chem. A*, 108, 1139-1149.

Jing, P., D. Cunnold, Y. Choi, and Y. Wang (2006), Summertime tropospheric ozone columns from Aura OMI/MLS measurements versus regional model results over the United States, *Geophys. Res. Lett*., *33*, L17817, doi: 10.1029/2006GL026473.

Johnson, D., and G. Marston (2008), The gas-phase ozonolysis of unsaturated volatile organic compounds in the troposphere, *Chem. Soc. Rev.*, *37*, 699–716.

Jones, A. E., N. Brough, P. S. Anderson, and E. W. Wolff (2014), HO_2NO_2 and HNO_3 in the coastal Antarctic winter night: a "lab-in-the-field" experiment, *Atmos. Chem. Phys.*, *14*, 11843–11851, doi:10.5194/acp-14-11843-2014.

Kanaya, Y., R. Q. Cao, H. Akimoto, M. Fukuda, Y. Komazaki, Y. Yokouchi, M. Koike, H. Tanimoto, N. Takegawa, and Y. Kondo (2007), Urban photochemistry in central Tokyo: 1. Observed and modeled OH and HO_2 radical concentrations during the winter and summer of 2004, *J. Geophys. Res. Atmos.*, *112*(D21), doi:10.1029/2007jd008670.

Kanaya, Y., A. Hofzumahaus, H.-P. Dorn, T. Brauers, H. Fuchs, F. Holland, F. Rohrer, B. Bohn, R. Tillmann, R. Wegener, A. Wahner, Y. Kajii, K. Miyamoto, S. Nishida, K. Watanabe, A. Yoshino, D. Kubistin, M. Martinez, M. Rudolf, H. Harder, H. Berresheim, T. Elste, C. Plass-Dülmer, G. Stange, J. Kleffmann, Y.

Elshorbany, and U. Schurath (2012), Comparisons of observed and modeled OH and HO_2 concentrations during the ambient measurement period of the HO_xComp field campaign, *Atmos. Chem. Phys.*, *12*, 2567–2585, doi:10.5194/acp-12-2567-2012.

Kazantseva, N. N., A. Ernepesova, A. Khodjamamedov, O. A. Geldyev, and B. S. Krumgalz (2002), Spectrophotometric analysis of iodide oxidation by chlorine in highly mineralized solutions, *Analytica Chimica Acta*, *456*, 105-119.

Kebabian, P. L., E. C. Wood, S. C. Herndon, and A. Freedman (2008), A practical alternative to chemiluminescence-based detection of nitrogen dioxide: cavity attenuated phase shift spectroscopy, *Environ. Sci. Technol.* 42, 6040–6045.

Kercher, J. P., T. P. Riedel, and J. A. Thornton (2009), Chlorine activation by N_2O_5: simulation, *in situ* detection of $ClNO_2$ and N_2O_5 by chemical ionization mass spectrometry, *Atmos. Meas. Tech.*, *2*, 193-204.

Kim, S., L. G. Huey, R. E. Stickel, D. J. Tanner, J. H. Crawford, J. R. Olson, G. Chen, W. H. Brune, X. Ren, R. Lesher, P. J. Wooldridge, T. H. Bertram, A. Perring, R. C. Cohen, B. L. Lefer, R. E. Shetter, M. Avery, G. Diskin, and I. Sokolik (2007), Measurement of HO_2NO_2 in the free troposphere during the Intercontinental Chemical Transport Experiment–North America 2004, *J. Geophys. Res. Atmos.*, *112*, D12S01.

Ko, M. K. W., N.-D. Sze, C. J. Scott, and D. K. Wisenstein (1997), On the relation between stratospheric chlorine/bromine loading and short-lived tropospheric source gases, *J. Geophys. Res. Atmos.*, *102*(D21), 25507-25517.

Kunz, A., P. Konopka, R. Müller, and L. L. Pan (2011), Dynamical tropopause based on isentropic potential vorticity gradients, *J. Geophys. Res. Atmos.*, *116*, D01110, doi:10.1029/2010JD014343.

Le Breton, M., M. R. McGillen, J. B. A, Muller, A. Bacak, D. E. Shallcross, P. Xiao, L. G. Huey, D. Tanner, H. Coe, and C. J. Percival (2012), Airborne observations of formic acid using a chemical ionization mass spectrometer, *Atmos. Meas. Tech.*, *5*, 3029–3039, doi:10.5194/amt-5-3029-2012.

Le Breton, M., A. Bacak, J. B. A. Muller, P. Xiao, B. M. A. Shallcross, R. Batt, M. C. Cooke, D. E. Shallcross, S. J.-B. Bauguitte, and C. J. Percival (2014), Simultaneous airborne nitric acid and formic acid measurements using a chemical

ionization mass spectrometer around the UK: analysis of primary and secondary production pathways, *Atmos. Environ.*, *83*, 166-175.

Lee, A. M., R. L. Jones, I. Kilbane-Dawe, and J. A. Pyle (2002), Diagnosing ozone loss in the extratropical lower stratosphere, *J. Geophys. Res. Atmos.*, *107*(D11), 4110.

Levine, J. G., P. Braesicke, N. R. P. Harris, N. H. Savage, and J. A. Pyle (2007), Pathways and timescales for troposphere-to-stratosphere transport via the tropical tropopause layer and their relevance for very short lived substances, *J. Geophys. Res. Atmos.*, *112*, D04308, doi: 10.1029/2005JD006940.

Levine, S. Z., W. M. Uselman, W. H. Chan, J. G. Calvert, and J. H. Shaw (1977), The kinetics and mechanism of the HO_2-NO_2 reactions, the significance of peroxynitric acid formation in photochemical smog, *Chem. Phys. Lett.*, *48*, 528-535.

Levy, H., II (1973), Photochemistry of minor constituents in the troposphere, *Planet. Space Sci.*, 21, 575-591.

Liang, Q., E. Atlas, D. Blake, M. Dorf, K. Pfeilsticker, and S. Schauffler (2014), Convective transport of very short lived bromocarbons to the stratosphere, *Atmos. Chem. Phys.*, *14*, 5781–5792, doi:10.5194/acp-14-5781-2014.

Liao, J., H. Sihler, L. G. Huey, J. A. Neuman, D. J. Tanner, U. Friess, U. Platt, F. M. Flocke, J. J. Orlando, P. B. Shepson, H. J. Beine, A. J. Weinheimer, S. J. Sjostedt, J. B. Nowak, D. J. Knapp, R. M. Staebler, W. Zheng, R. Sander, S. R. Hall, and K. Ullmann (2011a), A comparison of Arctic BrO measurements by chemical ionization mass spectrometry and long path ‐ differential optical absorption spectroscopy, *J. Geophys. Res. Atmos.*, *116*, D00R02, doi: 10.1029/2010JD014788.

Liao, J., L. G. Huey, D. J. Tanner, F. M. Flocke, J. J. Orlando, J. A. Neuman, J. B. Nowak, A. J. Weinheimer, S. R. Hall, J. N. Smith, A. Fried, R. M. Staebler, Y. Wang, J.-H. Koo, C. A. Cantrell, P. Weibring, J. Walega, D. J. Knapp, P. B. Shepson, and C. R. Stephens (2011b), Observations of inorganic bromine (HOBr, BrO, and Br_2) speciation at Barrow, Alaska, in spring 2009, *J. Geophys. Res. Atmos.*, *116*, D00R02.

Liao, J., L. G. Huey, E. Scheuer, J. E. Dibb, R. E. Stickel, D. J. Tanner, J. A. Neuman, J. B. Nowak, S. Choi, Y. Wang, R. J. Salawitch, T. Canty, K. Chance, T. Kurosu, R.

Suleiman, A. J. Weinheimer, R. E. Shetter, A. Fried, W. Brune, B.Anderson, X. Zhang, G. Chen, J. Crawford, A. Hecobian, and E. D. Ingall (2012), Characterization of soluble bromide measurements and a case study of BrO observations during ARCTAS, *Atmos. Chem. Phys.*, *12*, 1327-1338, doi:10.5194/acp-12-1327-2012.

Liao, J., L. G. Huey, Z. Liu, D. J. Tanner, C. A. Cantrell, J. J. Orlando, F. M. Flocke, P. B. Shepson, A. J. Weinheimer, S. R. Hall, K. Ullmann, H. J. Beine, Y. Wang, E. D. Ingall, C. R. Stephens, R. S. Hornbrook, E. C. Apel, D. Riemer, A. Fried, R. L. Mauldin III, J. N. Smith, R. M. Staebler, J. A. Neuman, and J. B. Nowak (2014), High levels of molecular chlorine in the Arctic atmosphere, *Nature Geoscience*, *7*, 91-94, doi:10.1038/NGEO2046.

Liu, Z., Y. H. Wang, F. Costabile, A. Amoroso, C. Zhao, L. G. Huey, R. Stickel, J. Liao, and T. Zhu (2010), Evidence of reactive aromatics as a major source of peroxy acetyl nitrate over China, *Environ. Sci. Technol.*, *44*(18), 7017–7022.

Marcy, T. P, R. S. Gao, M. J. Northway, P. J. Popp, H. Stark, D. W. Fahey (2005), Using chemical ionization mass spectrometry for detection of HNO_3, HOCl, and $ClONO_2$ in the atmosphere. *Int. J. Mass Spectrom.*, *243*, 63–70.

Martinez, M., H. Harder, T. A. Kovacs, J. B. Simpas, J. Bassis, R. Lesher, W. Brune, G. J. Frost, E. J. Williams, C. A. Stroud, B. T. Jobson, J. M. Roberts, S. R. Hall, R. E. Shetter, B. Wert, A. Fried, B. Alicke, J. Stutz, V. L. Young, A. B. White, and R. J. Zamora (2003), OH and HO_2 concentrations, sources, and loss rates during the Southern Oxidants Study in Nashville, Tennessee, summer 1999, *J. Geophys. Res. Atmos.*, *108*(D19). doi:10.1029/2003jd003551

McNeill, V. F., J. Patterson, G. M. Wolfe, and J. A. Thornton (2006), The effect of varying levels of surfactant on the reactive uptake of N_2O_5 to aqueous aerosol, *Atmos. Chem. Phys.*, *6*, 1635–1644, http:// www.atmos-chem-phys.net/6/1635/2006/.

Montzka S. A., and S. Reimann (Coordinating lead authors), A. Engel, K. Krüger, S. O'Doherty, W. T. Sturges, D. Blake, M. Dorf, P. Fraser, L. Froidevaux, K. Jucks, K. Kreher, M.J. Kurylo, A. Mellouki, J. Miller, O.-J. Nielsen, V. L. Orkin, R. G. Prinn, R. Rhew, M. L. Santee, A. Stohl, and D. Verdonik (2011), Ozone-Depleting Substances (ODSs) and related chemicals, Chapter 1 in *Scientific Assessment of Ozone Depletion: 2010,* Global Ozone Research and Monitoring Project–Report No. 52, 516 pp., World Meteorological Organization, Geneva, Switzerland.

Navarro, M. A., E. Atlas, A. Saiz-Lopez, X. Rodriguez-Lloveras, D, Kinnison, J.-F. Lamarque, S. Tilmes, M. Filus, N. R.P. Harris, E. Menegu, M. J. Ashfold, A. J. Manning, C. A. Cuevas, S. M. Schauffler, and V. Donets (2015), Airborne measurements of organic bromine compounds in the Pacific tropical tropopause layer, *Proc. Natl. Acad. Sci*.,*112*(45), 13789–13793, doi:10.1073/pnas.1511463112.

Neuman, J. A., D. D. Parrish, M. Trainer, T. B. Ryerson, J. S. Holloway, J. B. Nowak, A. Swanson, F. Flocke, J. M. Roberts, S. S. Brown, H. Stark, R. Sommariva, A. Stohl, R. Peltier, R. Weber, A. G. Wollny, D. T. Sueper, G. Hubler, and F. C. Fehsenfeld (2006), Reactive nitrogen transport and photochemistry in urban plumes over the North Atlantic Ocean, *J. Geophys. Res. Atmos.*, *111*, D23S54. doi: 10.1029/2005JD007010.

Neuman, J. A., J. B. Nowak, L. G. Huey, J. B. Burkholder, J. E. Dibb, J. S. Holloway, J. Liao, J. Peischl, J. M. Roberts, T. B. Ryerson, E. Scheuer, H. Stark, R. E. Stickel, D. J. Tanner, and A. Weinheimer (2010), Bromine measurements in ozone depleted air over the Arctic Ocean, *Atmos. Chem. Phys.*, *10*, 6503-6514, doi:10.5194/acp-10-6503-2010.

Niki, H., P. D. Maker, C. M. Savage, and L. P. Breitenbach (1977), Fourier transform IR spectroscopic observation of pernitric acid formed via $HOO+NO_2 \rightarrow HOONO_2$, *Chem. Phys. Lett.*, *45*, 564-566.

Orlando, J. J (2003), Atmospheric Chemistry of Organic Bromine and Iodine Compounds, in *Organic Bromine and Iodine Compounds*, edited by A. H. Nelson, pp. 253-299, *Handbook of Environmental Chemistry: 2003* Vol. 3, Part R, Springer-Verlag, Berlin, Heidelberg, New York.

Pan, L. L., W. J. Randel, B. L. Gary, M. J. Mahoney, and E. J. Hintsa (2004), Definition and sharpness of the extratropical tropopause: A trace gas perspective, *J. Geophys. Res. Atmos.*, *109*, D23103, doi: 10.1029/2004JD004982.

Pan, L. L., K. P. Bowman, M. Shapiro, W. J, Randel, R-S. Gao, T. Campos, C. Davis, S. Schauffler, B. A. Ridley, J. C. Wei, and C. Barnet (2007), Chemical behavior of the tropopause observed during the Stratosphere-Troposphere Analyses of Regional Transport (START) experiment, *J. Geophys. Res. Atmos.*, *112*, D18110, doi:10.1029/2007JD008645.

Pan, L. L. *et al.* (2016), The Convective Transport of Active Species in the Tropics (CONTRAST) Experiment, *Bull. Amer. Meteor. Soc*. doi:10.1175/BAMS-D-14-00272.1, in press.

Parrella, J. P., D. J. Jacob, Q. Liang, Y. Zhang, L. J. Mickley, B. Miller, M. J. Evans, X. Yang, J. A. Pyle, N. Theys, and M. van Roozendael (2012), Tropospheric bromine chemistry: implications for present and pre-industrial ozone and mercury, *Atmos. Chem. Phys.*, *12*, 6723-6740.

Paulson, S. E., and J. J. Orlando (1996), The reactions of ozone with alkenes: An important source of HO_x in the boundary layer, *Geophys. Res. Lett.*, *23*, 25, 3727-3730

Phillips, G. J., N. Pouvesle, J. Thieser, G. Schuster, R. Axinte, H. Fischer, J. Williams, J. Lelieveld, and J. N. Crowley (2013), Peroxyacetyl nitrate (PAN) and peroxyacetic acid (PAA) measurements by iodide chemical ionisation mass spectrometry: first analysis of results in the boreal forest and implications for the measurement of PAN fluxes, *Atmos. Chem. Phys.*, *13*, 1129–1139, doi:10.5194/acp-13-1129-2013.

Pommier, M., C. A. McLinden, J. A. Neuman, and J. B. Nowak (2012), Biomass burning in Siberia as a source of BrO to the Arctic free troposphere, *Atmos. Environ.*, *62*, 416-423.

Pratt, K. A., K. D. Custard, P. B. Shepson, T. A. Douglas, D. Pöhler, S. General, J. Zielcke, W. R. Simpson, U. Platt, D. J. Tanner, L. G. Huey, M. Carlsen and B. H. Stirm (2013), Photochemical production of molecular bromine in Arctic surface snowpacks, *Nature Geoscience*, *6*, 351–356 doi:10.1038/ngeo1779.

Ren, X., W. H. Brune, J. Mao, M. J. Mitchell, R. L. Lesher, J. B. Simpas, A. R. Metcalf, J. J. Schwab, C. Cai, Y. Li, K. L. Demerjian, H. D. Felton, G. Boynton, A. Adams, J. Perry, Y. He, X. Zhou, and J. Hou (2006), Behavior of OH and HO_2 in the winter atmosphere in New York City, *Atmos. Environ.*, *40*, S252- S263. doi:10.1016/j.atmosenv.2005.11.073.

van Roozendael, M., *et al.* (2002), Intercomparison of BrO measurements from ERS-2 GOME, Ground-based and Balloon Platforms, *Adv. Space Res.*, *29*, 1661-1666.

Ryerson, T. B., E. J. Williams, and F. C. Fehsenfeld (2000), An efficient photolysis system for fast-response NO_2 measurements, *J. Geophys. Res. Atmos.*, *105*(D21), 26447-26461, doi:10.1029/2000jd900389.

Salawitch, R. J., S. C. Wolfsy, E. W. Gottlieb, L. R. Lait, P. A. Newman, M. R. Schoeberl, M. Loewenstein, J. R. Podolske, S. E. Strahan, M. H. Proffitt, C. R. Webster, R. D. May, D. W. Fahey, D. Baumgardner, J. E. Dye, J. C. Wilson, K. K. Kelly, J. W. Elkins, K. R. Chan, and J. G. Anderson (1993), Chemical Loss of Ozone in the Arctic Polar Vortex in the Winter of 1991-1992, *Science*, *261*, 1146-1149.

Salawitch, R. J., D. K. Weisenstein, L. J. Kovalenko, C. E. Sioris, P. O. Wennberg, K. Chance, M. K. W. Ko, and C. A. McLinden (2005), Sensitivity of ozone to bromine in the lower stratosphere, *Geophys. Res. Lett*., 32, L05811, doi: 10.1029/2004GL021504.

Salawitch, R. J. (2006), Biogenic bromine, *Nature*, *439*(19), 275-276.

Salawitch, R. J., T. Canty, T. Kurosu, K. Chance, Q. Liang, A. da Silva, S. Pawson, J. E. Nielsen, J. M. Rodríguez, P. K. Bhartia, X. Liu, L. G. Huey, J. Liao, R. E. Stickel, D. J. Tanner, J. E. Dibb, W. R. Simpson, D. Donohoue, A. Weinheimer, F. Flocke, D. Knapp, D. Montzka, J. A. Neuman, J. B. Nowak, T. B. Ryerson, S. Oltmans, D. R. Blake, E. L. Atlas, D. E. Kinnison, S. Tilmes, L. L. Pan, F. Hendrick, M. van Roozendael, K. Kreher, P. V. Johnston, R. S. Gao, B. Johnson, T. P. Bui, G. Chen, R. B. Pierce, J. H. Crawford, and D. J. Jacob (2010), A new interpretation of total column BrO during Arctic spring, *Geophys. Res. Lett.*, *37*, L21805.

Seinfeld, J. H., and S. N. Pandis (2016), Atmospheric chemistry and physics: from air pollution to climate change, 3rd Edition, John Wiley & Sons, Hoboken, USA

Schofield, R., K. Kreher, B. J. Connor, P. V. Johnston, A. Thomas, D. Shooter, M. P. Chipperfield, C. D. Rodgers, and G. H. Mount (2004), Retrieved tropospheric and stratospheric BrO columns over Lauder, New Zealand, *J. Geophys. Res. Atmos.*, *109*, D14304.

Schwartz, S. E. (1986), Mass-transport considerations pertinent to aqueous-phase reactions of gases in liquid-water clouds, in: *Chemistry of Multiphase Atmospheric Systems*, edited by: Jaechske, W., Springer, Heidelberg, 415–471.

Shirley, T. R., W. H. Brune, X. Ren, J. Mao, R. Lesher, B. Cardenas, R. Volkamer, L. T. Molina, M. J. Molina, B. Lamb, E. Velasco, T. Jobson, and M. Alexander (2006), Atmospheric oxidation in the Mexico City Metropolitan Area (MCMA) during April 2003, *Atmos. Chem. Phys.*, *6*, 2753–2765.

Simpson, I. J., S. K. Akagi, B. Barletta, N. J. Blake, Y. Choi, G. S. Diskin, A. Fried, H. E. Fuelberg, S. Meinardi, F. S. Rowland, S. A. Vay, A. J. Weinheimer, P. O. Wennberg, P. Wiebring, A. Wisthaler, M. Yang, R. J. Yokelson, and D. R. Blake (2011): Boreal forest fire emissions in fresh Canadian smoke plumes: C1-C10 volatile organic compounds (VOCs), CO_2, CO, NO_2, NO, HCN and CH_3CN, *Atmos. Chem. Phys.*, 11, 6445–6463, doi:10.5194/acp-11-6445-2011.

Sioris, C. E., L. J. Kovalenko, C. A. McLinden, R. J. Salawitch, M. van Roozendael, F. Goutail, M. Dorf, K. Pfeilsticker, K. Chance, C. von Savigny, X. Liu, T. P. Kurosu,1 J.-P. Pommereau, H. Bösch, and J. Frerick (2006), Latitudinal and vertical distribution of bromine monoxidein the lower stratosphere from Scanning Imaging Absorption Spectrometer for Atmospheric Chartography limb scattering measurements, *J. Geophys. Res. Atmos.*, *111*, D14301, doi:10.1029/2005JD006479.

Sjostedt, S (2006), Investigation of photochemistry at high lattitudes: comparison of model predictions to measurements of short lived species, PhD thesis, Georgia Institute of Technology, Atlanta, GA, USA.

Sjostedt, S. J., L. G. Huey, D. J. Tanner, J. Peischl, G. Chen, J. E. Dibb, B. Leferd, M. A. Hutterli, A. J. Beyersdorf, N. J. Blake, D. R. Blake, D. Sueper, T. Ryerson, J. Burkhart, and A. Stohl (2007), Observations of hydroxyl and the sum of peroxy radicals at Summit, Greenland during summer 2003, *Atmos. Environ.*, *41*, 5122-5137.

Sinnhuber, B.-M., A. Rozanov, N. Sheode, O. T. Afe, A. Richter, M. Sinnhuber, F. Wittrock, and J. P. Burrows (2005), Global observations of stratospheric bromine monoxide from SCIAMACHY, *Geophys. Res. Lett.*, *32*, L20810, doi: 10.1029/2005GL023839.

Sinnhuber, B.-M., and I. Flokins (2006), Estimating the contribution of bromoform to stratospheric bromine and its relation to dehydration in the tropical tropopause layer, *Atmos. Chem. Phys.*, *6*, 4755–4761.

Slusher, D. L., L. G. Huey, D. J. Tanner, G. Chen, D. D. Davis, M. Buhr, J. B. Nowak, F. L. Eisele, E. Kosciuch, R. L. Mauldin, B. L. Lefer, R. E. Shetter, and J. E. Dibb (2002), Measurements of pernitric acid at the South Pole during ISCAT 2000, *Geophys. Res. Lett.*, 29, doi:10.1029/2002GL015703.

Slusher, D. L., L. G. Huey, D. J. Tanner, F. M. Flocke, and J. M. Roberts (2004), A thermal dissociation-chemical ionization mass spectrometry (TD-CIMS)

technique for the simultaneous measurement of peroxyacyl nitrates and dinitrogen pentoxide, *J. Geophys. Res. Atmos.*, *109*, D19315, doi:10.1029/2004JD004670.

Solomon, S. (1999), Stratospheric ozone depletion, a review of concepts and history, *Rev. Geophysics*, *37*, 3, 275-316.

Sommariva, R., H. D. Osthoff, S. S. Brown, T. S. Bates, T. Baynard, D. Coffman, J. A. de Gouw, P. D. Goldan, W. C. Kuster, B. M. Lerner, H. Stark, C. Warneke, E. J. Williams, F. C. Fehsenfeld, A. R. Ravishankara, and M. Trainer (2009), Radicals in the marine boundary layer during NEAQS 2004: a model study of day-time and night-time sources and sinks, *Atmos. Chem. Phys.*, *9*, 3075–3093.

Sommariva, R., S. S. Brown, J. M. Roberts, D. M. Brookes, A. E. Parker, P. S. Monks, T. S. Bates, D. Bon, D., J. A. de Gouw, G. J. Frost, J. B. Gilman, P. D. Goldan, S. C. Herndon, W. C. Kuster, B. M. Lerner, H. D. Osthoff, S. C. Tucker, C. Warneke, E. J. Williams, and M. S. Zahniser (2011), Ozone production in remote oceanic and industrial areas derived from ship based measurements of peroxy radicals during TexAQS 2006, *Atmos. Chem. Phys.*, *11*, 2471–2485, doi:10.5194/acp-11-2471-2011.

Spencer, K. M., D. C. McCabe, J. D. Crounse, J. R. Olson, J. H. Crawford, A. J. Weinheimer, D. J. Knapp, D. D. Montzka, C. A. Cantrell, R. S. Hornbrook, R. L. Mauldin III, and P. O. Wennberg (2009), Inferring ozone production in an urban atmosphere using measurements of peroxynitric acid, *Atmos. Chem. Phys.*, *9*, 3697-3707.

Stiller, G. P., T. von Clarmann, C. Brühl, H. Fischer, B. Funke, N. Glatthor, U. Grabowski, M. Höpfner, P. Jöckel, S. Kellmann, M. Kiefer, A. Linden, M. López-Puertas, G. Mengistu Tsidu, M. Milz, T. Steck, and B. Steil (2007), Global distributions of HO_2NO_2 as observed by the Michelson Interferometer for Passive Atmospheric Sounding (MIPAS), *J. Geophys. Res. Atmos.*, *112*, D09314, doi:10.1029/2006JD007212.

Talbot, R. W., J. E. Dibb, E. M. Scheuer, Y. Kondo, M. Koike, H. B. Singh, L. B. Salas, Y. Fukui, J. O. Ballenthin, R. F. Meads, T. M. Miller, D. E. Hunton, A. A. Viggiano, D. R. Blakes, N. J. Blakes, E. Atlas, F. Flocke, D. J. Jacob, and L. Jaeglé (1999), Reactive nitrogen budget during the NASA SONEX mission, *Geophys. Res. Lett.*, *26*, 20, 3057-3060.

Tanner, D. J., A. Jefferson, and F. L. Eisele (1997), Selected ion chemicalionization mass spectrometric measurement of OH, *J. Geophys. Res. Atmos.*,*102*(D5), 6415–6425.

Tegtmeier, S., K. Krüger, B. Quack, E. L. Atlas, I. Pisso, A. Stohl, and X. Yang (2012), Emission and transport of bromocarbons: from the West Pacific Ocean into the stratosphere, *Atmos. Chem. Phys.*, *12*, 10633-10648.

Theys, N., M. V. Roozendael, F. Hendrick, C. Fayt, C. Hermans, J.-L. Baray, F. Goutail, J.-P. Pommereau, and M. D. Mazière (2007), Retrieval of stratospheric and tropospheric BrO columns from multi-axis DOAS measurements at Réunion Island (21°S, 56°E), *Atmos. Chem. Phys.*, *7*, 4733-4749.

Thornton, J. A., C. F. Braban and J. P. D. Abbatt (2003), N_2O_5 hydrolysis on sub-micron organic aerosols: the effect of relative humidity, particle phase, and particle size, *Phys. Chem. Chem. Phys.*, *5*, 4593–4603, doi: 10.1039/b307498f.

Veres, P. R., J. M. Roberts, R. J. Wild, P. M. Edwards, S. S. Brown, T. S. Bates, P. K. Quinn, J. E. Johnson, R. J. Zamora, and J. de Gouw (2015), Peroxynitric acid (HO_2NO_2) measurements during the UBWOS 2013 and 2014 studies using iodide ion chemical ionization mass spectrometry, *Atmos. Chem. Phys.*, *15*, 8101–8114, doi:10.5194/acp-15-8101-201.

Wales, P. A., R. J. Salawitch et al., Stratospheric inorganic bromine loading inferred from CONTRAST and ATTREX observations, *in preparation*.

Wang, S., J. A. Schmidt, S. Baidar, S. Coburn, B. Dix, T. K. Koenig, E. Apel, D. Bowdalo, T. L. Campos, E. Eloranta, M. J. Evans, J. P. DiGangi, M. A. Zondlo, R.-S. Gao, J. A. Haggerty, S. R. Hall, R. S. Hornbrook, D. Jacob, B. Morley, B. Pierce, M. Reeves, P. Romashkin, A. ter Schure, and R. Volkamer (2015), Active and widespread halogen chemistry in the tropical and subtropical free troposphere, *Proc. Natl. Acad. Sci*., *112*(30), 9281–9286, doi: 10.1073/pnas.1505142112.

Wang, Y. H., Y. S. Choi, T. Zeng, B. Ridley, N. Blake, D. Blake, and F. Flocke (2006), Late-spring increase of trans-Pacific pollution transport in the upper troposphere, *Geophys. Res. Lett.*, *33*, L01811, doi:10.1029/2005GL024975.

Warwick, N. J., A. Pyle, G. D. Carver, X. Yang, N. H. Savage, F. M. O'Connor, and R. A. Cox (2006), Global modeling of biogenic bromocarbons, *J. Geophys. Res. Atmos.*, *111*, D24305.

Wayne, R. P., I. Barnes, P. Biggs, J. P. Burrows, C. E. Canosa-Mas, J. Hjorth, G. Le Bras, G. K. Moortgat, D. Perner, G. Poulet, G. Restelli, and H. Sidebottom (1991), The nitrate radical: physics, chemistry and the atmosphere, *Atmos. Environ*, *25A*, 1, 1-203.

Wennberg, P. O., *et al.* (1994), Removal of stratospheric O_3 by radicals: *in situ* measurements of OH, HO_2, NO, NO_2, ClO and BrO, *Science*, 266, 398-404.

Woodward-Massey, R., Y. M. Taha, S. G. Moussa, and H. D. Osthoff (2014), Comparison of negative-ion proton-transfer with iodide ion chemical ionization mass spectrometry for quantification of isocyanic acid in ambient air, *Atmos. Environ. 98*, 693-703.

World Meteorological Organization (WMO) (2011), Scientific Assessment of Ozone Depletion: 2010, Global Ozone Research and Monitoring Project – Report No. 52, 516 pp, Geneva, Switzerland.

World Meteorological Organization (WMO) (2014), Scientific Assessment of Ozone Depletion: 2014, World Meteorological Organization, Global Ozone Research and Monitoring Project– Report No. 55, 416 pp., Geneva, Switzerland.

Wu, C.-H., M. M. Birky, and L. G. Hepler (1963), Thermochemistry of some bromine and iodine species in aqueous solution, *J. Am. Chem. Soc*., *67*, 1202-1205.

Yang, X., R. A. Cox, N. J. Warwick, J. A. Pyle, G. D. Carver, F. M. O'Connor, and N. H. Savage (2005), Tropospheric bromine chemistry and its impacts on ozone: A model study, *J. Geophys. Res. Atmos.*, *110*, D23311, doi: 10.1029/2005JD006244.

Zeng, T., Y. H. Wang, K. Chance, E. V. Browell, B. A. Ridley, and E. L. Atlas (2003), Widespread persistent near-surface ozone depletion at northern high latitudes in spring, *Geophys. Res. Lett.*, *30*(24), 2298, doi: 10.1029/2003GL018587.

Zhang, Y. M.-T. Leu, and L. F. Keyser (1997), Heterogeneous chemistry of HO_2NO_2 in liquid sulfuric acid, *J. Phys. Chem. A, 101*, 3324-3330.

Zheng, W., F. M. Flocke, G. S. Tyndall, A. Swanson, J. J. Orlando, J. M. Roberts, L. G. Huey, and D. J. Tanner (2011), Characterization of a thermal decomposition chemical ionization mass spectrometer for the measurement of peroxy acyl nitrates (PANs) in the atmosphere, *Atmos. Chem. Phys.*, *11*, 6529-6547, doi: 10.5194/acp-11-6529-2011.

Zhao, C., Y. Wang, Q. Yang, R. Fu, D. Cunnold, and Y. Choi (2010), Impact of East Asian summer monsoon on the air quality over China: View from space, *J. Geophys. Res. Atmos., 115*, D09301, doi:10.1029/2009JD012745.